Department of Aerospace Engineering
University of Maryland
College Park, Maryland 20742

AERODYNAMIC CHARACTERISTICS OF ROTOR AIRFOILS AS AFFECTED BY SIMULATED BALLISTIC DAMAGE

by

Keith Wayne Robinson

Thesis submitted to the Faculty of the Graduate School
of The University of Maryland in partial fulfillment
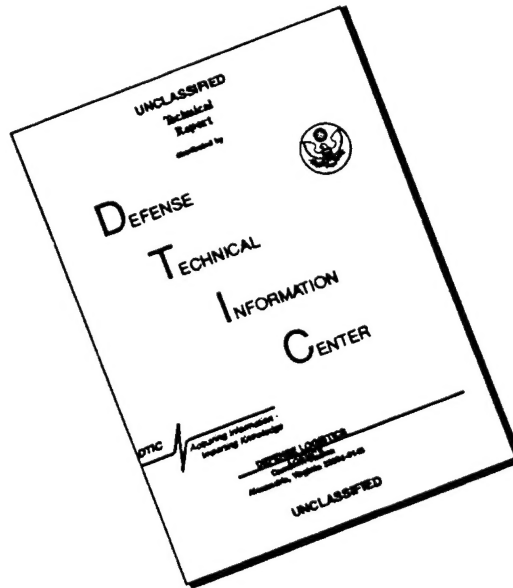of the requirements for the degree of
Master of Science
1995

19960606 092

DISCLAIMER NOTICE

THIS DOCUMENT IS BEST QUALITY AVAILABLE. THE COPY FURNISHED TO DTIC CONTAINED A SIGNIFICANT NUMBER OF PAGES WHICH DO NOT REPRODUCE LEGIBLY.

ABSTRACT

Title of Thesis: AERODYNAMIC CHARACTERISTICS OF ROTOR AIRFOILS
AS AFFECTED BY SIMULATED BALLISTIC DAMAGE

Name of degree candidate: Keith Wayne Robinson

Degree and Year: Master of Science, 1995

Thesis directed by: Dr. J. Gordon Leishman, Associate Professor, Department of
Aerospace Engineering

Tests were made using a 2-D insert in a subsonic wind tunnel to examine the effects of simulated ballistic damage on the aerodynamic characteristics of ten helicopter rotor blade sections. Two undamaged baseline blade sections, comprised of SC1095 and SC1095R8 airfoils, were tested and then modified with different simulated ballistic damage configurations. These comprised of a circular hole with the surrounding skin removed, fore and aft circular holes, and an aft wedge-shaped hole. One blade section was subjected to actual ballistic damage near the trailing edge. The sectional lift, drag and pitching moment were measured at positive and negative angles of attack at Reynolds numbers of one, two, and three million. Pressure measurements were also made for two configurations fitted with pressure taps. Additional tests were conducted over a full 360 degree range in angle of attack for a Reynolds number of one million. The measurements were complemented by oil flow visualization on the blade sections.

The simulated damage caused large disturbances in the flowfield near and downwind of the damaged regions. Generally, flow separation was initiated at the upstream leading edge of the damage, followed by a growth in separation, both in span and intensity, with increasing angle of attack. The aerodynamic characteristics were significantly degraded, with up to a 60 percent reduction in lift-curve-slope, a loss of maximum lift capability of nearly 30 percent, and a significant decrease in the lift-to-drag ratio due to drag increases of up to nearly 340 percent at low angles of attack.

AERODYNAMIC CHARACTERISTICS OF

ROTOR AIRFOILS AS AFFECTED BY

SIMULATED BALLISTIC DAMAGE

by

Keith Wayne Robinson

Thesis submitted to the Faculty of the Graduate School
of The University of Maryland in partial fulfillment
of the requirements for the degree of
Master of Science
1995

Advisory Committee:

Dr. J. Gordon Leishman, Associate Professor and Thesis Advisor
Dr. Inderjit Chopra, Professor
Dr. James Baeder, Assistant Professor
Dr. Jewel Barlow, Associate Professor

DEDICATION

To my wife, Mary Ann, whose support could not have been greater

ACKNOWLEDGMENTS

TABLE OF CONTENTS

LIST OF TABLES

LIST OF FIGURES

NOMENCLATURE

A	Blade section area, ft^2
c	Airfoil chord, ft
C_D	Drag coefficient
C_{D_o}	Zero-lift drag coefficient
C_L	Lift coefficient
C_{Lmax}	Maximum lift coefficient
C_M	Pitching moment coefficient about the 1/4-chord
$dC_L / d\alpha$	Lift-curve-slope, /deg
f	Effective nondimensional location of separation point
M	Mach number
q_∞	Free-stream dynamic pressure, lb / ft
Re	Reynolds number based on airfoil chord, $\rho V_\infty c / \mu_\infty$
V_∞	Free-stream velocity, ft / s
W	Uncertainty in measurement quantity
x_{ac}	Nondimensional aerodynamic center location
x_{cp}	Nondimensional center of pressure location
α	Angle of attack, deg
α_0	Zero-lift angle of attack, deg
ρ_∞	Free-stream density, $slugs / ft^3$

μ_∞ Free-stream viscosity, $slugs\,/\,ft\,/\,s$

Abbreviations

CFD	Computational Fluid Dynamics
DACU	Data Acquisition and Control Unit
GLMWT	Glenn L. Martin Wind Tunnel
HEI	High Explosive Incendiary
IDL	Interactive Data Language
JLF	Joint Live Fire
JTCG / AS	Joint Technical Coordinating Group on Aircraft Survivability
NACA	National Advisory Council on Aeronautics
NASA	National Aeronautics and Space Administration
PSI	Pressure Systems Incorporated
UMARC	University of Maryland Advanced Rotorcraft Code
2-D	Two-Dimensional
3-D	Three-Dimensional

Chapter 1

Introduction

For military helicopters, the vulnerability of the rotor system in a combat situation is an important consideration. During a typical combat scenario, a helicopter can be exposed to a variety of armor piercing and high explosive incendiary rounds. Because helicopters fly low and slow, they are easily detected and are much more susceptible to damage than most fixed wing aircraft.

Like all other military aircraft, helicopters have stringent design requirements on vulnerability. Much of the credit for the increased emphasis on the survivability of aircraft goes to the Joint Coordinating Group on Aircraft Survivability (JTCG/AS). The JTCG/AS was established in 1971 with the goal to develop survivability as a design discipline (Ref. 1). An outgrowth of this group was the Joint Live Fire (JLF) test program, initiated in the early 1980's. This program has tested numerous military tactical aircraft, to include the UH-60A Blackhawk and AH-64A Apache, in realistic vulnerability tests with fuel, weapons systems, and ammunition on board likely to be used in combat. This helps identify especially vulnerable components and aircraft subsystems early in the development cycle so that potential problems can be rectified without incurring unnecessary weight or long-term cost penalties. The major benefit, however, has been the reduction in vulnerability to currently operational aircraft and those now in development.

As discussed in Ref. 1, the UH-60A was one of the first helicopters to be designed to meet fairly strict vulnerability requirements that included ballistic damage inflicted on various aircraft systems. New design features such as separate mechanical flight controls, Kevlar armor, and ballistically tolerant controls and rotor blades, help to greatly reduce vulnerability. A testament to this new design philosophy is a UH-60A in combat operations in Grenada that sustained 45 small-arms and 23mm HEI round hits that damaged the rotor blades, fuel tanks, and control systems, yet still completed its assigned mission (Ref. 1).

On helicopters, both the main and tail rotors are extremely vulnerable to damage-inducing strikes from small as well as large caliber weapons. In the 1970's, Sikorsky developed the UH-60A main rotor, which was significantly more resistant to this type of damage (Ref. 2). The survivability of the rotor blade itself was enhanced by its integral structural design. The leading-edge and trailing edge pocket contours were formed by a skin consisting of fiberglass, boron, and titanium. Additionally, the skin was continuous spanwise, contributing to the axial and bending stiffness of the blade, an important consideration if the spar was ever subjected to ballistic damage (Ref. 2).

While the application of advanced composite material in the construction of rotor blades and rotor hubs has resulted in high levels of damage tolerance in terms of structural soundness, ballistic damage may still present significant problems with regards to its effects on the aerodynamic performance of the rotor blades. This

performance degradation may seriously limit the ability of the aircraft to complete its assigned mission or even sustain flight.

The effect of blade damage is a function of many parameters, including the extent of spar damage, the extent of damage to the aerodynamic contours of the blade, as well as the location of the damage along the blade span. The effect of airfoil damage at the inboard sections of the blade is less important due to the reduced velocity and lift in this area. It does, however, become much more important closer to the blade tips due to the higher dynamic pressures, increased lift, and pitching moments. At a minimum, a small damaged area on the blade may dramatically increase the sectional drag, resulting in an increase in rotor torque (power) requirement. This may limit payload or performance or both. Additionally, the loss of lift and change in section pitching moment, especially near the tip where the dynamic pressure is high, may present flight envelope restrictions such as reduced forward flight capability due to premature blade stall or high control forces. Other potential problems include the emergence of high structural vibrations that could be generated by the damaged rotor system. All of these potential problems will affect the ability of the crew to complete a mission.

It stands to reason that ballistic damage would most likely be realized in a combat situation where the full combat capability of available helicopter forces would be needed. Therefore, the unexpected attrition of helicopter forces due to unforeseen or unanticipated performance degradation must be avoided and, if possible, prevented to ensure continued success on the battlefield. A quantitative understanding of the

3

aerodynamic effects of ballistic damage on the rotor system is essential in order to accurately assess these risks.

1.1 Previous Work

There have been only limited attempts to quantify the effects of ballistic damage on the aerodynamic characteristics of airfoils, and specifically those airfoils used for helicopter rotor blades. Initial interest in ballistic damage focused primarily on fixed wing aircraft, specifically as to how it affected the aeroelastic characteristics of lifting surfaces (Ref. 3). Other investigations have stemmed from the need to determine changes in the aerodynamic forces caused by ballistic damage to accurately predict post-damage aeroelastic behavior (Refs. 3 and 4).

Aside from limited investigations into rotor blade ballistic damage vulnerability made by helicopter manufacturers (Ref. 5), almost no data are available to quantify the effects of ballistic damage on the aerodynamic characteristics of a helicopter rotor blade. Of interest in the present work are those investigations that have examined the effect of ballistic damage on the basic aerodynamic characteristics of wings or airfoil sections, to include changes in the lift, drag, pitching moment and other aerodynamically significant quantities that may affect the performance of the aircraft.

One of the earliest systematic experimental investigations into the aerodynamic characteristics of damaged wings was at the Cornell Aeronautical Laboratory in 1952 (Ref. 6). The test model was a 24 inch chord wing comprised of a NACA 65_1012 airfoil that spanned the 102 inch height of the test section. The wing was tested at

4

Mach numbers of 0.3, 0.7, and 0.85 with various simulated damage configurations, as shown in Appendix A. The data gathered in this investigation were interpreted in a later report by the same laboratory (Ref. 7). The results of the study, which measured the drag increase incurred by each of the different configurations normalized to the area of the hole, became the basis for later studies into the aeroelastic behavior of the wings.

In 1980, Chang (Ref. 3) conducted an investigation into the effects of ballistic damage on the aeroelastic integrity of an effected lifting surface of a fixed-wing aircraft. This work, conducted at the University of Texas in Austin, focused on two fixed-wing models, one representing a basic rectangular planform modeled after the US. Air Force A-10, and the other a swept leading edge configuration referred to as the statistical fighter wing. Citing a theoretical study (Ref. 8) that indicated chordwise and spanwise pressure disturbances would die out within a characteristic distance from a hole, Chang assumed the damage on his models (rectangular holes through the lifting surface in this case) would introduce only local changes to the aerodynamic lift, drag, and moment distributions. Using the data from the Cornell study (Ref. 7) to estimate the increase in drag due to their hole configuration, Chang found that the drag increase (in terms of structural instabilities that may excite resonance within the structure) was, in some cases, significant enough to cause structural failure. However, since the validity of the drag induced aeroelastic failure mechanism in the study was found to be strongly dependent on the accuracy of the aerodynamic data available, it was concluded that additional wind tunnel studies were necessary to gather more exact

5

data regarding the effects ballistic damage on the aerodynamic characteristics of more modern airfoils.

In response to Chang's conclusion, a follow-on study was performed by Westkaemper (Ref. 4), also at the same university, to determine the effects of ballistic damage on the aerodynamic characteristics of a T-38 stabilator. This wing was comprised of a symmetric NACA 65A004 airfoil, and was tested in subsonic flow. Six damaged configurations of up to 2 percent of the stabilator area, one circular and the remainder trapezoidal in shape, were located forward of the mid-chord with centers at 43, 60, and 75 percent span. The stabilators (each from the left side of the aircraft looking forward) were attached to the right hand wall of the test section (looking upstream) in the 5 by 7 foot subsonic wind tunnel at University of Texas at Austin, and tested at a Mach number of 0.186. Force data were measured using strain gauges attached to the torque tube support structure, while pressure measurements were made via pressure taps installed on the upper and lower surfaces of the stabilizer. Oil flow visualization was also used to supplement the force and pressure data.

From these tests, Westkaemper found that in absence of flow separation, the effects of the damage tended to be localized on the wing, with little spanwise flow, and that aerodynamic degradation in terms of forces and moments was modest. However, leading edge separation (a characteristic of the NACA 65A004 airfoil due to its fairly sharp leading edge) produced both spanwise and reverse flow, with the strongest influence observed outboard and forward of the hole. Of note here was the apparent 3-D flow effects on the swept-back stabilator planform.

Quantitatively, Westkaemper (Ref. 4) found that the zero-lift drag coefficient increased by as much as 300 percent, but that at more moderate lift coefficients (e.g., higher angles of attack) the drag increase was generally insignificant. Additionally, this author found that the decrease in coefficient of lift was more consistent across various angles of attack, ranging up to 10 percent for the larger damaged configurations. Unfortunately, Westkaemper's findings were based on a particular 3-D wing flow, which precluded a direct comparison to other wings with other planform shapes. However, a comparison of the respective data yielded a general qualitative understanding of the extent to which 3-D flow effects may influence the aerodynamic characteristics.

In 1993, Eastman (Ref. 5) from Sikorsky completed a three year study assessing the survivability of a UH-60 main rotor blade for ballistic damage resulting from 23mm and 30mm high explosive projectiles. The evaluation was primarily limited to effects on the blade strength, fatigue life, downstream effects of fuselage vibrations and the ability of the crew to function in a high-vibratory environment. Only a limited aerodynamic analysis was completed for each damage case.

Overall, a set of eight damage cases were analyzed for the SC1095 airfoil, as shown in Appendix B. Because Eastman believed that calculating aerodynamic loads on a blade section with ballistic damage would be "difficult and very subjective," blade stall and compressibility effects were assumed to be minimal to simplify the analysis. A mean blade angle of attack of 6 degrees and a mean Mach number of 0.40 were selected to quantify the operating environment of a typical blade section.

7

Although actual wind tunnel data for the baseline (undamaged) SC1095 airfoil were used for comparison, the effects of the ballistic damage on the aerodynamic characteristics were estimated based on photographs of the damage, damage maps, and on hypothesized 2-D pressure distribution changes. Based on ballistic damage at varying spanwise locations affecting a chordwise dimension of approximately 4.2 inches (0.2c) by a spanwise dimension of approximately 44 inches (2.1c), Eastman (Ref. 5) estimated a decrease in lift by as much as 72 percent and an increase in drag by as much as 3400 percent from the undamaged case. Of note here, though, is the purely subjective means by which these results were computed. A visual analysis of damage photographs, estimation techniques, and simplifying assumptions yielded data that have subsequently been found from the present study to be unrepresentative. Recognizing the need for accurate data, however, Eastman did recommend that wind tunnel tests with actual damaged blade sections should be performed to determine proper values for use in any future analysis.

The most applicable work to date on how ballistic damage affects the aerodynamic characteristics of a helicopter rotor blade section was recently conducted by Leishman (Ref. 9) at the University of Maryland in 1993. The work of Ref. 9 included experimental measurements of the aerodynamic characteristics of a typical helicopter blade section. A two foot span undamaged blade section of a helicopter airfoil was aerodynamically tested in a 2-D insert within the 8 by 11 foot working section of the University of Maryland's Glenn L. Martin wind tunnel. The blade section was then subjected to prescribed damage in the form of a 5 inch diameter hole,

with the center located at 60 percent chord and at the mid-span of the specimen. This specimen was then re-tested, and the results compared to the baseline (undamaged) case. Force balance data in the form of sectional lift, drag and pitching moment for both cases were measured at small increments in angle of attack up through stall at Reynolds numbers of one and two million.

Because of the unique capability of the test fixture to fully rotate the installed blade section, additional tests reported in Ref. 9 were performed to measure the airfoil characteristics over a full 360 degree range in angle of attack. This test simulated the high angle of attack and reverse flow region found on the retreating blade in forward flight. All of these measurements were complemented by flow visualization using mini-tufts attached to the upper surface of the damaged blade section. Unfortunately, pressure taps were not installed in the blade section precluding a fuller understanding as to how the flow state was influenced by the damage.

Unlike Westkaemper (Ref. 4), the tests conducted by Leishman (Ref. 9) revealed that the ballistic damage significantly degraded the aerodynamic characteristics of the blade section, with a loss in lifting performance of approximately 30 percent over the full angle of attack range and an increase in sectional drag by as much as 300 percent. Flow visualization also showed that for increasing angles of attack, the flow separation produced at the damaged region extended over a progressively larger part of the blade span. These results confirmed that the aerodynamic effects of local ballistic damage were not necessarily confined to regions

9

in the immediate vicinity of the damage. Therefore, a small amount of damage on a rotor may have quite significant effects on rotor loads and performance.

Considering the focus and timeliness of these findings, the study by Leishman enabled a much better quantitative understanding of the significance of ballistic damage on the aerodynamic characteristics of a typical rotor blade section. The work also provided a solid foundation for further research on the problem. However, it was clear that a systematic study into the effects of damage size, chordwise location, and nature of damage, was still required. This, however, is a formidable undertaking and a more select study must be performed. To this end, the present work is an extension of the work of Leishman and considers some of the aerodynamic issues associated with rotor blade vulnerability in a more systematic and quantifiable manner.

1.2 Problem Statement

In view of the somewhat limited reported studies on the subject of ballistic damage on airfoil performance, there is currently only a limited understanding on how this damage may compromise helicopter performance, vibratory loads or the aeroelastic stability of the rotor system. Previous work (Ref. 9) has concluded that drag can be expected to rise by as much as 300 percent on the damaged blade section, while the lift for a given angle of attack may decrease by up to 30 percent. Although extrapolating the global effects of a damaged blade section across the rotor disk is not in the scope of the current work, it is clear that a small area of damage may be severe

enough to influence the rotor performance and loads that limit the completion of a given mission.

The study of how ballistic damage affects the aerodynamic characteristics of helicopter rotor blades can be very complex, especially if considering the three-dimensionality of the resulting flow over the entire rotor disk. The fact that a helicopter rotor blade operates in an environment that is very dynamic and time-varying makes it difficult to precisely quantify these effects. Therefore, it is necessary to study these effects in a much more idealized manner. Through the use of 2-D measurements, it is possible to study the aerodynamic effects of ballistic damage on a typical blade section, and ultimately to use this information in a more comprehensive three-dimensional analysis to assess various interrelated effects on rotor loads, performance and aeroelasticity. This will ultimately cumulate in a much more rigorous ballistic damage model than is currently available to help predict overall helicopter performance under damaged conditions.

1.3 Present Work

This thesis describes an extension of the work of Leishman (Ref. 9), to more types of simulated damage. The overall objective in the present work was to more precisely quantify the effects of various configurations of simulated, as well as actual, ballistic damage on the aerodynamic characteristics of representative helicopter blade sections. Also, a common problem found in past experiments on the aerodynamics of ballistic damage has been the overall lack of focus on helicopter rotor blades.

Helicopter blade sections are often quite different to those used on fixed-wing aircraft, and it is difficult to extrapolate effects found on fixed-wing aircraft to those of helicopters. The amount of previous research done in this regard has been very narrow in scope. Therefore, the primary objective of the present work was to broaden the scope of Ref. 9, and direct toward gaining a better understanding on how the size, shape, and location of ballistic damage affects the aerodynamic characteristics of a typical helicopter rotor blade section.

This objective was met by testing two undamaged helicopter main rotor blade sections with different airfoil profile shapes (one fitted with pressure taps), numerous prescribed damage configurations, as well as an actual ballistic damage case. The specimens were tested through various angles of attack and Reynolds numbers. Force balance and pressure data were obtained to quantify the effect of ballistic damage on basic characteristics of the airfoil, including changes in C_L, C_D, C_M, lift-curve-slope, and chordwise pressure distributions at three different spanwise locations. Extensive oil flow visualization tests were made for each configuration to enhance the qualitative understanding of the effects of the damage on the flow environment across the blade section.

Finally, in a very general approach, some ideas are proposed that could be used to predict the degradation in airfoil performance as a function of the chordwise location of the ballistic damage. The results were then compared to the actual test results in an attempt to determine if a simplified aerodynamic model of the ballistic damage problem was valid and deserving of further research.

Chapter 2

Description of the Experiment

2.1 Test Facility

The tests were conducted in the Glenn L. Martin wind tunnel at the University of Maryland. This is a closed return tunnel with an 8 by 11 foot working section. Although Reynolds numbers of up to approximately 3.5×10^6 based on airfoil chord can be achieved in this tunnel, the present tests were conducted at the following Reynolds numbers and corresponding wind speeds based a mean tunnel operating temperature of 85°F

Re #	V_∞ (ft/sec)	V_∞ (mph)	q_∞ (lb/ft^2)	Mach #
1×10^6	91	62	9.82	0.08
2×10^6	182	124	39.28	0.16
3×10^6	273	186	88.38	0.24
3.5×10^6	318	217	120.29	0.28

Table 1: Summary of Test Reynolds Number Data

These conditions are representative of the retreating blade of a helicopter in forward flight. The wind speed was limited to a Reynolds number of 3×10^6 in order to prevent high aerodynamic loads on the test blade sections beyond the capabilities of the 2-D insert and force balance measurement system.

The tests on the blade sections were made possible using a special 2-D insert placed inside the working section of the wind-tunnel. This insert was designed and

built for the tests conducted in Ref. 9. The insert consisted of floor to ceiling false walls, with the test blade section spanning these two walls. A photograph of the insert is shown in Fig. 1. The 2-D insert essentially reduces the 3-D effects on the test blade section by making the wing appear to be of high aspect ratio and, therefore, nominally two-dimensional. Even with the insert, however, true 2-D flow is impossible to achieve. This issue will be discussed again later.

As detailed in Fig. 2, the insert walls comprised a NACA 0015 nose and trailing-edge section, with a flat center section. The center panels were manufactured from aluminum, and the leading and trailing edges from a foam core with a glass fiber skin. These leading edge and trailing edge panels were mounted to the main support by structural fasteners. The 2-D insert was designed to accommodate test sections of up to approximately 30 inches in chord. For the present tests, the gap between both insert walls was set to 2 feet. However, provisions have been made in the design to allow tests on wings with spans greater or less than 2 feet. The dimensions of the 2-D insert are given in Fig. 3.

The blade sections were mounted between two circular disks that were located flush with the flat center section of the insert. The blade sections were attached to these disks by means of bolts inserted into plugs fitted inside the spar of the blade specimens. The circular disks were rotated by a pitch drive mechanism, which comprised a ring gear driven by a servo motor through a chain transmission. This enabled the test blade sections to be rotated a full 360 degrees. A displacement transducer was used to determine the angular position, and therefore, the geometric

angle of attack of the blade section. The reference angle for all angle of attack measurements was that of the left-most side of the test blade section (looking upstream). This enabled the angle of attack positioning to be as precise as possible.

The entire blade section support structure and pitch change mechanism was mounted to the 6-component yoke balance system of the wind tunnel. All physical connections to the balance system were made inside the insert walls by means of the structure detailed in Fig. 4. This prevented any interference from the insert walls. Using the balance system, measurements could then be made of the total wing lift, pitching moment and drag at any angle of attack between 0 and 360 degrees.

Because of the highly 3-D nature of ballistic damage (usually a hole with a ragged edge on one or both sides of the blade), obtaining the true 2-D aerodynamic properties of any one section of the blade is impractical, if not impossible. Therefore, the measured aerodynamic characteristics represent the effects of ballistic damage on a typical blade element of up to about half of the test span or, in the present tests, one foot. This is also representative of the size of blade element discretization used in modern comprehensive rotor analyses.

2.2 Special Considerations in 2-D Wind Tunnel Testing

Wind tunnel investigations of 2-D wing characteristics constitute an important phase of aerodynamic testing. While most of the current understanding into the behavior of airfoil sections is a result of 2-D wind tunnel testing, some special considerations must be taken into account when interpreting the measurements. These

considerations are especially important when comparing the relative performance of different airfoils.

Usually, in any experiment, the test airfoil is made to fully span either the width or the height of the wind tunnel test section or that of a 2-D insert (as used in the present tests). This increases the effective aspect ratio of the wing or blade section. While the effects of 3-D flow can never be completely eliminated, the wind tunnel or 2-D insert walls essentially act as boundaries preventing spanwise flow, minimizing any "relieving" effects on either end of the wing and, consequently, the effects of 3-D flow. If any pressure measurements are necessary, then they are usually made at or near the mid-span where the 3-D effects and interference due to the wind tunnel or 2-D insert walls are minimized.

Regardless of the wing aspect ratio, flow separation (which tends to be 3-D in nature) will ultimately occur on the wing. If severe enough, this separation will almost certainly affect the airfoil characteristics at the mid-span. Thus, the possibility of 3-D stall developments should be kept in mind when statically testing airfoils at high angles of attack. Some knowledge of the stall development is essential, especially when comparing the aerodynamic behavior of different airfoils or when comparing the relative merits of airfoils tested in different wind tunnel where different flow characteristics may exist.

As noted before, 2-D flow is extremely difficult to attain on any wing configuration with any aspect ratio, especially near maximum lift. Under these conditions, the flow generally separates in a non-linear manner across the span and

forms a series of "stall cells" which, depending on the airfoil, may appear as mushroom shapes spread across the trailing edge (Ref. 16). Flow visualization by means of mini-tufts or oil is an easy and effective way to examine the development of this flow separation over the wing and the its effect on the flow pattern. However, because of the greater flow details revealed with oil flow visualization, this is generally the preferable technique.

In many so-called 2-D tests, flow separation may occur at the wing/wind tunnel wall junction, depending on the wind tunnel used and the thickness of the wall boundary layer. A characteristic "scarf" vortex may form at this junction, trailing back along the chordline of the wing (see Figs. 5 and 6). The presence of this vortex helps keep the flow attached at the outer span regions, sometimes adding to the 3-D nature of the flow at high angles of attack. Therefore, it should be recognized that there is probably no such thing as true 2-D airfoil characteristics since all measurements are contaminated, to some degree, by the effects of spanwise flow and flow separation (Ref. 11). One can only understand the significance of the problem and attempt to minimize its effect on the measured data.

2.3 Rotor Blade Sections

Five blade sections were provided by the U. S. Army Research Laboratory at Aberdeen Proving Ground, Maryland for use in this experiment. These specimens were taken from an actual U. S. Army helicopter rotor blade representative of current fielded systems. Of the five blade sections, three were made up of the SC1095 airfoil

and the remaining two of the SC1095R8 airfoil (see Fig. 7). All were refurbished to an aerodynamically smooth contour and spray painted with a flat black finish. Each of the blade sections had a chord of 1.731 feet and a span of 2.0 feet, resulting in an undamaged reference area of 3.462 ft^2. Note that in this thesis all of the aerodynamic coefficients were normalized to this undamaged reference area. Because the rotor blade had a pre-twist angle of 18 degrees (leading edge down from root to tip), the blade sections exhibited approximately 1.5 degrees of linear twist along their span. This was compensated for by assuming the angle of attack at the mid-chord to be representative for all calculations regarding the aerodynamic characteristics of the blade sections. For example, data taken at a 2-D insert angle of attack 10 degrees were considered to be representative of 9.25 degrees for the blade section.

In an attempt to maximize the number of configurations available for testing, four of the five blade sections provided by the U.S. Army were modified as the experiment progressed. This involved either plugging existing holes, cutting new holes, or, in one case, modifying the lip of a hole to represent the "petalling" that would be present if a projectile passed through the metal spar. Ultimately, ten different airfoil configurations were tested over the course of the experiment (see Table 2 and Fig. 8)

Case	Airfoil	Blade Configuration
Case 1	SC1095	Undamaged
Case 1A	SC1095	Aft circular hole
Case 1B	SC1095	Aft wedge
Case 1C	SC1095	Actual ballistic damage
Case 1D	SC1095	Center circular hole plugged w/ pressure taps
Case 1E	SC1095	Center circular hole w/ pressure taps
Case 2	SC1095-R8	Aft circular hole plugged
Case 2A	SC1095-R8	Forward circular hole
Case 2B	SC1095-R8	Forward circular hole w/ petalling
Case 2C	SC1095-R8	Aft circular hole

Table 2: Summary of Blade Section Configurations

Note from the summary table that the blade sections were combined as cases sharing the same airfoil. Thus, the number in the case designation simply identifies the airfoil type when reviewing the results.

Case 1 (see Fig. 9) was an undamaged blade section that was tested to establish the baseline characteristics of the SC1095 airfoil. After completing the test runs for Case 1, the blade section was modified for testing as Case 1A (see Fig. 10). For Case 1A, ballistic damage was simulated by means of a circular hole 4 inches (0.193 % chord or 0.193c) in diameter. This hole was cut normal to the top surface at the mid-span of the blade section, and was located 13.52 inches (0.651c) downstream of the leading edge. Upon completion of testing for Case 1A, the blade section was again modified for testing as Case 1B (see Fig. 11). To approximate the actual ballistic damage from Case 1C, additional pieces were cut from the blade section to give a wedge-shape with a base of 14 inches (0.674c) and a height of 6.79 inches

(0.327c). The point on top of the wedge was located 12.98 inches (0.625c) downstream of the leading edge with the base located 1 inch upstream from the trailing edge.

Case 1C (see Figs. 12-14) was the only blade section subjected to actual ballistic damage. Prepared by the U. S. Army Research Laboratory at Aberdeen Proving Ground, Maryland, Case 1C was an undamaged blade section through which a representative projectile was fired. The damage inflicted on the blade section was of the same approximate size and location of the simulated (wedge-shaped) ballistic damage used in Case 1B.

Cases 1D and 1E were the same blade section used by Leishman in Ref. 10. For Case 1E (see Figs. 15a and 15b), the ballistic damage was simulated by means of a circular hole 5 inches (0.241c) in diameter. This hole was cut at the mid-span of the wing, and was located 10 inches (0.481c) downstream of the leading edge. Around the periphery of the hole, a one inch ring of the glass-fiber skin was removed to expose the paper honeycomb interior structure of the rotor blade. After testing for Case 1E was completed, the blade section was modified by plugging the hole and replacing the one inch ring of glass-fiber skin for testing as Case 1D (see Figs. 16a and 16b).

Data from both Cases 1D and 1E were used to determine the repeatability of the tests from Ref. 9. Unfortunately, this particular blade section was cut from a transition area on the rotor blade. The right approximately 2.08 inches (9 percent of span) of the blade section exhibited the general shape of the SC1095R8 airfoil. In order to validate the force balance as well as pressure data taken from the this blade

section, it was necessary to compare it against the characteristics of Case 1, the baseline blade section for the SC1095 airfoil. Since the pressure taps were installed on the opposite side of the blade, away from the transition area, and the transition area itself was very small, good general agreement in the force balance data was expected.

To establish the baseline characteristics for the SC1095R8 airfoil, the blade section to be used for Case 2C was modified for testing as Case 2 (see Fig. 17). This modification consisted of plugging the hole near the trailing edge of the blade section. The ballistic damage for Case 2A (see Fig. 18) was simulated by means of a circular hole 4 inches (0.193c) in diameter. This hole was cut normal to the top surface at the mid-span of the blade section, and was located 3.3 inches (0.159c) downstream of the leading edge. Of note is that the hole in Case 2A was cut through the center of the titanium spar running along the span of the blade section. Case 2A was further modified for testing as Case 2B (see Fig. 18). To simulate the "petalling" that takes place when a projectile passes through metal, a metal ring of jagged teeth approximately 0.5 inches (0.024c) high was attached around the circumference of the hole.

Finally, the plug in the blade section used in Case 2 was removed to modify the blade section for testing as Case 2C (see Fig. 19). The ballistic damage for Case 2C was simulated by means of a circular hole 4 inches (0.193c) in diameter. This hole was cut normal to the top surface at the mid-span of the blade section, and was located 13.47 inches (0.649c) downstream of the leading edge.

2.4 Data Acquisition

The entire data acquisition process was controlled by a HP-A900 computer. A custom data acquisition routine was written using Hewlett-Packard's VEE (Virtual Engineering Environment) to control the angle of attack schedule, and acquire measurements of the air loads. The lift, drag and pitching moment were automatically sampled three hundred times at each test condition, except at high angles of attack where, due to the unsteadiness of the flow, only two hundred samples were taken. The final measurements were an average acquired to within a prescribed tolerance and statistical accuracy. The measurements were plotted on a graphics monitor in real-time during the tests using IDL graphics routines.

Deadweight tares were obtained from balance measurements with the wing installed but with the wind off. Tares were obtained over the required range of angles of attack, and curve fitted to obtain the appropriate corrections at intermediate angles of attack. These tares were automatically subtracted from the measurements during the data acquisition process.

To enable static pressure measurements, a total of 58 pressure taps (33 on the upper surface and 25 on the lower surface) were installed in the blade section used for Cases 1D and 1E. Because of the honeycomb construction of the inner blade section, stainless steel pressure sensing tubes were inserted through the center of the blade and, having been bent 90 degrees at the end, were then inserted into the composite skin of the upper and lower surfaces. The tubes protruded out of the side of the blade

section, and were connected by Tygon tubing to a pressure module mounted inside of the left wall (looking upstream) of the 2-D insert.

Two objectives were used in determining the placement of the pressure taps. The first objective was to determine how the damage influenced the pressure profile of the airfoil, which necessitated placing pressure taps along the chord at the same spanwise location as the damage. The second objective was to determine how representative the force balance measurements were of 2-D flow. This necessitated placing pressure taps at different spanwise locations away from the mid-span to identify the extent of the 3-D flow occurring on the blade section.

With the previous objectives in mind, the pressure taps were concentrated on three spanwise stations, mid-span, 5.5 inches (23 percent span) left of mid-span, and 8.5 inches (35.4 percent span) left of mid-span (looking upstream) (see Figs. 15a and 15b). These static pressure measurements allowed for a direct comparison between the aerodynamic characteristics measured directly from force balance system and the aerodynamic characteristics derived through the integration of the pressure data. The spanwise pressure profiles also allowed for an accurate determination of the degree of 2-D flow and its variation across the span.

Using the pressure tap instrumented blade section, time-averaged pressures were measured at 58 locations. The pressure measurements were taken using a Pressure Systems Inc. (PSI) multi-channel Data Acquisition and Control Unit (DACU). The module contained 32 miniature quartz pressure transducers, analog multiplexers, and analog-to-digital converters. A miniature pneumatic valving system

23

in the module permitted rapid on-line calibration of the pressure sensors, which was essential in maintaining measurement accuracy within a 2 percent tolerance over the considerable tunnel run times. Thus, the PSI system enabled very low pressures of less than 0.001 lb/in^2 (7.5 N/m^2) to be measured with good accuracy and high repeatability.

The dynamic pressure in the test section was measured indirectly as a pressure drop between the static pressure in the settling chamber and the average static pressure measured at a ring of orifices at the forward upstream end of the test section. The relationship between the pressure drop and the actual dynamic pressure in the test section was obtained by means of a NASA calibrated pitot static probe located in the test section at the blade section location, but without the blade section installed. The measured dynamic pressure at this position was correlated with the pressure drop between the settling chamber and the pressures measured at the forward end of the tunnel test section.

During the tests, the dynamic pressure was maintained as closely as possible to the required value by careful adjustment of the fan speed. With increasing wing angle of attack, the increased solid and wake blockage produced by the wing required higher fan power and speed to maintain a constant dynamic pressure in the working section. During some tests at high angles of attack, periodic separation, reattachment and vortex shedding made it difficult to maintain a constant dynamic pressure. Under these conditions, measuring the aerodynamic characteristics to a specified precision

was difficult or impossible. The final values, therefore, have a higher overall uncertainty.

2.5 Test Conditions

Experiments on each of the blade specimens were conducted at Reynolds numbers of 1×10^6, 2×10^6, and 3×10^6 (M $\cong$ 0.08, 0.16, and 0.24). Since the airfoils were non-symmetric, it was necessary to examine both the negative and positive angle of attack ranges up through stall. At Reynolds numbers of 1×10^6 and 2×10^6, tests were conducted over angles of attack ranging from -25 degrees to 35 degrees in steps of one degree. At Reynolds numbers of 3×10^6, tests were conducted over angles of attack ranging from -5 degrees to 25 degrees in steps of one degree. Angles of attack at the highest Reynolds number were limited in magnitude in order to prevent high aerodynamic loads on the test blade sections beyond the capabilities of the 2-D insert and force balance measurement system. Overall, these angles of attack provided measurements over the typical working range of a helicopter rotor blade section. Smaller angle of attack increments (as small as one quarter of a degree) were taken near the point of maximum lift to accurately determine the stall mechanism (i.e., abrupt or gradual).

It should be noted here that care must be taken when operating at high Reynolds numbers, as aerodynamic loads increase with the square of the freestream velocity. While the blade sections used in this experiment generated only about 53 pounds of lift at a Reynolds number of one million, the lift being generated increased

to 471 pounds at a Reynolds number of three million, close to the maximum limit of the wind tunnel force balance system.

For Cases 1D and 1E, additional tests were conducted at a Reynolds number of 1×10^6 over an angle of attack range of 360 degrees. To minimize the total time required for the tests, the angle of attack increment for different ranges was varied. From 185 to 160 degrees, 25 to -25 degrees, and -160 to -185 degrees, the angle of attack was changed in steps of one degree. For all other ranges, the angle of attack was changed in steps of three degrees. It was not practical to conduct full 360 degree angle of attack sweeps at the higher Reynolds numbers due to the high loads imposed on the support and balance system.

For the tests described above, note that increasing angle of attack sweeps were made for all cases except for the 360 degree rotations, where decreasing angle of attack sweeps were made. This also helped confirm the existence of any static hysteresis effects in the measurements. Because of the differences in the physical processes of flow separation versus flow reattachment, it is known that under some circumstances different values of the air loads can be obtained depending on the actual test technique. For example, at high angles of attack different results can be obtained depending on whether the angle of attack is continuously increased or decreased over this range. Similarly, different results can be obtained if the angle of attack is set first and the wind speed increased to the required conditions, versus setting the wind speed and then incrementing the angle of attack. This phenomenon is usually referred to as "static hysteresis".

26

A summary of the test table used in the wind tunnel experiments is given in

Table 3.

Run Num	Airfoil	Case	Blade Description	Re Number	AOA Range	AOA Increment
4,5,6	SC1095	Case 1E	center hole w/ taps	1000000	(-25 to +25)	1 deg
7		Case 1E	center hole w/ taps	2000000	(-25 to +25)	1 deg
8		Case 1E	center hole w/ taps	1000000	(+185 to -185)	1 deg ...185/160,25/-25,-160/-185 3 deg elsewhere
9		Case 1E	center hole w/ taps	3000000	(-5 to +25)	1 deg
10	SC1095	Case 1D	plugged hole w/ taps	1000000	(-25 to +25)	1 deg
11		Case 1D	plugged hole w/ taps	2000000	(-25 to +25)	1 deg
12		Case 1D	plugged hole w/ taps	1000000	(+185 to -185)	1 deg ...185/160,25/-25,-160/-185 3 deg elsewhere
13		Case 1D	plugged hole w/ taps	3000000	(-5 to +25)	1 deg
14-21*	SC1095	Case 1D	plugged hole w/ taps	2000000	(-2,0,5,10,12,14,16)	N/A
22-27*		Case 1E	center hole w/ taps	2000000	(-2,0,5,10,12,14,16)	N/A
28**		Case 1E	center hole w/ taps	2000000	(12,14,16)	N/A
29	SC1095-R8	Case 2A	fwd hole	1000000	(-25 to +35)	1 deg
30		Case 2A	fwd hole	2000000	(-25 to +35)	1 deg
31		Case 2A	fwd hole	3000000	(-5 to +30)	1 deg
32-35*		Case 2A	fwd hole	2000000	(5,10,15,20)	N/A
36	SC1095-R8	Case 2	undamaged	1000000	(-25 to +35)	1 deg
37		Case 2	undamaged	2000000	(-25 to +35)	1 deg
38		Case 2	undamaged	3000000	(-5 to +25)	1 deg
39-42*		Case 2	undamaged	2000000	(5,10,15,20)	N/A
47	SC1095-R8	Case 2C	aft hole	1000000	(-25 to +35)	1 deg
48		Case 2C	aft hole	2000000	(-25 to +35)	1 deg
49		Case 2C	aft hole	3000000	(-5 to +25)	1 deg
43-46*		Case 2C	aft hole	2000000	(5,10,15,20)	N/A
50	SC1095	Case 1	undamaged	1000000	(-25 to +35)	1 deg
51		Case 1	undamaged	2000000	(-25 to +35)	1 deg
52		Case 1	undamaged	3000000	(-5 to +25)	1 deg
53-57*		Case 1	undamaged	2000000	(5,10,15,20,14.5)	N/A
58	SC1095	Case 1C	actual ballistic dam.	1000000	(-25 to +35)	1 deg
59-60		Case 1C	actual ballistic dam.	2000000	(-25 to +35)	1 deg
61		Case 1C	actual ballistic dam.	3000000	(-5 to +25)	1 deg
62	SC1095	Case 1A	aft hole	1000000	(-25 to +35)	1 deg
63		Case 1A	aft hole	2000000	(-25 to +35)	1 deg
64		Case 1A	aft hole	3000000	(-5 to +25)	1 deg
65-68*		Case 1A	aft hole	2000000	(5,10,15,20)	N/A
73	SC1095	Case 1B	wedge w/ trailing edge	1000000	(-25 to +35)	1 deg
74		Case 1B	wedge w/ trailing edge	2000000	(-25 to +35)	1 deg
75		Case 1B	wedge w/ trailing edge	3000000	(-5 to +25)	1 deg
76		Case 1B	wedge w/o trailing edge	3000000	(-5 to +25)	1 deg
69-72*		Case 1B	wedge w/ trailing edge	2000000	(5,10,13.25,20)	N/A
77	SC1095-R8	Case 2B	fwd hole w/ petalling	1000000	(-25 to +35)	1 deg
78		Case 2B	fwd hole w/ petalling	2000000	(-25 to +35)	1 deg
83		Case 2B	fwd hole w/ petalling	3000000	(-5 to +25)	1 deg
79-82*		Case 2B	fwd hole w/ petalling	2000000	(5,10,15,20)	N/A
* - Indicates Oil Flow Visualization						
** - Indicates Smoke Flow Visualization						

Table 3: Test Run Summary

2.6 Experimental Accuracy

The VEE test balance data acquisition program required that the desired precision of each force or moment component be specified in dimensional form. In practice, the achievable precision depends entirely on the unsteadiness of the aerodynamic loads. Therefore, because of steady and unsteady flow considerations, the precisions used in this experiment were defined differently for different angle of attack regions, as given in Table 4.

AOA Range (deg)	Lift (lb$_f$)	Drag (lb$_f$)	Moment (ft-lbs)
185 to 175	0.125	0.0125	0.15
174 to 13	0.25	0.025	0.3
12 to -12	0.125	0.0125	0.3
-13 to -174	0.25	0.025	0.3
-175 to -185	0.125	0.0125	0.15

Table 4: Force Balance Precision Settings

In this experiment, the balance loads were obtained to a target precision of the mean based on an equation of the form

$$P = \frac{k\sigma}{\sqrt{n}} \qquad (1)$$

28

where P is the target precision, σ is the standard deviation, n is the number of samples acquired, and k is a factor which is a function of the level of confidence and the number of samples.

The force balance results were converted into sectional or coefficient values by normalizing by dynamic pressure and the reference (undamaged) area of the blade section $(3.462\,ft^2)$. The force coefficients were obtained from

$$C_L = \frac{L}{q_\infty A} \tag{2}$$

$$C_D = \frac{D}{q_\infty A} \tag{3}$$

and the moment coefficient about the ¼-chord from

$$C_M = \frac{M}{q_\infty A c} \tag{4}$$

where c is the blade chord and A is the reference (undamaged) area. The error in the measurement of the aerodynamic coefficients is a function of the uncertainty of the measurements. The uncertainty, W_{C_L}, in the lift coefficient, C_L, is given by

$$W_{C_L} = \left[\left(\frac{\partial C_L}{\partial L} W_L \right)^2 + \left(\frac{\partial C_L}{\partial q_\infty} W_{q_\infty} \right)^2 + \left(\frac{\partial C_L}{\partial A} W_A \right)^2 \right]^{\frac{1}{2}} \tag{5}$$

where W_{C_L}, W_{q_∞}, and W_A are the errors in the measurement of the lift force, the free-stream dynamic pressure, and the wing area, respectively (Ref. 12). These estimated errors are summarized in Table 5.

Parameter	Error
Lift, L	±0.1 lb$_f$
Drag, D	±0.1 lb$_f$
Moment, M	±0.5 ft-lbs
Dynamic Pressure, q_∞	±0.072 lb/ft^2
Blade Section Area, A	0.013 ft^2

Table 5: Summary of Estimated Errors in Measured Quantities

The preceding equation may be simplified to obtain the relative error in C_L, giving

$$\frac{W_{C_L}}{C_L} = \left[\left(\frac{W_L}{L} \right)^2 + \left(\frac{W_{q_\infty}}{q_\infty} \right)^2 + \left(\frac{W_A}{A} \right)^2 \right]^{\frac{1}{2}} \qquad (6)$$

Similar equations can be derived to obtain the error in the measurements of C_M and C_D. In general, the errors in the force and moment coefficient were found to be less than 0.1 percent under all conditions, except when periodic flow separation occurred on the blade section. This situation will be addressed later in Chapter 3 of this thesis.

2.7 Oil Flow Visualization

Oil Flow visualization was used for every configuration, both damaged and undamaged. An oil mixture, consisting of oil mixed with titanium dioxide powder, was applied to the upper and lower surfaces of each blade section and on the adjoining left and right walls of the 2-D insert. This oil mixture gives a white deposit on a black background suitable for high contrast flow visualization.

30

For these tests, the tunnel wind speed was quickly increased to the target wind speed (corresponding to a Reynolds number of 2×10^6) and the flow patterns were allowed to develop for approximately 6 to 10 minutes, depending on the angle of attack. Caution was exercised here to avoid letting the tunnel run for too long. When using oil, flow patterns tend to reach an optimum point, beyond which time the oil is finally blown off the surface. Once the flow pattern had fully developed, the wind tunnel speed was quickly decreased to allow entry into the wind tunnel and photographs to be immediately taken of the blade section.

Because each blade section was finished in flat black paint, the white oil provided superb contrast, enabling even the most minute flow details to be seen quite clearly. Both still photographs and video were used to document the development of flow separation on the blade section for angles of attack up to and beyond stall. The video was particularly useful near stall onset, however, since the flow was often unsteady here due to intermittent flow separation and reattachment. The video camera was mounted outside of the wind tunnel, on top of the test section ceiling, and recorded the development of the flow pattern through a clear Plexiglas ceiling panel. In at least one case, where the difference between the reference angle and the stall angle closed to within less than one-half a degree, a well developed pre-stall flow pattern was obliterated when perturbations in the wind tunnel flow caused the flow over the blade section to separate. Here, the video yielded the necessary picture images of the flow pattern that could not have been easily photographed otherwise.

In the flow visualization results, transition from a laminar to a turbulent boundary layer was easily seen by the presence of a laminar separation bubble near the leading edge of the airfoil. Typically, this bubble became narrower and moved closer to the leading edge with increasing angle of attack (Ref. 13). For the airfoils tested in the current work, the laminar separation bubble remained present throughout the entire range of angles of attack, even beyond the point of stall. Care must be taken, however, when considering the connection between the characteristics of this bubble and the corresponding aerodynamics. For example, the presence of this bubble may sometimes seem irregular because of local accumulations of oil. Occasionally, these accumulations of oil may cause the bubble to burst. Imperfections on the leading edge of the airfoil may also cause the bubble to burst by triggering a transition to a turbulent boundary layer in the flow prior to the bubble. Therefore, care must be taken when applying the oil to and preparing the surface of an airfoil for this type of test.

Generally, it was found that this particular flow visualization method provided a good qualitative understanding of the nature of the flow environment at the blade section and 2-D insert wall juncture, as well as that due to the presence of the simulated ballistic damage.

Flow visualization using a smoke wand was attempted for several test runs using the blade section for Case 1E (mid-chord damage), with the intent of further defining the 3-D behavior of the "mustache" vortices being generated by the damage. This met with only minor success, however, and the use of smoke was subsequently discontinued.

Chapter 3

Results and Discussion

To fully compare and contrast the aerodynamic characteristics of each blade specimen, various plots of the results were made. Basic plots of C_L, C_D, and C_M versus angle of attack were made for each of the blade configurations at Reynolds numbers of 1×10^6, 2×10^6, and 3×10^6. These plots were then used to examine the effect of increasing Reynolds number on each configuration. Comparisons of C_L, C_D, C_M, and Lift-to-Drag Ratio versus angle of attack were then made to identify differences and/or characteristic trends between the undamaged (baseline) airfoil sections, blade sections of the same airfoil with similar damage configurations, and blade sections composed of different airfoils with essentially the same damage configuration (See Table 6 and Fig. 20).

Comparison	Cases Compared
1	Case 1, Case 2
2	Case 1, Case 1A, Case 1B, Case 1C
3	Case 1, Case 1D
4	Case 1, Case 1E
5	Case 2, Case 2A, Case 2B, Case 2C
6	Case 1A, Case 2C
7	Case 1D, Case 1E

Table 6: Summary of Case Comparisons

In this thesis, the individual comparisons were mostly made at a Reynolds number of 2×10^6 since these measurements were the most comprehensive. Although each blade configuration was tested at a Reynolds number of 3×10^6, only angles of attack down to -5 degrees were used in order to prevent high aerodynamic loads on the test specimens and the force balance measurement system. Therefore, the number of measurements made in the negative angle of attack region at this Reynolds number were more limited. Additionally, because the SC1095 and SC1095R8 airfoils were non-symmetric, the behavior of the airfoils at high angles of attack near maximum lift (both positive and negative angles of attack) were of significant interest, and were examined in this experiment.

The results measured in the attached flow region were used to extract key aerodynamic characteristics, such as the lift-curve-slope, zero lift angle of attack, and the location of the aerodynamic center. The lift-curve-slope and zero lift angle of attack were obtained from a least squares fit to the measured data (Ref. 14) in the attached flow regime using the equation

$$C_L = \frac{dC_L}{d\alpha}(\alpha - \alpha_\circ) = C_{L_\alpha}(\alpha - \alpha_\circ) \tag{7}$$

The drag in the low angle of attack region was fitted using

$$C_D = C_{D_0} + C_{D_1}|(\alpha - \alpha_\circ)| + C_{D_2}(\alpha - \alpha_\circ)^2 \tag{8}$$

where C_{Do}, C_{D1}, and C_{D2} are constants chosen to give the best fit to the experimental blade section data (Refs. 13 and 15).

34

The nondimensional position of the aerodynamic center was obtained from the lift-curve-slope, $dC_L / d\alpha$, and the moment-curve-slope, $dC_M / d\alpha$, using

$$x_{ac} = \frac{1}{4} - \frac{dC_M}{dC_N} = \frac{1}{4} - \left(\frac{dC_M}{d\alpha}\right)\left(\frac{d\alpha}{dC_N}\right) \tag{9}$$

where C_N was computed from C_L as defined in Appendix C.

It should be noted, however, that in the attached flow region, C_L and C_N have almost the same numerical values. Thus, it is an acceptable approximation in this region to assume that C_L is equal to C_N.

The non-dimensional position of the center of pressure, x_{cp}, for each angle of attack was computed from the pitching moment coefficient about the ¼-chord, C_M, and the normal force coefficient, C_N, using

$$x_{cp} = \frac{1}{4} - \frac{C_M}{C_N} \tag{10}$$

Although not included in this thesis, the center of pressure measurements for all Reynolds numbers were found to be qualitatively similar. In the positive low angle of attack regime, the center of pressure appeared close to the ¼-chord. In fact, in every case, the center of pressure asymptoted to the location of the aerodynamic center prior to the development of flow separation and stall. After separation occurred, nominally at an angle of attack of 16 degrees, the center of pressure moved quickly aft and asymptoted to between 35 and 40 percent chord. The actual position of the center of pressure was found to be only weakly affected by the simulated

35

ballistic damage located near the trailing-edge. For the damaged cases, however, the center of pressure did tend to move forward of that for the undamaged cases, and slightly ahead of the quarter-chord. For those cases with ballistic damage close to the leading edge, a different trend developed. The center of pressure tended to asymptote to the aerodynamic center with increasing angle of attack, which was farther back on the airfoil than for the undamaged cases to those cases with damage close to the trailing edge. After separation, however, the center of pressure for all cases moved quickly aft and asymptoted to between 35 and 40 percent chord.

Note that all force and moment coefficients presented have been nondimensionalized with respect to the undamaged area of the blade section. The obvious question is to what extent the results can be reconciled by using the actual lifting area of the damaged blade specimens. These comparisons are shown in Fig. 21. Note that in the case of the lift and drag, the agreement is quite good, suggesting that as far as the force coefficients are concerned, area removal is the primary factor in reconciling the aerodynamic characteristics. However, from the lift-to-drag ratio plot in Fig. 34b, one can see that the performance is still degraded by more complex phenomena other than area removal. Similarly, the pitching moment curves in Fig. 21 cannot be reconciled on the basis of area removal. Nevertheless, it is clear from these results that area removal accounts for a substantial part of the aerodynamic degradation.

Most aerodynamicists are familiar with the standard lift, drag, and moment curves plotted herein. However, in comparing the different configurations against

undamaged (baseline) blade sections, it may be somewhat easier, in some cases, to show the results as a perturbation or deviation from the baseline characteristics (see Figs. 22a and 22b). For example, a positive value on the lift perturbation plot indicates a value of lift coefficient that much higher than that of the baseline. Similarly, a negative value indicates a perturbation value less than that of the baseline.

While the perturbation approach allows for a quick interpretation of the data when comparing different damage configurations against baseline blade sections, it is not the most common plotting method. Therefore, because most aerodynamicists are familiar with the standard lift, drag, and moment plots, this method was used here to define the aerodynamic characteristics of the different blade sections.

3.1 Effects of Increasing Reynolds Number

Both the type of stall and the maximum lift coefficient can be strongly affected by Reynolds number, as is the shape of the lift stall curve. Since we know that the Reynolds number is defined as

$$\text{Re} = \frac{\rho V c}{\mu} \tag{11}$$

where ρ is the density of air, V is the free-stream velocity, c is the chord of the airfoil, and μ is the viscosity of air, the same airfoil may perform differently when used on helicopter rotor blades with varying chords and tip speeds. For airfoils that exhibit the trailing edge stall mechanism, increasing Reynolds number is beneficial in that it results in a thinner boundary layer relative to the chord. This thinner boundary layer is more

37

resistant to the adverse pressure gradient on the airfoil and, consequently, separation. Typically, these types of airfoils will yield higher values of C_{Lmax} with increasing Reynolds number (Ref. 13).

Even at somewhat low free-stream Mach numbers, the local velocity near the leading edge of an airfoil can come close to the local speed of sound at high angles of attack, resulting in localized compressibility effects. This is manifest as higher local adverse pressure gradients at a given value of lift, and gives rise to a thickened boundary layer, which causes trailing-edge separation to occur at a lower angle of attack.

In reviewing the effects of increasing Reynolds number on each blade section, two distinct groups emerged. The undamaged blade sections and those with damage closer to the trailing-edge exhibited similar aerodynamic characteristics, as did the blade sections with damage close to the leading-edge. Figures 23 through 32 show the aerodynamic characteristics of each rotor blade section configuration, as measured at Reynolds numbers of 1×10^6, 2×10^6, and 3×10^6.

For the first group, with increasing Reynolds number, the maximum lift coefficient increased, as did the lift-curve-slope. Generally, with increasing C_{Lmax}, there was a slight increase in the stall angle. However, this increase did not manifest itself in every case. When this trend was not present, the stall angles remained the same for all Reynolds numbers. Of note here is the fact that Case 1E, with simulated damage in the form of a hole at center-chord, showed an increase in C_{Lmax} for all cases

of increasing Reynolds number whereas the other cases exhibited a decrease in C_{Lmax} when the Reynolds number was increased from 2×10^6 ($M = 0.16$) to 3×10^6 ($M = 0.24$). This decrease was attributed to localized compressibility effects developing on or near the leading-edge of the blade sections at higher angles of attack, thereby increasing the adverse pressure gradient, thickening the boundary layer, and causing trailing-edge separation to occur again at a lower angle of attack.

While differences in drag tended to be very small in the attached region, a distinct decrease in drag was noted in a small range of angle attack (approximately 18 to 22 degrees) in the post-stall region with increasing Reynolds number. Beyond this point, drag values were generally seen to converge. Finally, regardless of the slope of the C_M versus angle of attack curve in the attached flow region, every blade section exhibited an increasing nose down pitching moment with increasing Reynolds number, although some to a smaller degree than others.

For the second group of blade sections, the results were very different. For these cases, for increasing Reynolds number, there were no apparent changes to the lift-curve-slope. However, C_{Lmax} and the stall angle decreased with increasing Reynolds number. This is a result of the forward hole in each case apparently "fixing" the flow separation point. The presence of this hole in the area that produces most of the lift on the airfoil precludes any increase in the maximum lift coefficient with increasing Reynolds number.

39

Additionally, as the Reynolds number was increased, the flow through the hole (from the lower surface to the upper surface) is faster and complicates the flow over the top of the airfoil. Again, because of its location near the leading-edge, the hole contributes greatly to flow separation, and the resulting decrease in lift that is evident at higher Reynolds numbers. Of note here is that Case 2B, while exhibiting the same characteristics as Case 2A, does not realize a reduction in lift when the Reynolds number is increased from 2×10^6 to 3×10^6. Because of the petalling present around the circumference of the hole in Case 2B, it is likely that small scale vortices are being generated, effectively energizing the boundary layer on the front part of the airfoil, and preventing it from separating earlier at the higher Reynolds number.

Because of the progressive separation caused by the hole near the leading-edge, the drag increased at a much higher rate with increasing angle of attack prior to stall. While drag in this region is not effected by increasing Reynolds number, a slight increase is evident with increasing Reynolds number between 18 to 22 degrees. The drag values generally tend to converge after this point.

Finally, the shape of the pitching moment curve is unique, in that it exhibited a stair-step type decrease with increasing angle of attack. Like the first group of blade sections, there was a small increase in the nose-down pitching moment with increasing Reynolds number.

At all Reynolds numbers, every blade section appeared to exhibit a trailing-edge stall mechanism, although to varying degrees. Under these circumstances, flow

separation begins at the trailing-edge of the airfoil, and moves forward toward the leading-edge with increasing angle of attack. This mechanism can be inferred from the lift characteristics, where the lift-curve-slope shows a progressively greater nonlinear behavior near maximum lift. The stall mechanism is further confirmed by the pitching moment behavior, where the trend toward a decreasing nose down moment near maximum lift is also characteristic of airfoils that exhibit a trailing-edge stall mechanism (Ref. 13).

At the higher Reynolds numbers the stall onset was found to become more abrupt. However, the stall mechanism was still by the upstream or forward movement of trailing-edge separation. This variation with Reynolds number is characteristic of most cambered airfoils (with thicknesses greater than 10 percent of chord) in the low Mach number regime (Ref. 13).

At negative angles of attack at all Reynolds numbers, stall also appeared to be by the trailing-edge stall mechanism. Recall that in the negative angle of attack region the flow separation develops on the lower surface of the airfoil. Since, unlike the upper surface, the lower surface contour is not designed to control the high adverse pressure gradients that occur at large negative angles of attack, rapid boundary layer thickening and flow separation occur on the lower surface even at moderately low negative angles of attack. This results in a low lift-curve-slope and a fairly low value of maximum negative lift for all Reynolds numbers. Note that at the higher Reynolds numbers, however, there is a significant increase in maximum negative lift over that obtained at one million.

3.2 Rotor Blade Section Case Comparisons

A summary of the measured aerodynamic parameters for each configuration in the attached flow regime is given in Table 7.
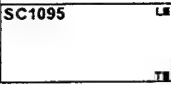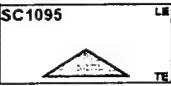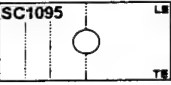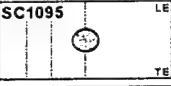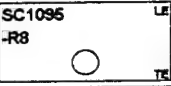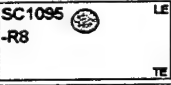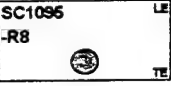
Case Number	Icon	CLa/deg	Xac	alpha0	CDo	CLmax
Case 1	SC1095	0.1057	0.2538	-0.239	0.011	1.5275
Case 1A	SC1095	0.0987	0.2488	-0.015	0.0163	1.4451
Case 1B	SC1095	0.0918	0.2278	-0.00375	0.019	1.3405
Case 1C	SC1095	0.0923	0.2392	-1.29	0.0368	1.3896
Case 1D	SC1095	0.1078	0.2519	-0.331	0.0109	1.6022
Case 1E	SC1095	0.0854	0.2459	-0.1185	0.028	1.1684
Case 2	SC1095 -R8	0.1071	0.2424	-0.4654	0.0137	1.632
Case 2A	SC1095 -R8	0.1025 0.0429	0.2711 0.3231	-0.891	0.0162	1.2579
Case 2B	SC1095 -R8	0.1004 0.0514	0.2742 0.327 0.261	-0.8951	0.019	1.2702
Case 2C	SC1095 -R8	0.0991	0.2344	-0.383	0.0184	1.6133
Note: Where more than one number appears for the same case indicates a distinct change in the lift-curve slope						

Table 7: Summary of Aerodynamic Parameters Measured at $Re = 2 \times 10^6$

3.2.1 Comparison 1 - Case 1 and Case 2
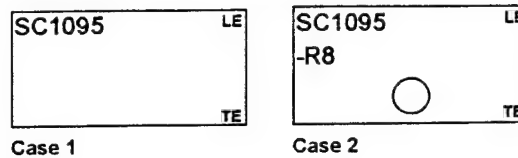
Case 1

Case 2

Figs. 33a and 33b show the measured aerodynamic characteristics of the baseline SC1095 (Case 1) and the baseline SC1095R8 (Case 2) blade sections at a Reynolds number of 2×10^6.

In the attached flow regime for both cases, the lift and pitching moment varied linearly with angle of attack, and the drag exhibited a parabolic variation. In the post-stall region for both positive and negative angles of attack, the SC1095R8 baseline exhibited a distinct rounding of the lift curve. The SC1095 airfoil (Case 1) has less camber and more symmetry than the SC1095R8 airfoil (Case 2), which tends to encourage a maximum lift peak with a more abrupt departure at stall. The SC1095R8 airfoil tends to exhibit a somewhat less severe stall at both positive and negative angles of attack due to the lower adverse pressure gradients obtained with the more highly cambered airfoil. As a result, this airfoil exhibits lower drag in the post-stall region for positive angles of attack. In the negative angle of attack region, however, the SC1095R8 (Case 2) achieves a significantly lower negative lift coefficient and suffers from much higher drag until well into the post-stall region.

The pitching moment for both cases were similar, with the baseline SC1095R8 (Case 2) exhibiting a slight increase at the point of maximum lift. The Lift-to-Drag Ratio, an effective measure of the efficiency of the blade sections, revealed that the

baseline SC1095 (Case 1) and the baseline SC1095R8 (Case 2) were quite similar in the positive angle of attack region but that the baseline SC1095R8 (Case 2) was a significantly poorer performer in the negative angle of attack region.

3.2.2 Comparison 2 - Case 1, Case 1A, Case 1B, and Case 1C
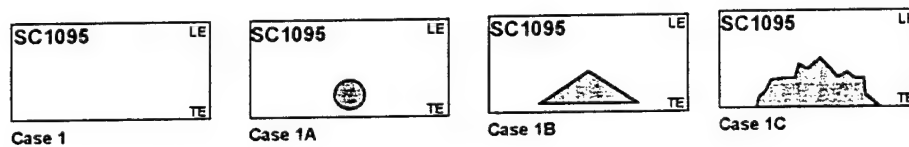
Figs. 34a and 34b show the measured aerodynamic characteristics of the rotor blade sections in Case 1, Case 1A, Case 1B, and Case 1C as measured at a Reynolds number of 2×10^6.

Using Case 1 as the baseline configuration, the effect of different damage (in terms of size) on the same airfoil is evident in this comparison. In the attached flow region for all cases, the lift and pitching moment all vary linearly with angle of attack and the drag exhibits a parabolic variation. As the damaged area increased from Case 1A to Case 1B, the lift-curve-slope showed a distinct decrease, as did the maximum lift coefficient. Of note here is that while the maximum lift decreased from Case 1 to Case 1A, the stall angle remained the same. Case 1B stalled nearly 1 degree higher. Case 1C, with actual ballistic damage, achieved a higher maximum lift coefficient than Case 1B but stalled 2 degrees lower. Because Case 1C had more surface area despite the actual ballistic damage than Case 1B, this was not a surprise. The "roughness" of

44

the damage on Case 1C probably caused separation to occur at the trailing edge at a lower angle of attack.

Generally, the drag for Case 1, Case 1A, and Case 1B was quite similar. A close inspection of the drag curve, however, reveals a notable increase in drag for the damaged cases. The drag increase for Case 1A is 1.5 times that of the undamaged (baseline) blade section in the attached flow region, while the drag for Case 1B is 1.7 times that of the baseline. For Case 1C, the displaced ply material caused more severe local separation as is evident by the substantial increase in drag for this case. While the long strands of surface ply material have the potential of generating high drag it is expected that on a rotor system, blade centrifugal and aerodynamic loads will cause most of these strands to peel along the ply lay-up angle to the trailing edge, and separate from the blade. In this experiment, many of the composite fragments did separate from the blade section during the wind tunnel test. However, numerous strands remained attached to the blade section, contributing further to the sectional drag increase 3.4 times higher than that of the baseline.

Of note here is that the drag-curve-slope for Case 1B decreased at about 20 degrees angle of attack, and remained linear beyond this point. This is most likely a result of the larger hole size for this configuration.

The pitching moment curves show that Case 1B and Case 1C share similar linear behavior until approximately 8 degrees, at which point Case 1B continues to increase at the same rate while Case 1C returns to zero. Note also that, with the loss of lifting area on the aft portion of these blade sections, the slope of the pitching

45

moment curves for Case 1B and Case 1C increased due to a forward shift of the aerodynamic center.

The Lift-to-Drag Ratio revealed that, as expected, Case 1A and Case 1B are perhaps twice as efficient as the specimen with the actual ballistic damage (Case 1C). Again, Case 1C is subjected to significantly more drag considering the severe surface discontinuities incurred by the actual ballistic damage.

3.2.3 Comparison 3 - Case 1 and Case 1D
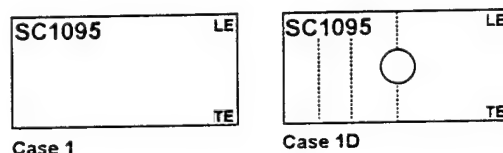
Case 1   Case 1D

Figs. 35a and 35b show the measured aerodynamic characteristics of the rotor blade sections in Case 1 (the baseline SC1095) and Case 1D as measured at a Reynolds number of 2×10^6.

Because this blade section consists predominately of the SC1095 airfoil, it exhibited the same characteristics as the blade section in Case 1, but with several exceptions.

Not surprisingly, at negative angles of attack, Case 1D exhibited a progressive rounding of the lift-curve-slope resulting in a fairly low value of maximum negative lift. This behavior was similar to that of the baseline SC1095R8. This was not surprising considering that the rightmost 2 inches (0.1c) of this blade section was comprised of a SC1095R8 airfoil.

46

The Lift-to-Drag Ratio indicates almost total similarity between these two cases with the exception of the negative angle of attack region where the SC1095R8 airfoil tended to promote early flow separation. This caused a significant rise in drag with a direct negative impact on the Lift-to-Drag Ratio.

3.2.4 Comparison 4 - Case 1 and Case 1E
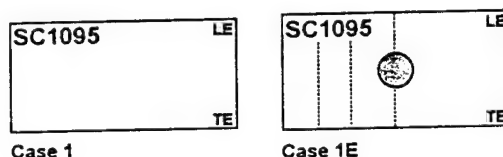
Case 1   Case 1E

Figs. 36a and 36b show the measured aerodynamic characteristics of the rotor blade sections in Case 1 (the baseline SC1095) and Case 1E as measured at a Reynolds number of 2×10^6.

Considering the lift, it is clear that the lift-curve-slope and maximum lift coefficient are significantly less for Case 1E than for the baseline SC1095 (Case 1D). In fact, with the simulated ballistic damage on the mid-chord of the blade section, maximum lift decreased 24 percent from the baseline (undamaged) SC1095 specimen This is a result of flow separation occurring at the upstream edge of the hole.

Note also that the overall stall characteristic for Case 1E exhibited a more gradual rounding of the lift curve near maximum lift. The possible premature onset of trailing-edge separation due to the existence of the damage (a hole in this case) limits the build-up in circulation, reducing the maximum attainable value of lift. The angle of

47 .

attack corresponding to the maximum lift coefficient was relatively unaffected by the damage.

Because the effects of the damage may promote premature trailing edge separation, the corresponding pitching moment behavior appears as a small nose-up moment trend near the stall angle of attack. This is because the aerodynamic center moved forward 1 percent of the blade chord.

Of all of the aerodynamic load components, the effects of damage on the drag coefficient were perhaps the most significant. In the low angle of attack regime, the drag was approximately 2.5 times higher than that of the baseline airfoil. Again, this is due to the premature onset of trailing-edge flow separation for a given angle of attack, which limits the build-up of circulation, reduces the leading-edge suction, and increases the pressure drag at a given angle of attack.

3.2.5 Comparison 5 - Case 2, Case 2A, Case 2B, and Case 2C
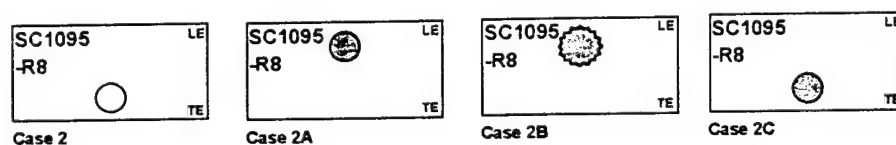
Figs. 37a and 37b show the measured aerodynamic characteristics of the rotor blade sections in Case 2 (the baseline SC1095R8), Case 2A, Case 2B, and Case 2C as measured at a Reynolds number of 2×10^6.

Two comparisons can be made here. First, the effect of damage towards the leading-edge and, second, the effect of damage near the trailing-edge.

The baseline SC1095R8 (Case 2) and Case 2C exhibited the same characteristics as Case 1 and Case 1A, the only difference being a definitive increase in lift for a given angle of attack, again resulting from the more highly cambered SC1095R8 airfoil. In the attached flow region for Case 2 and Case 2C, the lift varied linearly with angle of attack, and the drag exhibited a parabolic variation. In the post-stall region, note that the lift-curve-slope exhibited a gradual decline. The pitching moment also exhibited a fairly linear variation, but tended to show a positive increase with increasing angle of attack with a more significant upturn towards the stall angle. At negative angles of attack, each case exhibits a progressive rounding of the lift-curve-slope and a very low value of maximum negative lift compared to previous cases.

The interesting comparison here, however, is between the baseline (Case 2), and the blade sections with damage towards the leading-edge (Case 2A and Case 2B). The blade sections with ballistic damage near the leading-edge behaved quite differently than those with trailing-edge damage. First, note that while the lift-curve-slope varies linearly for each case, the lift-curve-slope for Case 2A and Case 2B decreases dramatically at approximately 6 degrees, and remained linear after this point until stall. At stall, both Case 2A and Case 2B exhibited a relatively smooth rounding-off of the lift-curve-slope. While reaching a lower maximum lift coefficient than Case 2, the stall angle for Case 2A and Case 2B is at least 3 degrees higher. This "kink" in

the lift-curve-slope is most likely the result of increased flow from the lower surface, up through the hole, to the upper surface at higher angles of attack. This tends to "fix" the point of flow separation over the range from lower angles of attack through the stall angle of Case 2.

The blade section with "petalling" (Case 2B) achieved a slightly higher maximum lift coefficient (1 percent) than did the "non-petalled" specimen (Case 2A). Again, because of the "petalling" present around the circumference of the hole in Case 2B, it is likely that small scale vortices were generated, effectively energizing the boundary layer on the front part of the airfoil, and prevented it from separating as early as Case 2A.

The drag for the forward damaged blade sections (Case 2A and Case 2B) exhibited a fairly linear increase from approximately 6 degrees until stall, growing from 1.4 to 2.5 times higher than the baseline (Case 2). Note that the petalling in Case 2B resulted in a slight increase in drag over that of Case 2A.

The pitching moment for Case 2A and Case 2B reflects a "stair-step" decrease with increasing angle of attack due to an aft movement of the aerodynamic center. Interestingly, the center of pressure for these two cases tended to stabilize between 0.32c and 0.35c in the positive angle of attack range up to stall. In the post-stall region, the center of pressure approached that of Case 2 and Case 2C, and assumed the same gradual increase in magnitude to approximately 0.45c.

The Lift-to-Drag Ratio indicates that while the blade section with aft damage is only 20 percent less efficient than the baseline, Case 2A and Case 2B are close to four times less efficient in the positive angle of attack region. It can be concluded, then, that the aerodynamic degradation for the same size hole becomes catastrophic as the hole moves forward along the chord.

Of note here is the possibility that some of the difference in performance between the blade sections with trailing-edge damage and leading-edge damage could be a result of increased cavity flow for Case 2A and Case 2B. These leading-edge damage blade sections had damage (circular holes in this case) cut through the hollow spar of the blade, which may have allowed the flow to expand spanwise into the spar. The damage for Case 2C (also a circular hole) was cut in a solid honeycomb region of the blade section which prevented any expansion of the flow from the lower to the upper surface.

3.2.6 Comparison 6 - Case 1A and Case 2C
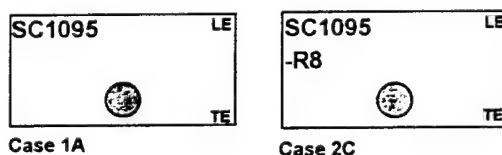
Case 1A   Case 2C

Figs. 38a and 38b show the measured aerodynamic characteristics of the rotor blade sections in Case 1A and Case 2C, as measured at a Reynolds number of 2×10^6.

The type and extent of the damage for these two cases is essentially the same. However, the airfoil shapes are different (see Fig. 7). Comparing these results to the

Case 1 and Case 2, it is evident that while the magnitude of the curves is smaller for the damaged cases, the trends are almost identical to those of Case 1 and Case 2.

3.2.7 Comparison 7 - Case 1D and Case 1E
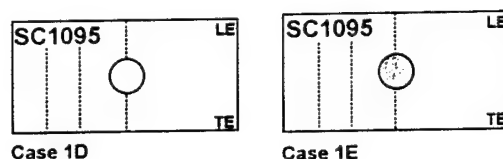
Case 1D   Case 1E

Figs. 39a and 39b show the measured aerodynamic characteristics of the rotor blade sections in Case 1D and Case 1E as measured at a Reynolds number of 2×10^6.

Because of the similarity in the aerodynamic characteristics between the blade section used for Case 1 and that in Case 1D, the results of this comparison are essentially the same as that of Case 1 and Case 1E.

Additional tests were conducted for each of these cases in an attempt to identify any possible static hysteresis effects. In the interest of minimizing the total time required to complete the experiment, data were only taken for increasing and decreasing sweeps in angle of attack at a Reynolds number of one million. The results are shown in Figs. 40 and 41. For Case 1D, the plots for increasing and decreasing angles of attack were virtually identical, with no visible hysteresis behavior. However, for Case 1E, static hysteresis was evident in the post-stall region from approximately 16 to 22 degrees angle of attack. As noted previously, this behavior is the result of the differences in the physical processes of flow separation versus flow reattachment.

3.3 Aerodynamic Characteristics in the High Angle of Attack Regime

Figs. 42a, 42b, and 42c show the results of tests over a full 360 degrees angle of attack for the rotor blade sections in Case 1D and Case 1E as measured at a Reynolds number of 1×10^6. Tests at higher Reynolds numbers were not conducted due to the large unsteady loads and severe buffeting associated with the flow about the airfoil at large angles of attack.

For angles of attack greater than 30 degrees, there was massive flow separation over the leeward surface of the wing. Under these conditions, the flow is unsteady, and the loads vary in a more random fashion. It is possible, however, for the flow to "lock-in" at certain angles of attack and produce periodic vortex shedding. This can induce large periodic loads on the wing, support structure, and balance system.

In the post stall regime, the lift coefficient increased again beyond C_{Lmax}, and then progressively reduced in magnitude up to 90 degrees angle of attack. The effects of damage obviously had only a small influence on the lift in the post-stall regime since the flow was completely separated on the top surface in both cases. On the other hand, both the pitching moment and the drag showed a somewhat larger effect of ballistic damage. Here, the effects of damage caused the center of pressure to remain slightly less aft on the chord than for the undamaged case, resulting in lower pitching moments. Due to the reduced cross-sectional area of the damaged wing, the peak

53

drag coefficient for the damaged blade section was about 20 percent lower than for the baseline blade section.

Note that for angles of attack between 100 degrees and 130 degrees, the measurements show somewhat more scatter. This is a result of the occurrence of periodic vortex shedding from the blade section over this angle of attack range, as mentioned previously.

3.4 Aerodynamic Characteristics in Reverse Flow

In high speed forward flight, the inboard sections of the retreating blade of the rotor experience reverse flow. This occurs because the forward flight velocity is greater than the local velocity at the inboard blade elements.

In reverse flow, the sharp trailing-edge of the blade points into the relative wind, and the rounded nose of the airfoil becomes the trailing-edge. Because of the sharp leading-edge, the onset of significant separation and stall occurs at a relatively low angle of attack, with a correspondingly low value of maximum lift. This is the case for both negative and positive angles of attack. Furthermore, although the dynamic pressure in the reverse flow region is relatively small, the center of pressure moves to the vicinity of the ¾-chord location. This may produce a significantly higher blade pitching moment.

Figs. 42a, 42b, and 42c show the results of tests over a full 360 degrees angle of attack for the rotor blade sections in Case 1D and Case 1E as measured at a

54

Reynolds number of 1×10^6. Note that both blade sections produced a significant amount of lift, even while operating in the reverse flow region. However, the relaxation of the Kutta condition (accompanied by the separation at the now "blunt" trailing-edge) produced higher drag in reverse flow. Both the zero-lift drag coefficient and the increase in drag with increasing angle of attack were found to be much larger than when the airfoil was operating in the normal flow regime. The effects of the damage were somewhat minor when the airfoil was operating in the reverse flow regime since the sharp leading-edge and blunt trailing-edge already significantly degrade the aerodynamic performance.

The aerodynamic center was expected to move to the vicinity of the three-quarter chord in the reverse flow region. However, since the aerodynamic center is only relevant for the attached flow region, the center of pressure was used. For both blade configurations, the center of pressure appeared to asymptote to between 0.55c and 0.6c immediately prior to and immediately after the blade section rotated through the +/- 180 degree position. Although not coincident with the three-quarter chord as expected, the aft center of pressure resulted in a significant increase in the pitching moment for both blade sections. Additionally, while the pitching moment curve in the attached flow region had a low slope (corresponding to an aerodynamic center at the quarter-chord), the slope was magnified tremendously in the reverse flow region. This resulted in extremely large changes in pitching moment with relatively small changes in angle of attack.

3.5 Oil Flow Visualization

A substantial number of flow visualization experiments were carried out at various angles of attack up through and beyond stall. The results were recorded on conventional T-MAX 400 ASA black and white film, as well as Super VHS video tape. As noted previously, the video was particularly useful for recording the flow patterns on the blade sections given the somewhat dynamic and unsteady behavior of the flowfield near stall, or in the separated flow near the damaged region of the blade section.

Sample flow visualization results are shown in Figs. 43 through 48. Note that, in general, the presence of the simulated ballistic damage caused flow separation at the upstream edges of the hole, even at low angles of attack. This is reflected in the drag measurements shown previously in Figs. 33 through 39, by which the increased separation produces an energy loss that shows up as an increase in drag. Often, a pair of counter-rotating vortices were formed at the upstream edge of the damaged region

For increasing angle of attack, the region of flow separation expanded over a larger part of the trailing edge of the blade section. Note also that the oil on the outer span shows that the flow over the outer (attached flow) part of the wing is affected, with the flow being directed somewhat more towards the insert walls. These results confirm that the effects of ballistic damage are not necessarily confined to regions in the immediate vicinity of the damage. Rather, the aerodynamic effects of ballistic damage may be felt over a span perhaps as much as twice that of the dimensions of the damage.

56

In these tests, the laminar separation bubble remained present throughout the entire range of angles of attack. This is observed by an accumulation of oil in a narrow band near the leading edge. This confirmed that the stall mechanism was not leading edge stall, often initiated by the bursting of the separation bubble, but rather the forward movement of the trailing-edge separation. Of note here is that as the angle of attack increased, the separation bubble moved well forward onto the leading edge. As the bubble transitioned forward, it became much narrower, in some cases by as much as one-third its original size.

The flow visualization photographs also captured well-formed "scarf" vortices influencing the flow-field on and near the 2-D insert walls (Figs. 5 and 6). Note in these photographs the well-defined areas of separated flow caused by the vortices. These vortices became somewhat more prominent at higher angles of attack near stall, expanding outwardly along the span by as much as 2 inches (8 percent span). In comparison, the "scarf" vortices acting on the blade section in Case 1A appear to be much larger for the same angle of attack than those acting on the blade section in Case 2C (Figs. 44 and 48). Care must be taken in interpreting these effects, however. It is known from previous discussion that the blade section in Case 1A, made up of the SC1095 airfoil, stalls before and achieves a lower maximum lift coefficient than the Case 2C blade section, made up of the SC1095R8 airfoil. Thus, when looking at the apparent effect that the "scarf" vortices have on each of these blade sections, a conclusion might be drawn that these vortices cause this difference in lifting capability. This conclusion would be wrong, however, as the airfoil shape influences the behavior

of the vortices and not vice versa. Since the SC1095 is more symmetric than the SC1095R8 and exhibits much less leading-edge camber, it is expected that separation will be more abrupt, and will occur sooner than with the SC1095R8 airfoil. Consequently, the "scarf" vortices on the SC1095 will exhibit more of a spanwise growth on the SC1095 at a given angle of attack because of the earlier onset of flow separation.

3.6 Blade Section Pressure Profiles

Two sets of comparisons were made with the pressure profiles. First, pressure profiles for both Case 1D and Case 1E were compared for each spanwise location at angles of attack of 5, 10, 14, and 16 degrees (Figs. 49 through 52). The intent here was to identify the differences in pressure profile between a damaged and an undamaged blade section. Second, the three spanwise pressure profiles for each individual case were compared at the angles of attack discussed earlier to identify any trends towards spanwise flow (Figs. 53 through 60). These plots were further compared to oil flow visualization photographs to further clarify the characteristics of the flow-field as it related to the changes in the pressure profiles.

Note that for the comparison of span 3 at 14 degrees angle of attack, there is fully-attached flow on the undamaged (Case 1D) blade section evident by the classic airfoil pressure profile. However, for Case 1E, the flow is separated behind the hole, evident by the fairly constant negative pressure measured there. Additionally, in separated flow regions, the negative pressure tends to be slightly higher than that of

58

the attached flow region. This is also evident when comparing Case 1D and Case 1E at 14 degrees angle of attack. At the higher angle of attack (16 degrees), both cases exhibit flow separation over most of the blade chord, again evident by the fairly constant negative pressure distribution along the chord. Note here that the flow remains attached longer on the damaged blade section, separating possibly 0.2c farther back along the chord than the undamaged case.

In looking at possible spanwise flow, there appears to be no 3-D flow effects for Case 1D at an angle of attack of 14 degrees. However, for Case 1E, the pressure profiles are different at each spanwise location. This indicates that the damage does, in fact, cause spanwise flow.

3.7 A Comparison of Force Balance Data and Integrated Pressure Data

As described previously, 58 pressure taps (33 on the upper surface and 25 on the lower surface) were installed in the blade section used for Cases 1D and 1E. This made it possible to compare the force balance results with similar results derived from the integration of the pressure measurements. The normal force, leading-edge suction force (axial force), and the pitching moment were obtained by integrating the local pressure around the airfoil at each spanwise location. This yielded results for each of the three discrete spanwise locations on the airfoil, and was used to validate the degree of two-dimensionality of the force balance results obtained for the entire blade section.

The normal, axial (suction), and moment coefficients can be written in terms of the differential pressure coefficient, ΔC_P, as

$$C_N = \int_0^c (C_{Pl} - C_{Pu}) d\left(\frac{x}{c}\right) = \int_0^c \Delta C_P d\left(\frac{x}{c}\right) \qquad (12)$$

$$C_A = \int_0^c \left(C_{Pu} \frac{dy_u}{dx}\right) d\left(\frac{x}{c}\right) - \int_0^c \left(C_{Pl} \frac{dy_l}{dx}\right) d\left(\frac{x}{c}\right) \qquad (13)$$

$$C_M = -\int_0^c (C_{Pl} - C_{Pu}) \left(\frac{x}{c}\right) d\left(\frac{x}{c}\right) = -\int_0^c \Delta C_P \left(\frac{x}{c}\right) d\left(\frac{x}{c}\right) \qquad (14)$$

where C_{pl} and C_{pu} are the pressure coefficients measured on the lower and upper surfaces, respectively (Ref. 10). Resolving the normal and axial forces in the lift and drag directions yields

$$C_L = C_N \cos\alpha + C_A \sin\alpha \qquad (15)$$

$$C_D = C_N \sin\alpha + C_A \cos\alpha \qquad (16)$$

It should be noted, however, that the accuracy with which the numerical values of C_N, C_A, and C_M can be computed is very dependent on the number and location of the pressure taps on the airfoil surface. For subsonic flow, the pressure peak and high adverse pressure gradients occur near the leading edge. However, at higher subsonic speeds, the largest pressure gradient occurs somewhat farther downstream of the leading edge.

For this experiment, it was possible to install only a limited number of pressure taps in the blade section. Most of pressure taps were placed in positions around the ballistic damage to quantify its effect on the local flow-field. Unfortunately, only one pressure tap was installed close enough to the leading-edge to properly capture the

suction pressure peak. Positioned on the mid-span, this pressure tap was positioned 0.5 inches (0.024c) from the leading edge of the blade section. From the measured pressure profiles in Figs. 49 through 52, it is apparent that this is the general location of the leading edge pressure peak. It is important to note, then, that the decrease in magnitude of the pressure profiles of span 1 and span 2 is not an aerodynamic phenomena, but rather simply a result of the lack of pressure taps in the leading edge region of the blade section at these two spanwise locations.

To maintain accuracy when calculating C_N, C_A, and C_M from few pressure taps, special interpolation methods are used, as shown in Appendix D. These interpolation methods, or transformations, have the effect of removing the leading-edge pressure peak (for subsonic flow), and effectively smoothing out the chordwise pressure distribution as shown in Figs. 61 and 62.

Note that using transformations usually leads to a higher accuracy in C_N and C_M when sparse numbers of pressure taps are involved (Ref. 16). The transformation shown in Appendix D also had the effect of removing the fictitious point at leading-edge where the pressure coefficient was assumed to be zero (Figs. 61 and 62).

Because of the inability of the pressure taps to completely resolve the surface pressure around the leading and trailing edges of an airfoil in sufficient detail, the integration of surface pressures generally cannot be used to obtain a realistic assessment of the drag coefficient. This is evident when comparing the force balance data with that derived from the pressure measurements as shown in Figs. 63 and 64. Again, because of the lack of pressure taps at the leading and trailing edges, the

integration of the pressure differential in computing C_A is only qualitatively correct. Additionally, in the calculations for Case 1D and Case 1E, the pressure was arbitrarily set to zero at both the leading and trailing edges as well as over the chordwise length of the hole in Case 1E. The zero pressure assumption over the hole resulted in a lower C_{Lmax} when using the pressure integration method compared with that derived from the force balance data.

Generally, there was good agreement between the force balance and the pressure data for the lift and moment coefficients as seen in Figs. 63 and 64. For Case 1D, both sets of data corresponded well at all three spanwise locations. These results indicate that the force balance results are very representative of 2-D flow. This justifies the continued use of the force balance system to gather force data for blade sections instead of using pressure taps, which would be costly and time consuming.

The force balance and pressure data for the lift and moment coefficients also corresponded well for Case 1E except at span 3, which was the location of the hole. This indicates that a blade section with damage does, in fact, exhibit characteristics of 3-D flow. However, the extent of the three-dimensionality of the flow is a function of many factors to include the chordwise location of the damage and the angle of attack of the blade section. Based on the results in Fig. 64, it can be concluded that most of the aerodynamic degradation due to damage on this blade section occurred on or near the spanwise location of the damage. Also note that should this flowfield be modeled using CFD techniques, a 3-D model must be used to accurately predict the aerodynamic characteristics of the blade section.

The force balance and pressure data for the drag coefficient did not agree as a result of shortcomings integrating pressure data to obtain the axial (suction) force, as discussed earlier.

3.8 Using Kirchhoff Theory to Predict Reductions in Lift-Curve-Slope

The prediction of maximum lift on an airfoil is difficult under any circumstances. However, it is possible to estimate the reduction in lift curve slope of an airfoil with a fixed separation point by a very general application of Kirchhoff theory (Ref. 17).

If it is assumed that the airfoil is sufficiently thin that it can be approximated by a flat plate, then Kirchhoff theory gives the following relationship between the lift coefficient, the angle of attack, and the trailing edge separation point

$$C_L = \frac{dC_L}{d\alpha}\left(\frac{1+\sqrt{f}}{2}\right)^2 (\alpha - \alpha_\circ) \tag{17}$$

where f is the non-dimensional location of the effective separation point of the flow (say, the leading-edge of the hole in this work), and $dC_L/d\alpha$ is the lift-curve-slope of the undamaged airfoil section.

For example, it can be assumed for Case 1E that the mean effective flow separation point for the blade section is fixed at the leading-edge of hole (0.482c). The reduction in lift-curve-slope can be approximately estimated by substituting the

fixed separation point from Case 1E, $f = 0.482$, into Eqn. 17. This gives the effective

lift-curve-slope of the damaged airfoil as

$$\left(\frac{dC_L}{d\alpha}\right)_{damaged} = \left(\frac{1+\sqrt{0.482}}{2}\right)^2 \left(\frac{dC_L}{d\alpha}\right)_{undamaged} = 0.718\left(\frac{dC_L}{d\alpha}\right)_{undamaged} \qquad (18)$$

This result compares very favorably with the measured reduction in lift-curve-slope for

Case 1E at $Re = 2 \times 10^6$ (see Table 8), overpredicting the measured reduction by only

11 percent.

A review of Table 8 indicates that, with one exception, the estimated

reductions were within 13 percent of the actual reductions. While this still leaves an

unacceptable margin for error for predicting versus measuring performance

degradations, the closeness of the measurements indicate that the development of an

empirical performance prediction method may be plausible.

Case Number	Measured Lift-Curve-Slope	f	Predicted Lift-Curve-Slope	% Difference
Case 1A	0.0987	0.6510	0.0863	12.59
Case 1B	0.0918	0.6250	0.0847	7.71
Case 1C	0.0923	0.7590	0.0925	-0.24
Case 1E	0.0854	0.4820	0.0759	11.18
Case 2A	0.1025 0.0429	0.1590	0.0524	-22.11
Case 2B	0.1004 0.0514	0.1590	0.0524	-1.92
Case 2C	0.0991	0.6490	0.0873	11.92

Table 8: Summary of Kirchhoff Theory Results in Predicting Reduction of Lift-Curve-Slope

Note, however, that using Kirchhoff theory for the ballistic damage problem must still be validated. In this experiment, only the chordwise location of the ballistic damage was varied. Varying the size of the ballistic damage of similar shapes at the same chordwise location must still be investigated in order to arrive at a suitable estimation of the flow separation point. Additionally, varying the spanwise dimension of the damage must also be part of further investigation to study its impact on the predicted values. This will require further experimental measurements to determine the actual aerodynamic characteristics as a function of hole size (in both the chordwise and spanwise dimensions) and chordwise position.

Chapter 4

Summary and Conclusions

Tests were made in a 2-D insert at the University of Maryland's Glenn L. Martin subsonic wind tunnel to measure the effects of ballistic damage on the aerodynamic characteristics of several helicopter rotor blade sections. Tests were conducted on two undamaged blade sections comprised of the SC1095 and the SC1095R8 airfoils, respectively. Tests were then conducted on the same sections, but with several simulated ballistic damage configurations. These comprised of a circular hole with a the surrounding skin removed to expose the internal honeycomb structure, fore and aft circular holes, and an aft wedge-shaped hole. Tests were also conducted on one blade section that had sustained actual ballistic damage near the trailing edge.

The sectional lift, drag and pitching moment were measured at angles of attack up through stall at Reynolds numbers of one, two, and three million. Pressure measurements were also made for two configurations (Case 1D and Case 1E) fitted with pressure taps. Additional tests were conducted over a full 360 degree range in angle of attack for a Reynolds number of 1×10^6. The measurements were complemented by oil flow visualization on the upper and lower portions of the blade sections.

4.1 Conclusions

The following conclusions have been drawn from this study:

1. The overall aerodynamic characteristics of the damaged sections were found to be significantly degraded, with drag being affected the most. The severity of this degradation increased as the damaged area moved forward along the blade chord, as well as with the increasing size of the damaged area (a result of a loss of lifting area and increased cavity flow).

2. In general, the lift-curve-slope decreased by varying degrees depending on the damage configuration, drag always increased, and the aerodynamic center moved forward or aft depending on the chordwise position of the damage.

3. With simulated ballistic damage on the aft portion of the blade section, the maximum lift decreased 12 percent from the baseline (undamaged) SC1095 specimen, but only 1 percent from the baseline (undamaged) SC1095R8 specimen. In each case the lift-curve-slope decreased by as much as 13 percent from the baseline. Drag for the SC1095 blade sections was approximately 1.7 times higher than that of the baseline airfoil, while the drag for the SC1095R8 blade sections was approximately 1.3 times higher than that of the baseline. The aerodynamic center moved forward by as much as 3 percent of the blade chord.

4. With actual ballistic damage on the aft portion of the blade section, the maximum lift decreased 9 percent from the baseline (undamaged) SC1095 specimen, while the lift-curve-slope decreased by 13 percent from the baseline. Drag was

67

approximately 3.4 times higher than that of the baseline, and the aerodynamic center moved forward approximately 2 percent of the blade chord.

5. With simulated ballistic damage on the mid-chord of the blade section, the maximum lift decreased 24 percent from the baseline (undamaged) SC1095 specimen, while the lift-curve-slope decreased by 19 percent from the baseline. Drag was approximately 2.5 times higher than that of the baseline, and the aerodynamic center moved forward only 1 percent of the blade chord.

6. With simulated ballistic damage on the forward portion of the blade section, the maximum lift decreased 23 percent from the baseline (undamaged) SC1095R8 specimen, while the lift-curve-slope decreased by as much as 60 percent from the baseline. Drag ranged from approximately 1.4 to 2.5 times higher than that of the baseline in the attached flow region with increasing angle of attack. The aerodynamic center moved aft by as much as 9 percent of the blade chord. The "petalled" configuration, surprisingly, resulted in a slightly higher maximum lift (about 1 percent), but a higher drag (1.2 times) than the "non-petalled" configuration.

7. The lift-curve-slope decreased with the forward movement of the damage.

8. The integrated pressure data was in excellent agreement with the force balance data. This confirmed the validity of using force balance measurements as representative of 2-D flow. Additionally, the integrated pressure data revealed that while 3-D (spanwise) flow was characteristic of the damaged blade sections, it

occurred mostly near the mid-chord with the outer spanwise locations being more representative of 2-D flow.

9. Oil flow visualization confirmed the stall mechanism to be trailing-edge stall (forward movement of separation from the trail-edge) in all cases, despite the sometimes abrupt nature of the stall characteristics of some blade sections. This was further confirmed by the presence of a laminar separation bubble on every blade section up through and beyond stall.

10. Oil flow visualization revealed that the damage caused large effects on the local flowfield. Separation was generally initiated at the upstream leading-edge of the damage, followed by a growth in separation, both in span and intensity, with increasing angle of attack.

11. Oil flow visualization showed that the circular damaged regions produced "mustache" vortices that extended over a progressively larger area of the blade as the damage moved forward along the chord.

12. Oil flow visualization also showed that for increasing angles of attack, the "mustache" vortices produced by the damaged region grew in intensity and extended over a progressively larger part of the blade span.

13. In the case of similar damage on blade sections with different airfoils, the differences in aerodynamic characteristics were similar to the differences in the baseline (undamaged) SC1095 and SC1095R8 blade sections.

14. The use of Kirchhoff theory to develop an empirical performance prediction method for the airfoils subjected to ballistic damage may be plausible.

4.2 Recommendations

The following recommendations are made for continued research based on the conclusions drawn from this study:

1. The current work focused primarily on the effects of damage based on location. In future research, it is suggested that the location of the damage be fixed. Then it would be possible to study the effects of systematically varying the size of the damaged area.

2. In future research, conduct similar tests at higher Reynolds numbers and Mach numbers to further isolate their effects on the SC1095 and SC1095R8 airfoils.

3. Pursue the development of an empirical 2-D model for determining the aerodynamic characteristics of damaged airfoils.

4. Static airfoil measurements are not always representative of helicopter rotors, which operate in a dynamic and unsteady aerodynamic environment. To validate the use of static results as a basis for helicopter performance predictions, the wind tunnel testing could be expanded to include measurements of the unsteady aerodynamic characteristics of the damaged blade sections.

5. In future research, input the sectional effects of the damaged blade sections into a 3-D rotor model (e.g., UMARC) and conduct a parametric study with emphasis on blade loads, blade aeroelastic stability, and overall rotor system performance.

Appendix A

Damage Configurations Tested in Ref. 6

Damage Configurations
1A15-2A15
1A15-3A15
1A10-2A10
1A10-3A10
2B15-4C15
2B15-5C15
2E15-4G15
2E15-5G15
2A15-3A15
2A15-4A15
2A15-5A15
3A15-5A15
2A10-3A10
2A10-4A10
2A10-5A10
3A10-5A10

Table 9: Damage Configuration Codes (see Table 10)

Hole Location	Hole #	Location	
	1	Leading edge	
	2	.25 chord, upper surface	
	3	.70 chord, upper surface	
	4	.25 chord, lower surface	
	5	.70 chord, lower surface	
Lip Type	Symbol	Type of Lip	Flange Depth
	A	flush with surface	none
	B	protruding from upper surface	1/2 inch
	C	receding into upper surface	1/2 inch
	D	scoop protruding from lower surface	1/2 inch
	E	scoop protruding from lower surface	1 inch
	F	spoiler protruding from upper surface	1/2 inch
	G	spoiler protruding from upper surface	1 inch
Hole Size	Numeral	Hole Diameter	
	10	.10 chord	
	15	.15 chord	

Table 10: Key to Damage Configuration Codes (see Table 9)

Appendix B

Damage Configurations Tested in Ref. 5

| Case # | Impact Location | | Fired From |
	Span (% x/R)	Chord (x/c)	
1	28	0.36	above and aft of the blade
2	56	0.36	above and aft of the blade
3	90	0.36	above and aft of the blade
4	28	0.41	above and aft of the blade
5	56	0.41	above and aft of the blade
6	28	0.48	above and aft of the blade
7	56	0.48	above and aft of the blade
8	90	0.48	above and aft of the blade

Table 11: Actual Ballistic Damage Configurations

Appendix C

Definition of Aerodynamic Force Components

By resolving the normal and axial forces (see Fig. 65) in the lift and drag direction, we see that

$$C_L = C_N \cos\alpha + C_A \sin\alpha \tag{19}$$

$$C_D = C_N \sin\alpha - C_A \cos\alpha \tag{20}$$

In order to solve for the normal coefficient we can write these equations in matrix form where

$$\begin{Bmatrix} C_L \\ C_D \end{Bmatrix} = \begin{bmatrix} \cos\alpha & \sin\alpha \\ \sin\alpha & -\cos\alpha \end{bmatrix} \begin{Bmatrix} C_N \\ C_A \end{Bmatrix} = [A] \begin{Bmatrix} C_N \\ C_A \end{Bmatrix} \tag{21}$$

Then, through simple matrix manipulation, we see that

$$\begin{Bmatrix} C_N \\ C_A \end{Bmatrix} = [A]^{-1} \begin{Bmatrix} C_L \\ C_D \end{Bmatrix} = \begin{bmatrix} \cos\alpha & \sin\alpha \\ \sin\alpha & -\cos\alpha \end{bmatrix} \begin{Bmatrix} C_L \\ C_D \end{Bmatrix} \tag{22}$$

Hence,

$$C_N = C_L \cos\alpha + C_D \sin\alpha \tag{23}$$

Appendix D

Transformation of Pressure Data

Applying the following transformation

$$C_P^* = C_P\sqrt{\frac{x}{c}} \qquad (24)$$

$$\frac{x^*}{c} = \sqrt{\frac{x}{c}} \qquad (25)$$

the normal and moment coefficients, in terms of the transformed variables, become

$$C_N = 2\int_0^c \left(C_{Pl}^* - C_{Pu}^*\right)d\left(\frac{x^*}{c}\right) \qquad (26)$$

$$C_M = -2\int_0^c \left(C_{Pl}^* - C_{Pu}^*\right)\left(\frac{x^*}{c}\right)^2 d\left(\frac{x^*}{c}\right) \qquad (27)$$

Bibliography

[1] Atkinson, D. B., Ball, R. E., "A History of the Survivability Design of Military Aircraft," AIAA 95-1421, 36th Annual AIAA/ASME/ASCE/AHS/ASC Structures, Structural Dynamics and Materials Conference, New Orleans, LA, April 1995.

[2] Foulk, J. B., "Survivability of the Army/Sikorsky YUH-60A Helicopter," Preprint No. 1011, 32nd Annual National V/STOL Forum of the American Helicopter Society, Washington, D.C., May 1976.

[3] Chang, J. H., Stearman, R. O., "The Effects of Warhead-Induced Damage on the Aeroelastic Characteristics of Lifting Surfaces," Vol. 1 - Aeroelastic Effects, AFOSR-TR-80-1039, 1980.

[4] Westkaemper, J. C., Chandrasekharan, R. M., "The Effects of Warhead-Induced Damage on the Aeroelestic Characteristics of Lifting Surfaces," Vol. 2 - Aerodynamic Effects, AFOSR-TR-80-1040, 1980.

[5] Eastman, L., "UH-60A Dynamic Main Rotor Blade Ballistic Vulnerability Assessment," United Technologies SER-701981, 1993.

[6] "Investigation of Characteristics of Airflow within Aircraft Structures - Phase b(1)", Cornell Aeronautical Laboratory, Inc., Report No. V-699-D-17, April 1952.

[7] Reece, J. W., "Interpretation of the Drag Changes Measured in the Wind Tunnel Tests of a Holed Wing", Cornell Aeronautical Laboratory, Inc., Report No. G1-634-G-1, March 1952.

[8] Stearman, R. et. al., "The Influence of Ballistic Damage on the Aeroelastic Characteristics of Lifting Surfaces", AFOSR TR 80-0220, May 1979.

[9] Leishman, J. G., "Aerodynamic Characteristics of a Helicopter Rotor Airfoil as Affected by Simulated Ballistic Damage," USARL ARL-CR-66, 1993.

[10] Anderson, J. D., Jr., *Fundamentals of Aerodynamics*, McGraw-Hill, Inc., 1991.

[11] Abbott, I. H., Von Doenhoff, A. E., *Theory of Wing Sections*, Dover Publications, Inc., 1959.

[12] Hildebrand, F. B., *Introduction to Numerical Analysis*, Dover Publications, Inc., 1987.

[13] Prouty, R. W., *Helicopter Performance, Stability and Control*, PWS Engineering, Massachusetts, 1986.

[14] Hamming, R. W., *Numerical Methods for Scientists and Engineers*, Dover Publications, Inc., 1986.

[15] Johnson, W., *Helicopter Theory*, Dover Publications, Inc., 1994.

[16] Leishman, J. G., *Helicopter Aerodynamics*, Classroom Notes, University of Maryland, January 1994.

[17] Thwaites, B., *Incompressible Aerodynamics*, Dover Publications, Inc., 1987.

[18] Carr, L. W., McAlister, K. W., McCroskey, W. J., Pucci, S. L., "An

Experimental Study of Dynamic Stall on Advanced Airfoil Sections," Vol. 1 -

Summary of the Experiment, NASA TM 84245, 1982.
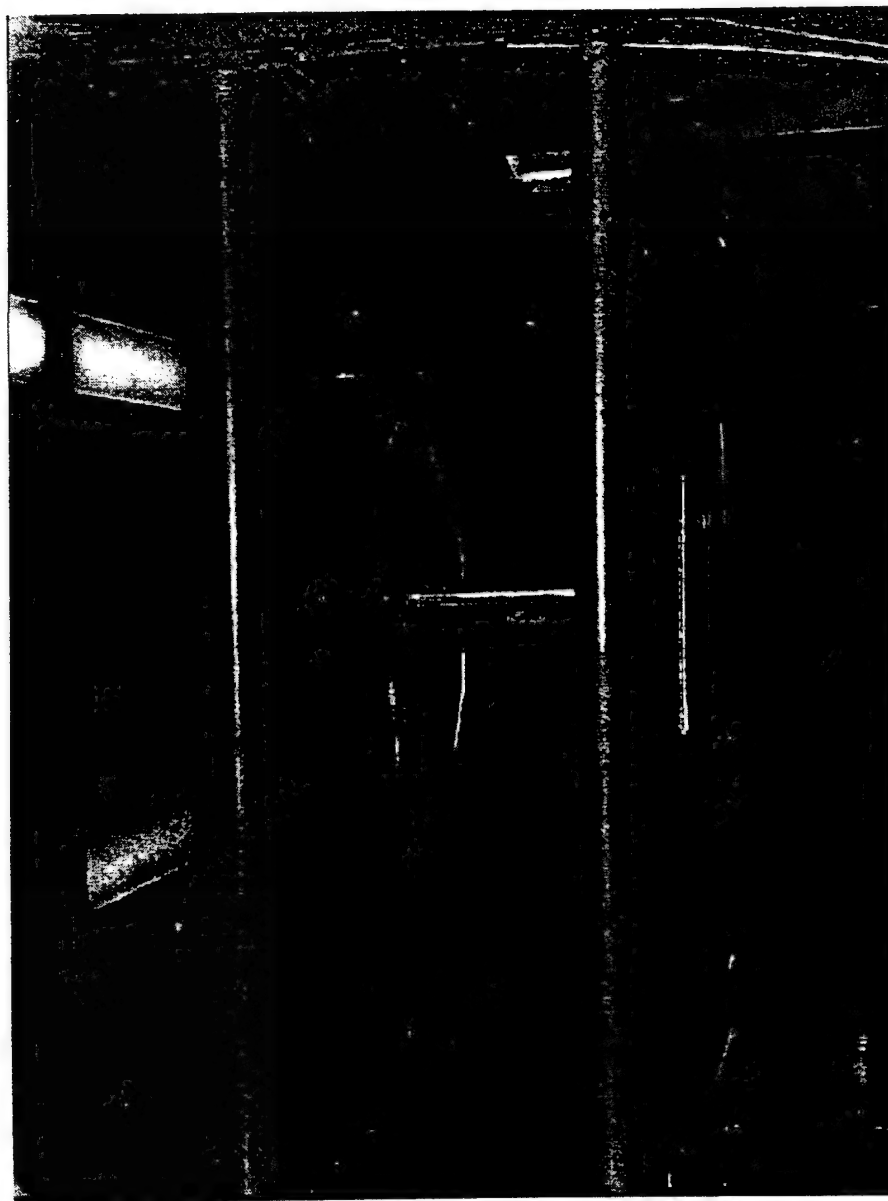
Figure 1: 2-D Insert in Test Section of GLMWT with Blade Section Installed (view from front, looking downstream)
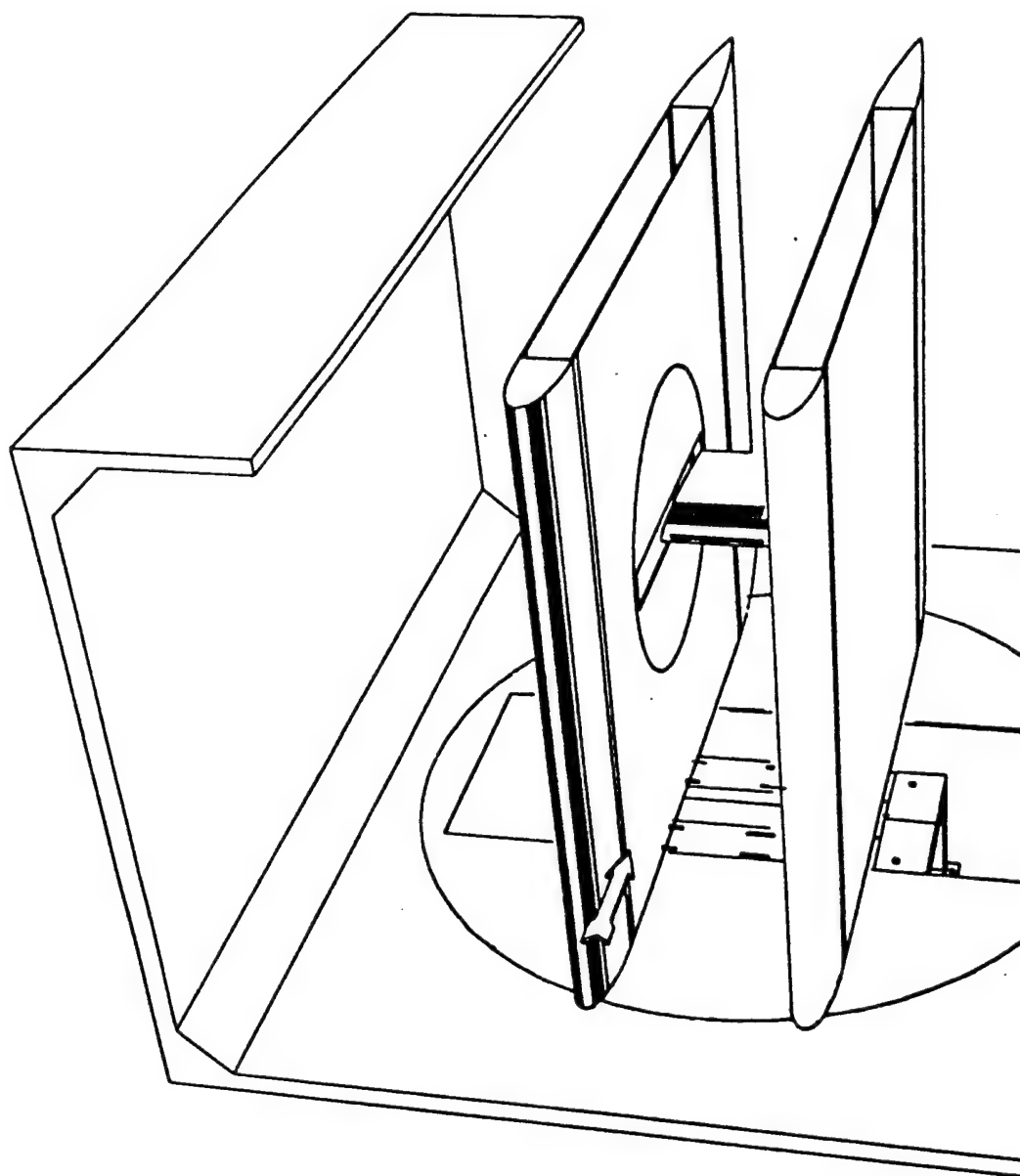
Figure 2: Front Cut-Away View of 2-D Insert with Force Balance Exposed in Floor

81
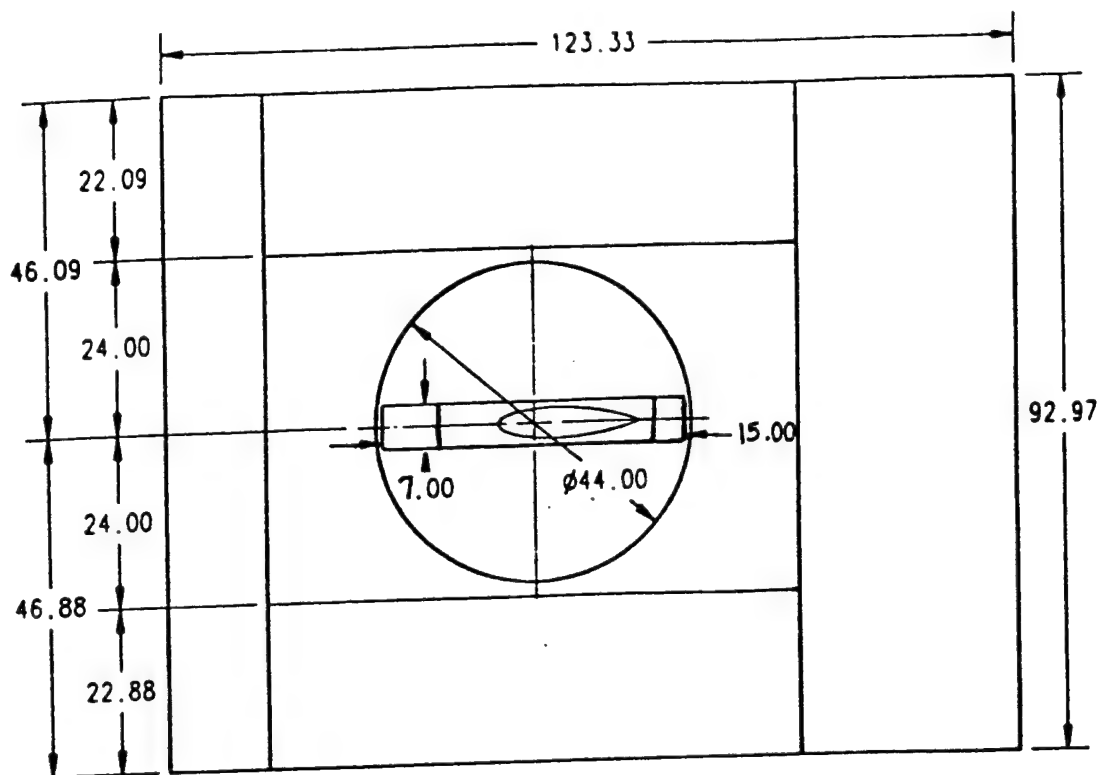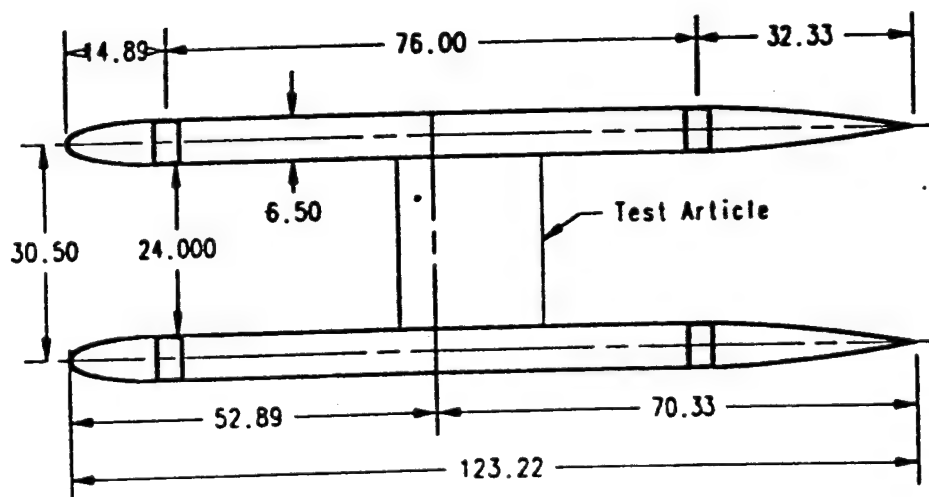
Side View

Two Dimensional Test Section Insert
Top View

Figure 3: Dimensional Top and Side View of 2-D Insert

82
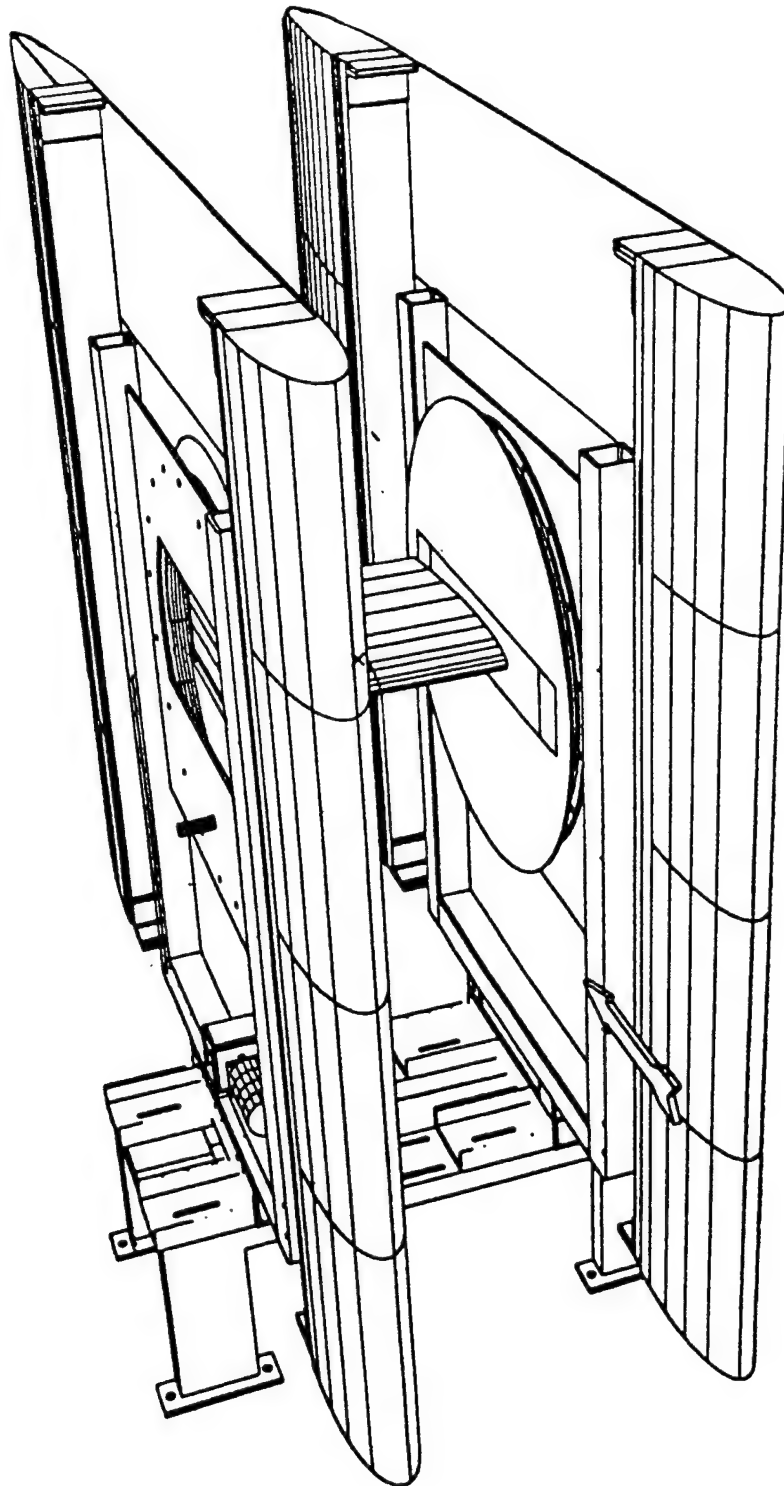
Figure 4: Front Cut-away View of 2-D Insert with Main Support Structure Base
Attached to Force Balance

Figure 5: Front View of Scarf Vortex Formed at Blade Section / 2-D Insert Junction
(note laminar separation bubble formed on the leading-edge of the blade section)
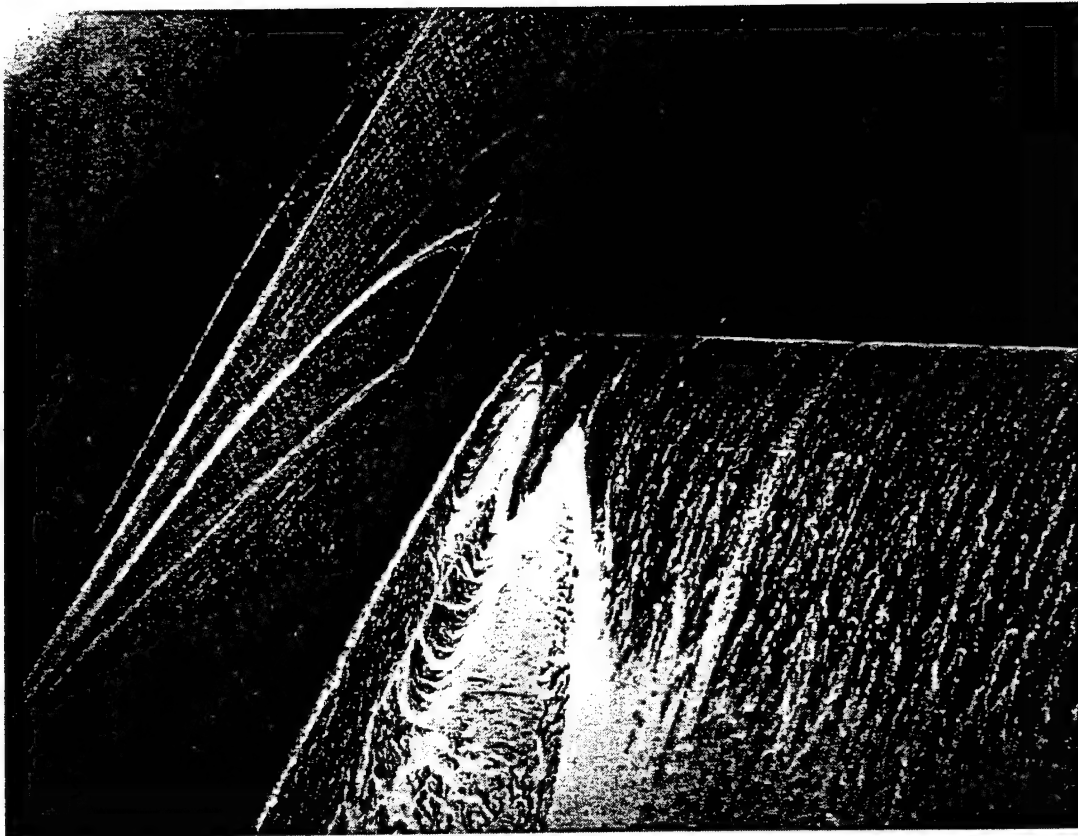
Figure 6: Top View of Scarf Vortex Formed at Blade Section / 2-D Insert Junction
(looking upstream)
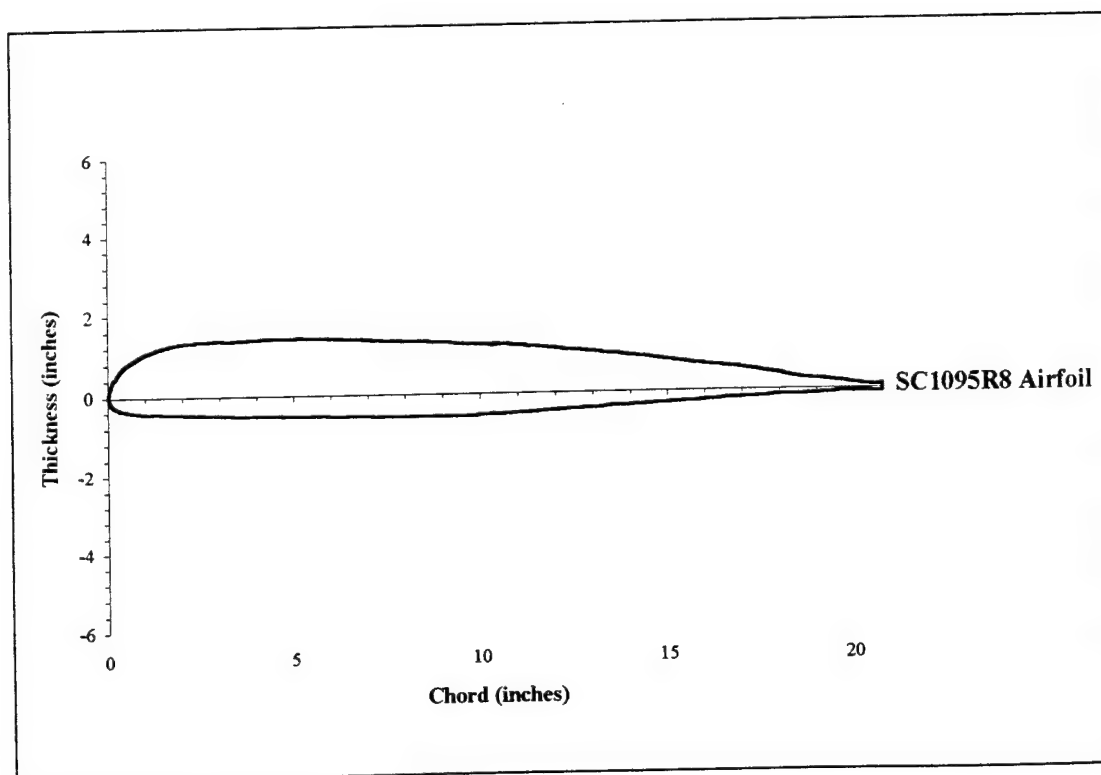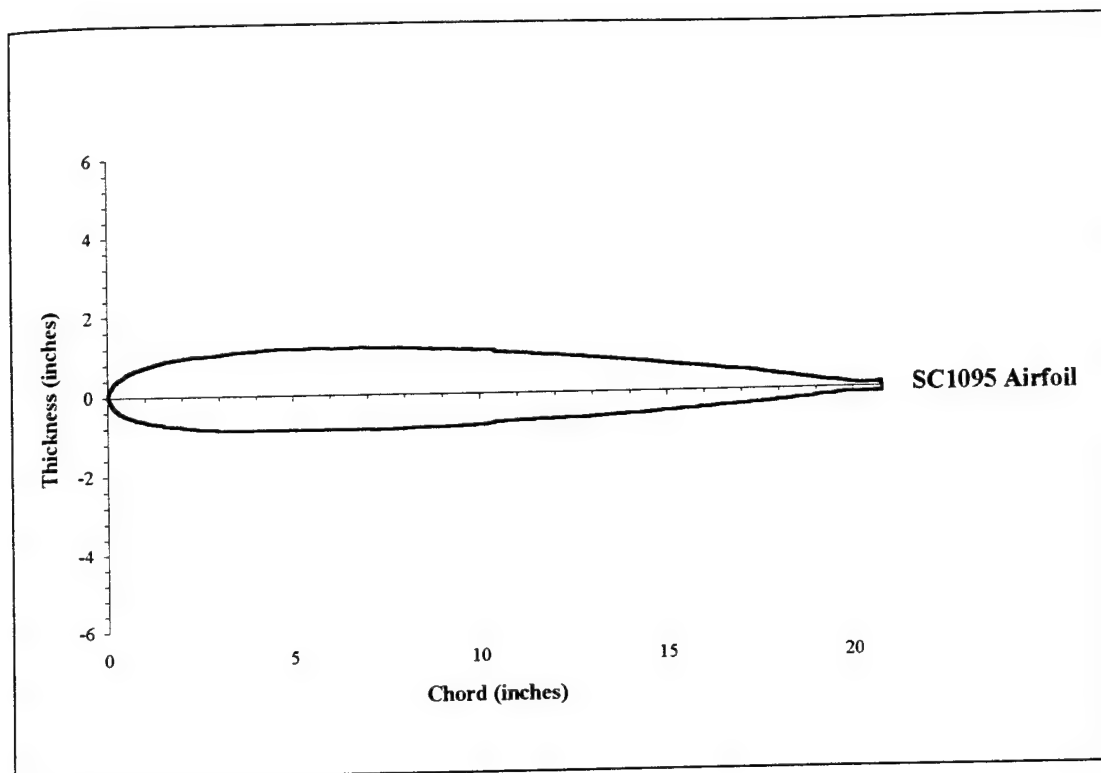
Figure 7: SC1095 and SC1095R8 Airfoil Profiles (Ref. 18)

86
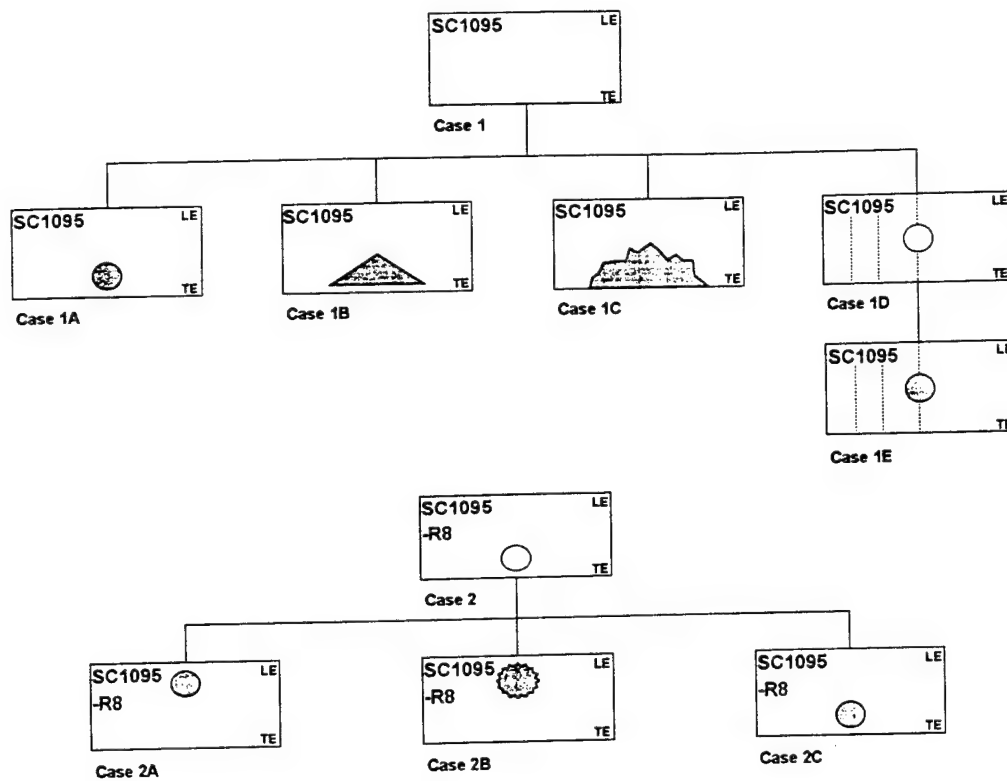
Figure 8: Blade Section Configurations

SC1095

Leading Edge

Trailing Edge

20.77 in

12.00 in

24.00 in
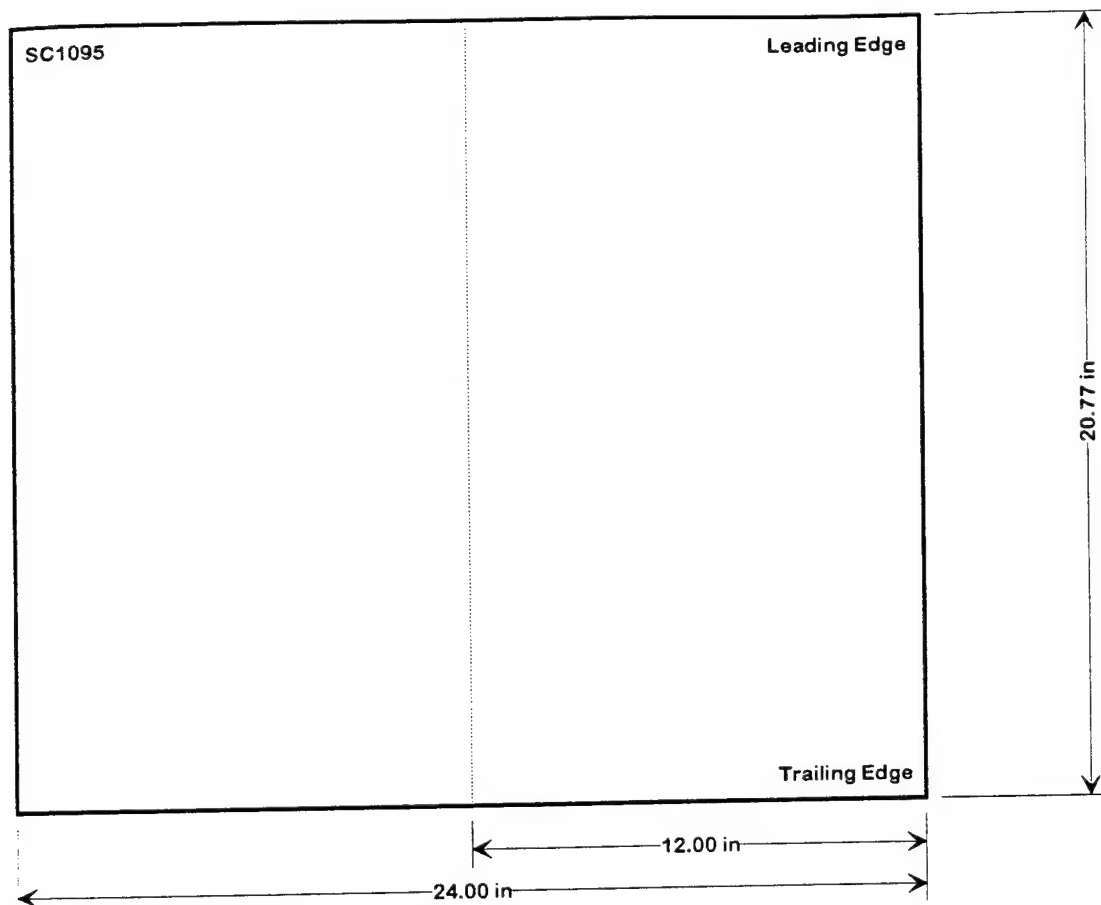
Figure 9: Case 1 Blade Configuration (Undamaged Baseline)

88
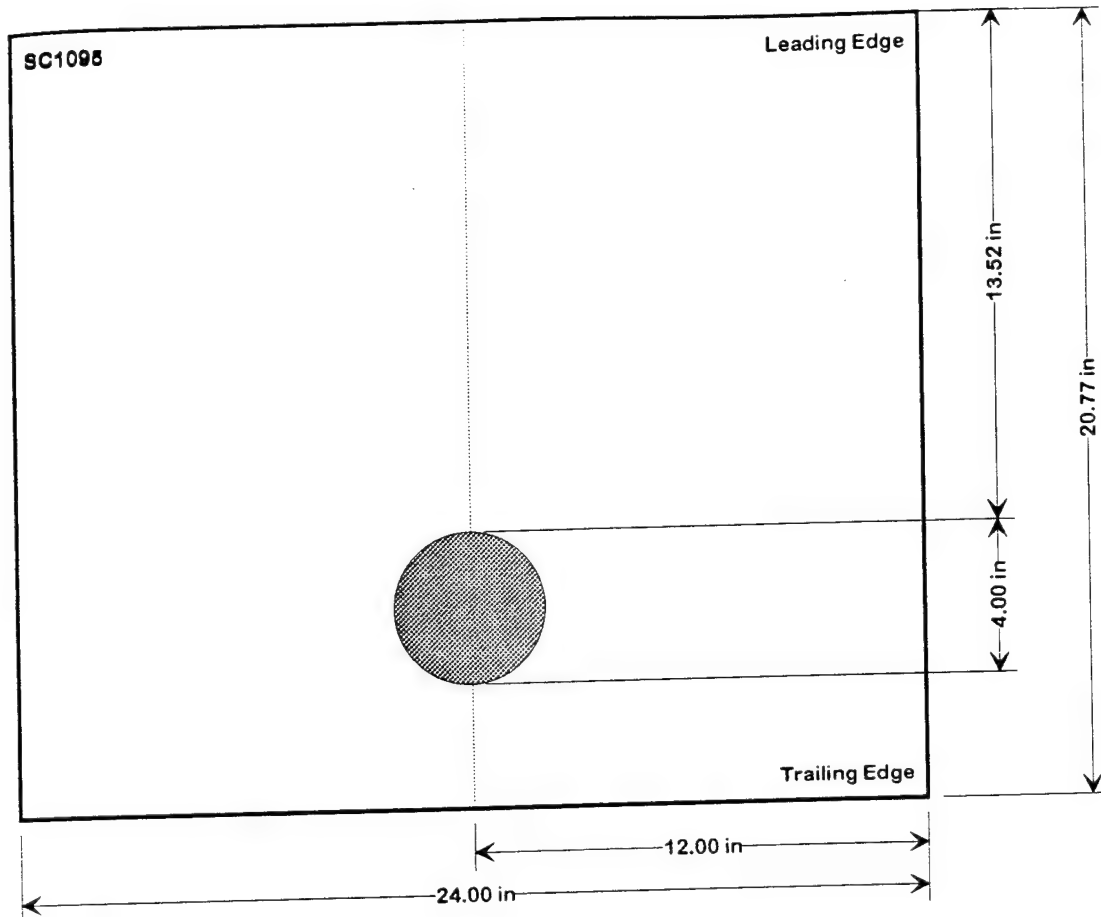
Figure 10: Case 1A Blade Configuration
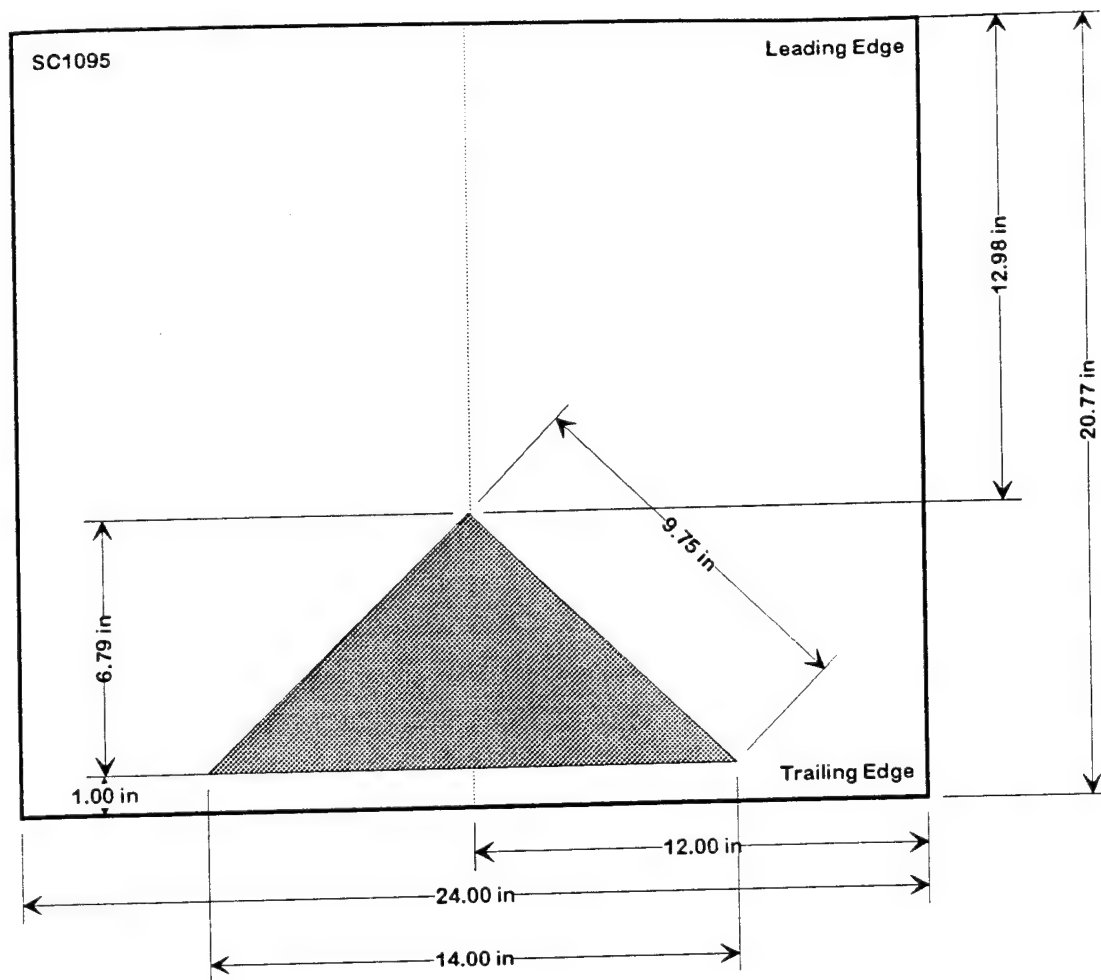
Figure 11: Case 1B Blade Configuration
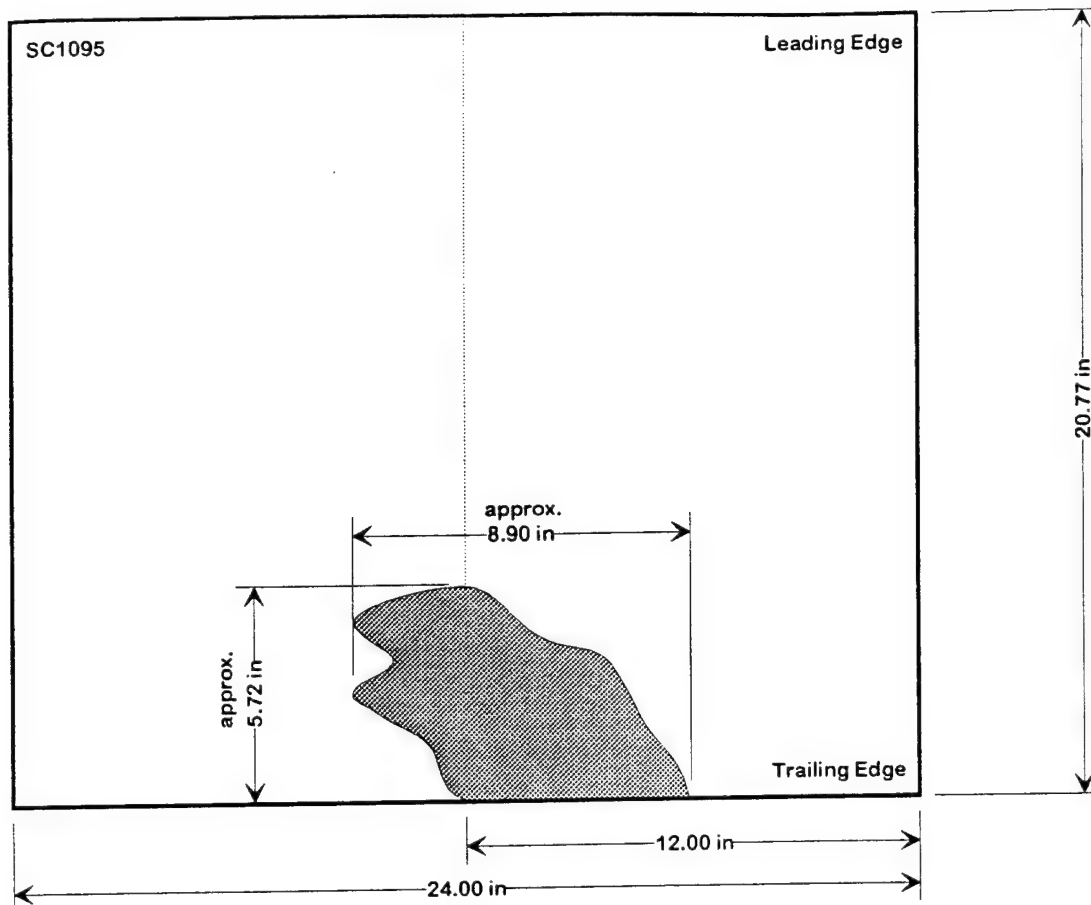
Figure 12: Case 1C Blade Configuration (Actual Ballistic Damage)
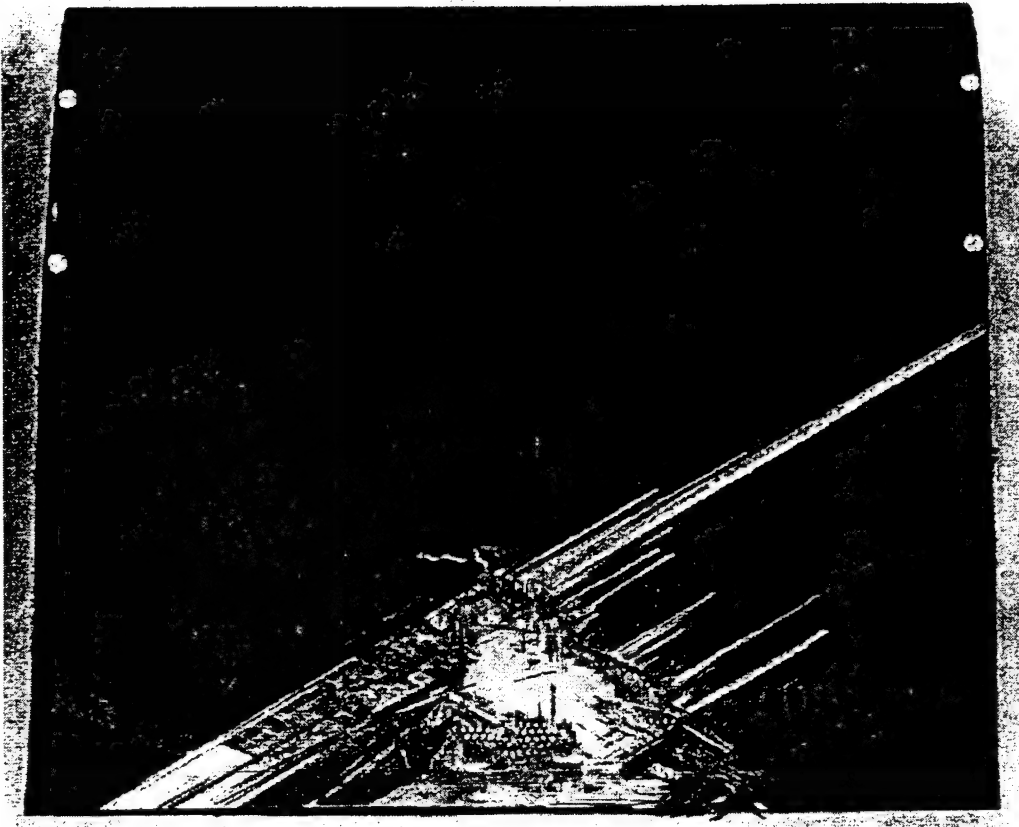
Figure 13a: Case 1C Blade Configuration (Actual Ballistic Damage -- Top View)
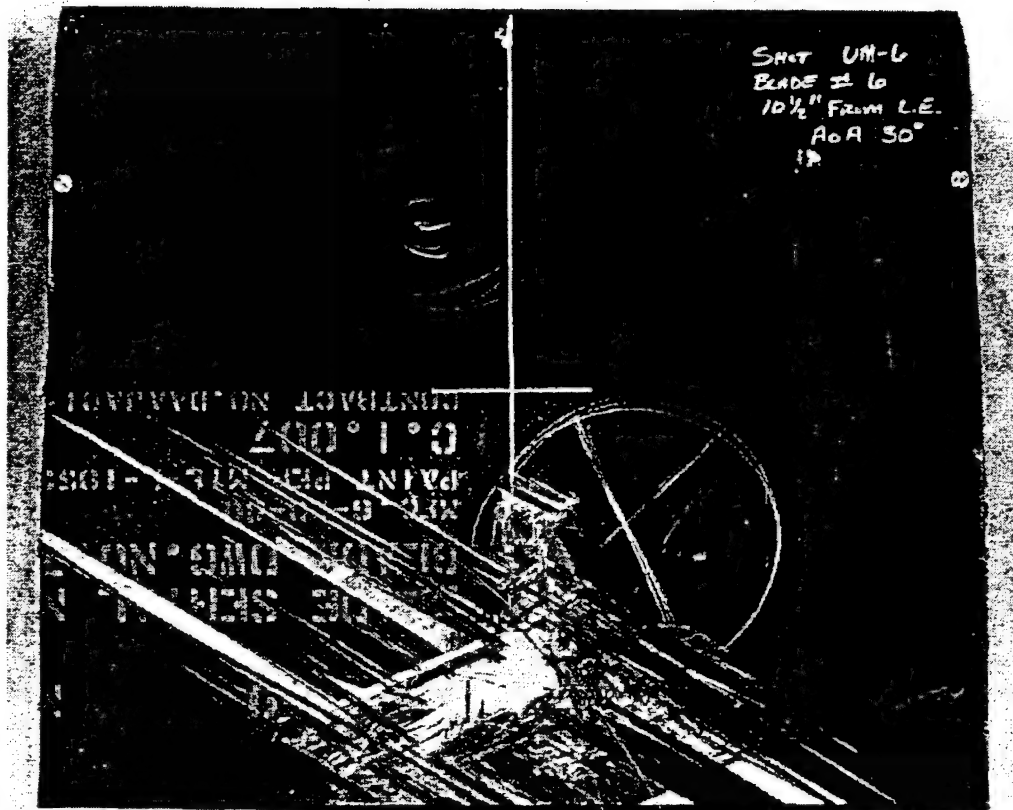
Figure 13b: Case 1C Blade Configuration (Actual Ballistic Damage -- Bottom View)
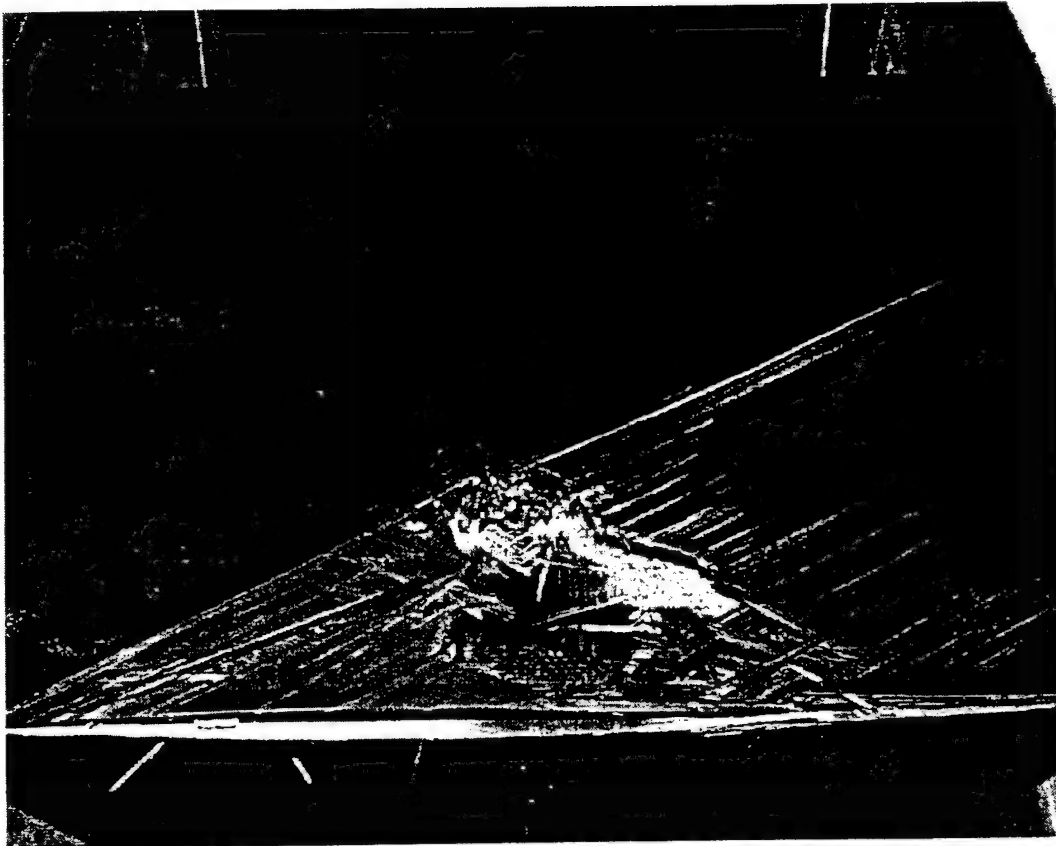
Figure 14: Case 1C Blade Configuration (Actual Ballistic Damage) Installed in 2-D
Insert (looking forward)
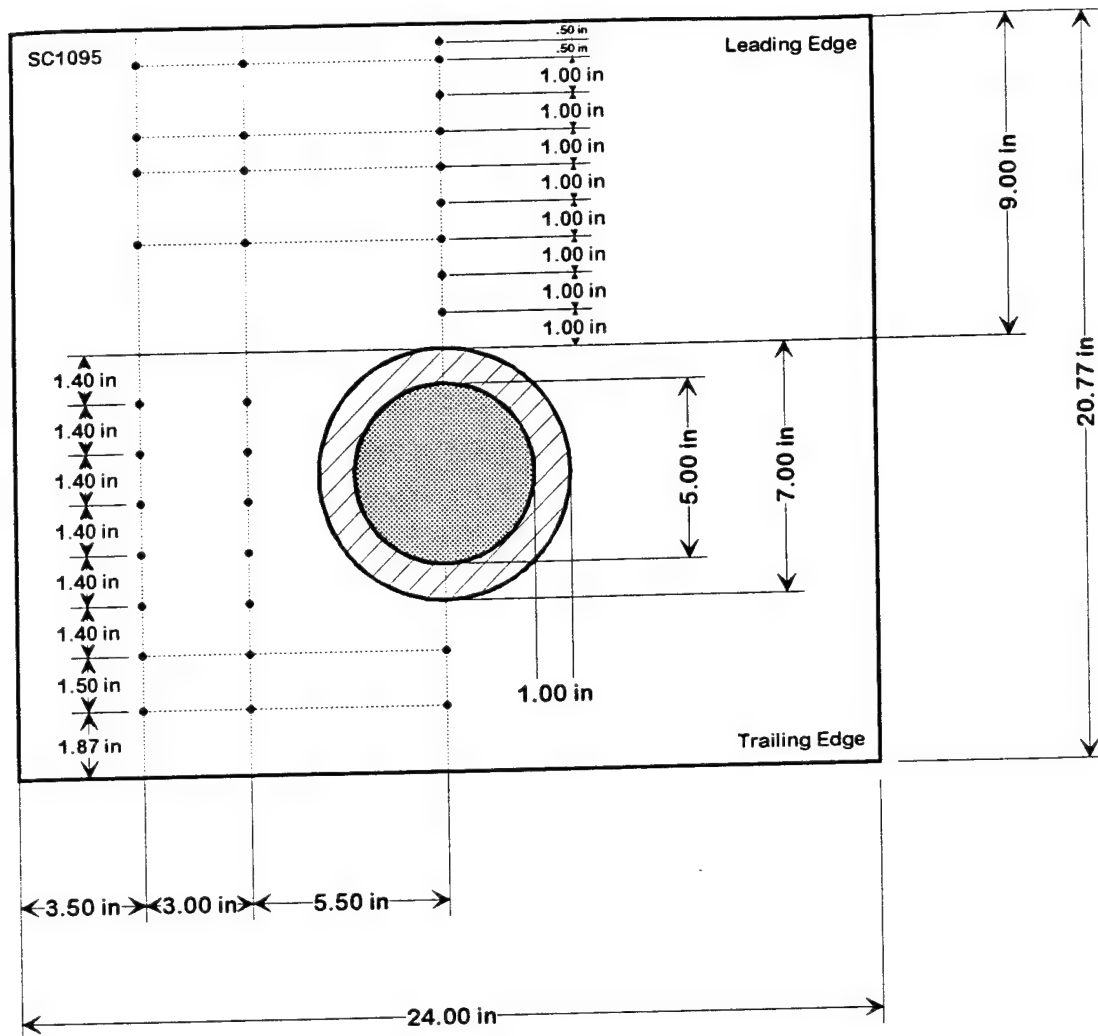
Figure 15a: Case 1E Blade Configuration (Top View)
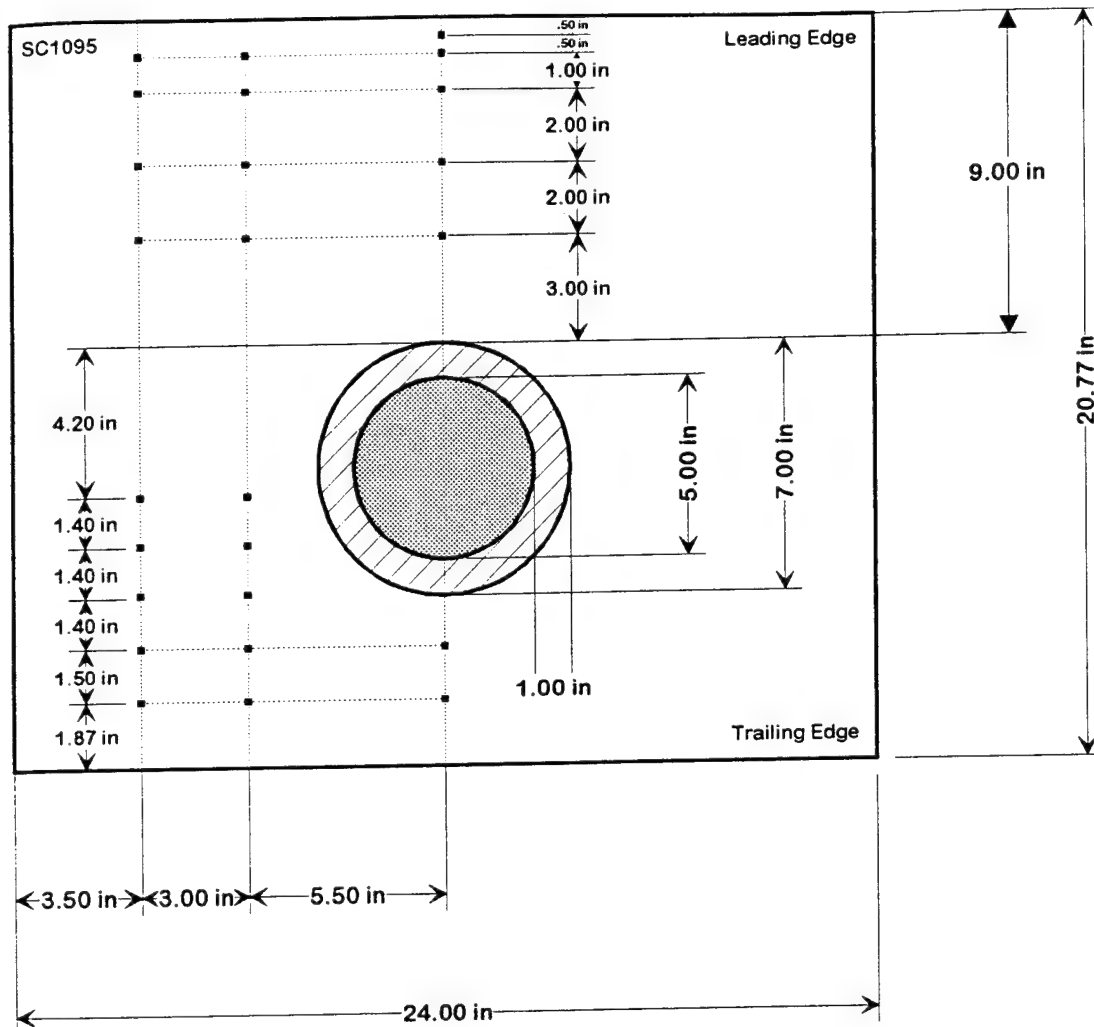
Figure 15b: Case 1E Blade Configuration (Bottom View)
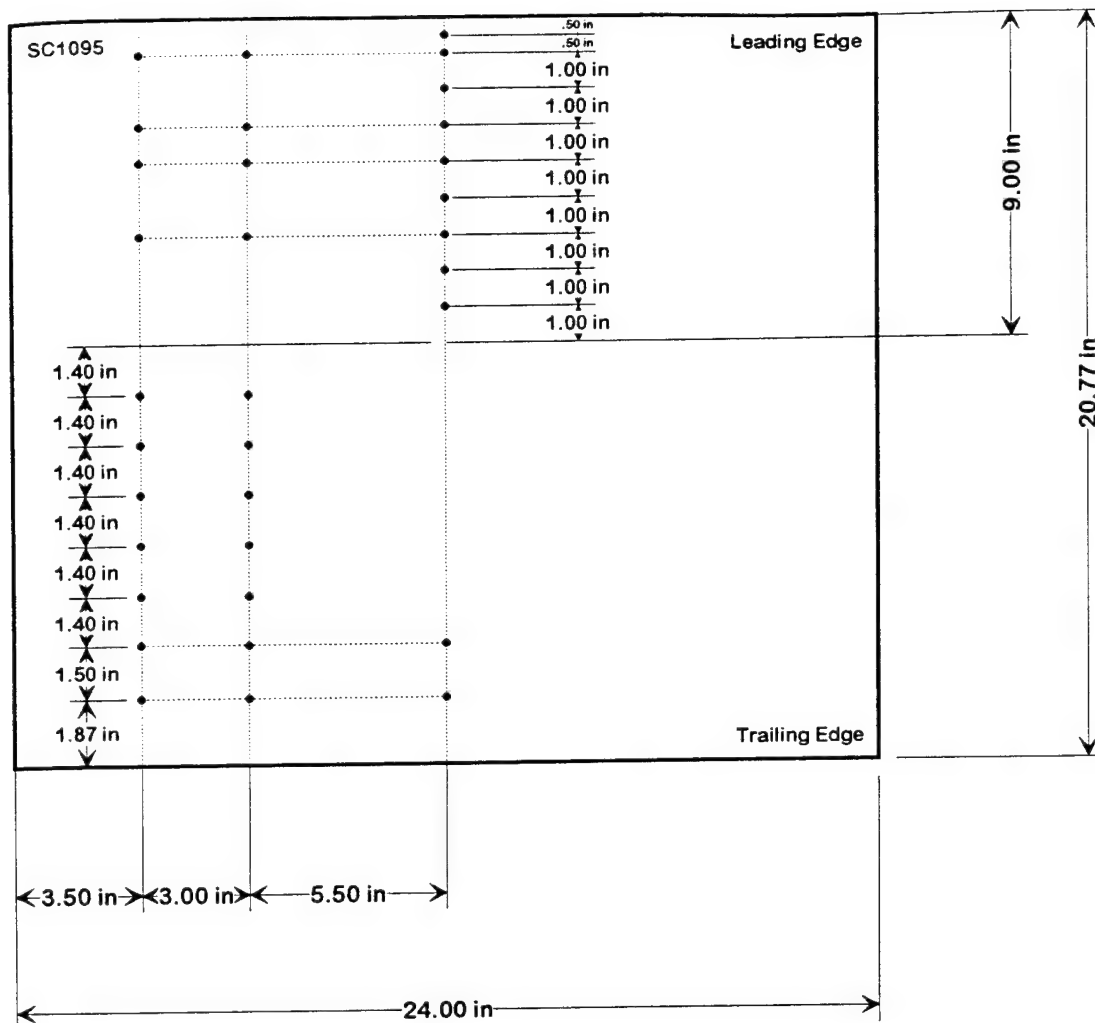
Figure 16a: Case 1D Blade Configuration (Top View)
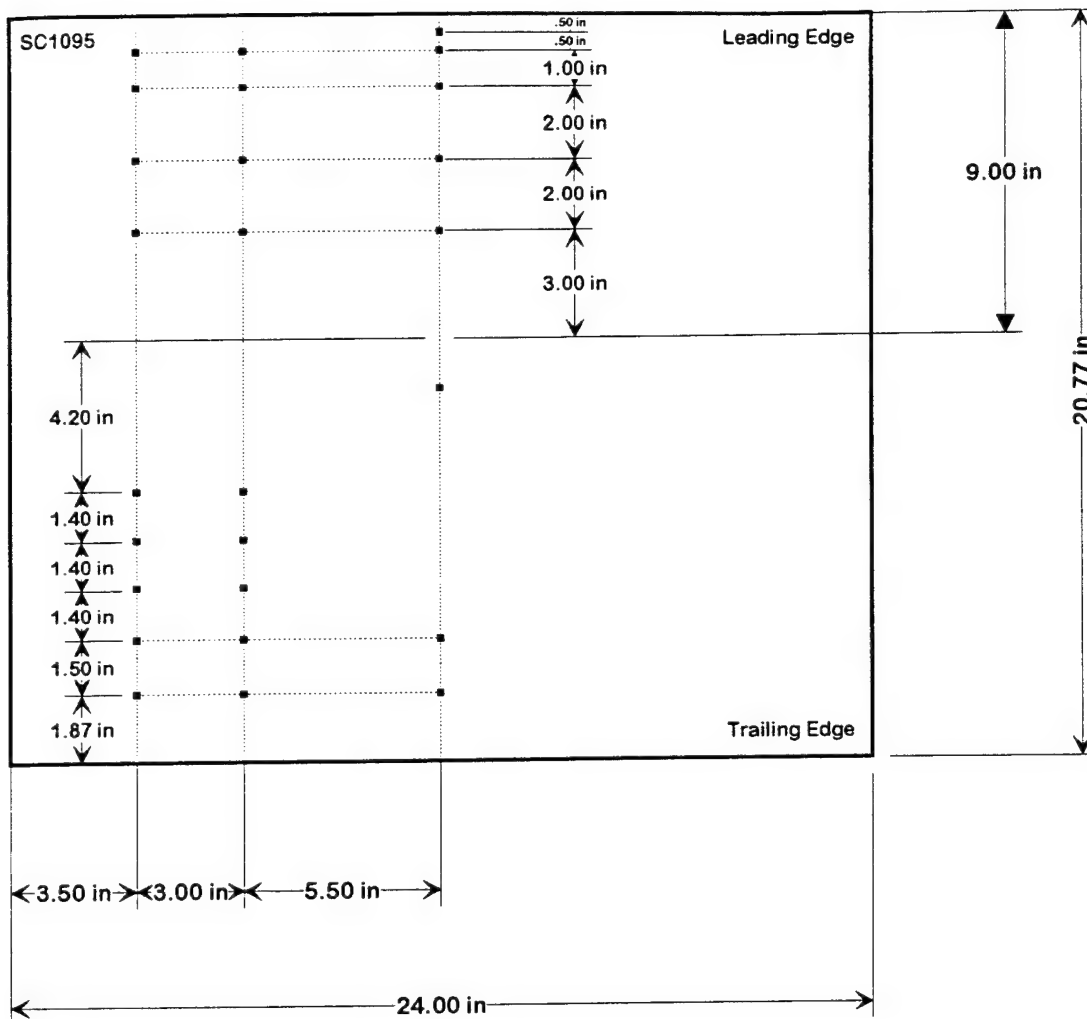
Figure 16b: Case 1D Blade Configuration (Bottom View)
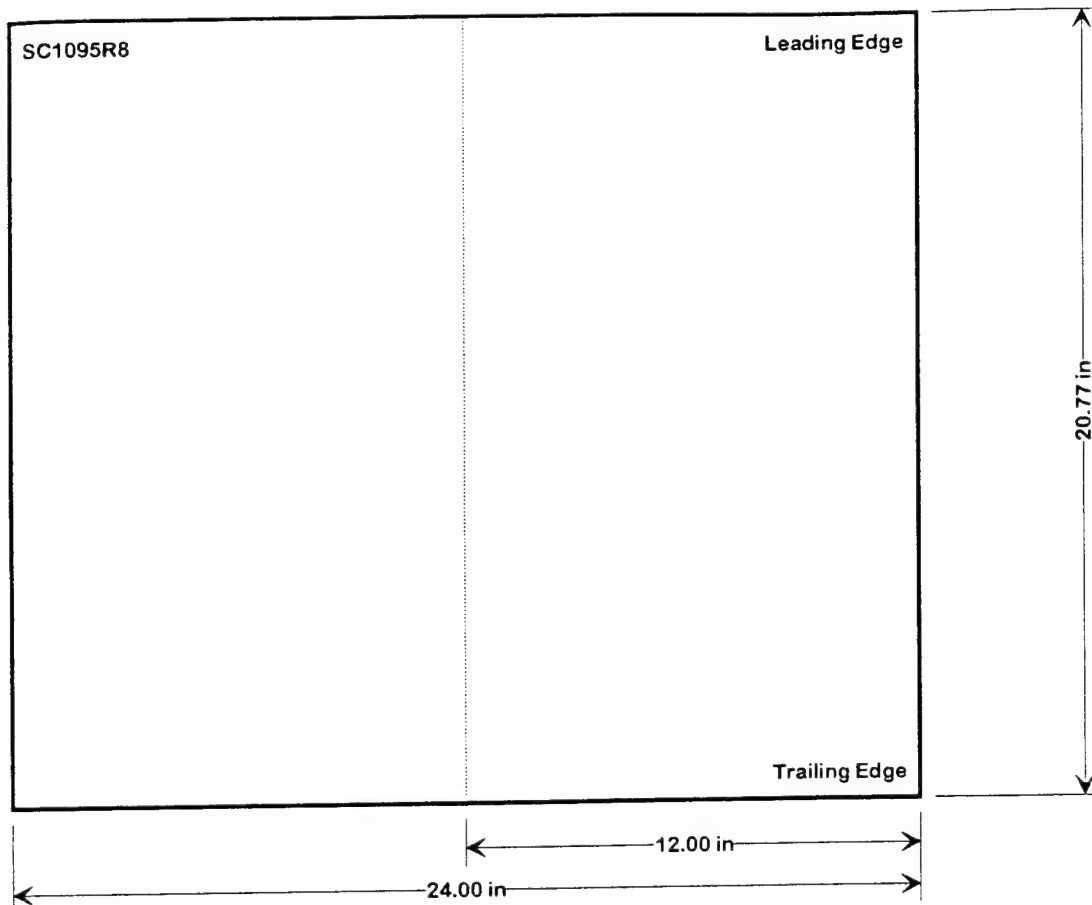
Figure 17: Case 2 Blade Configuration (Undamaged Baseline)

SC1095R8   Leading Edge

3.30 in

4.00 in

20.77 in

Trailing Edge

12.00 in

24.00 in
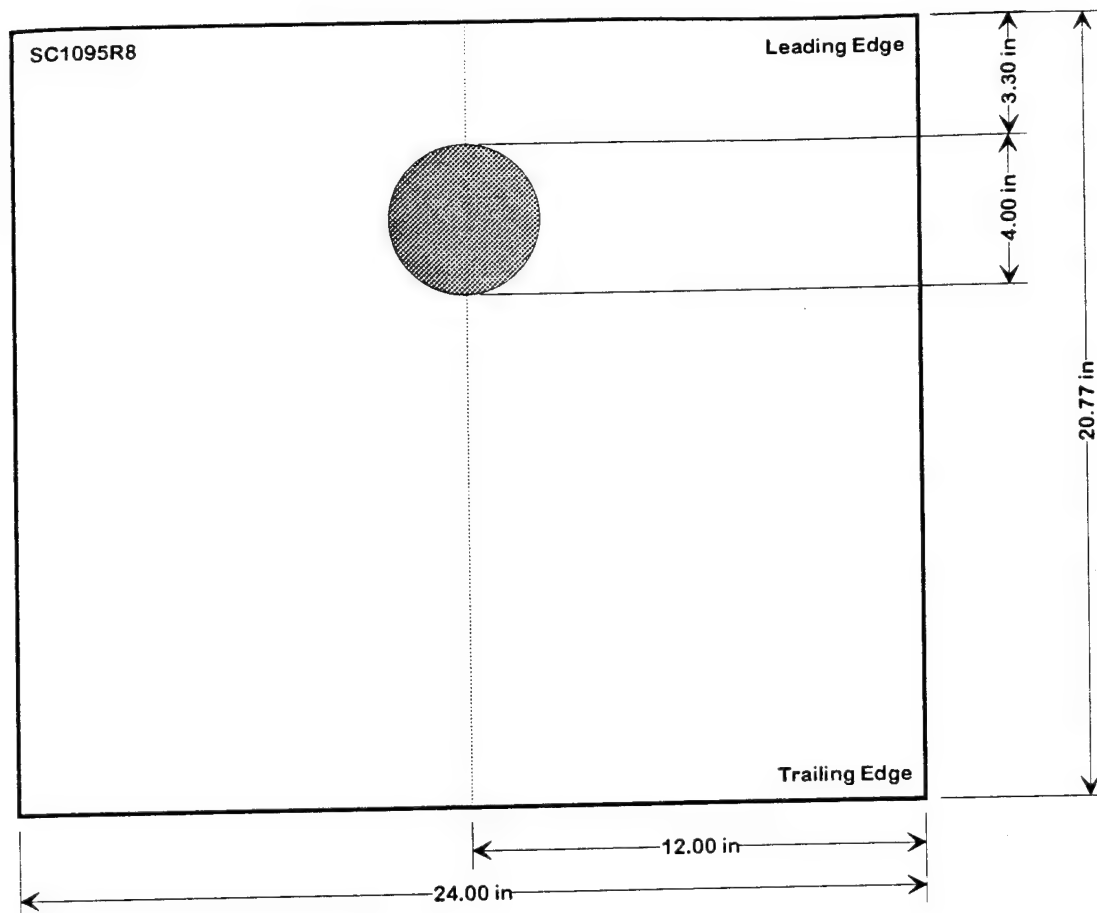
Figure 18: Case 2A and Case 2B Blade Configuration
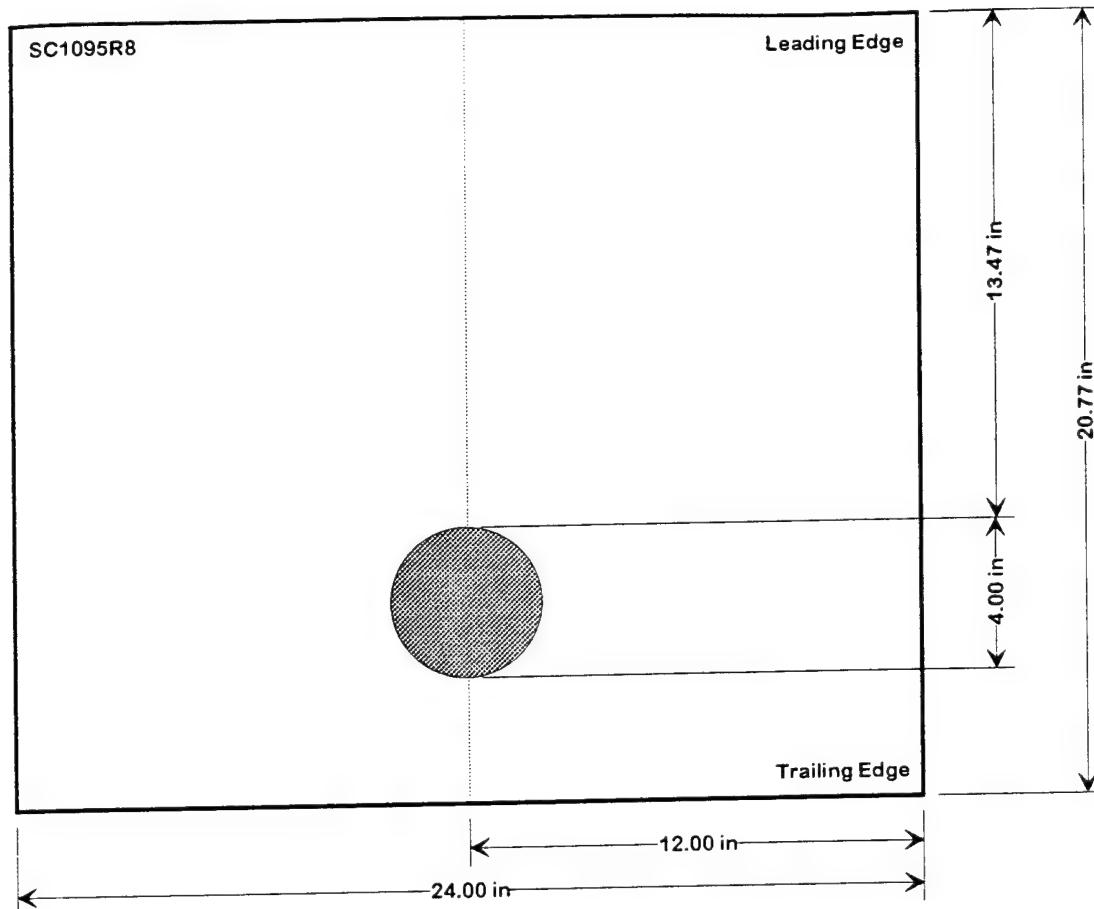
Figure 19: Case 2C Blade Configuration

Comparison #   Cases Compared
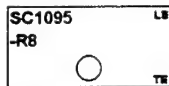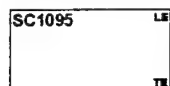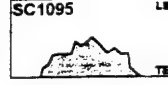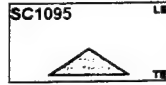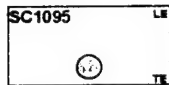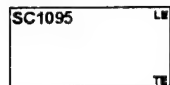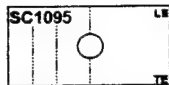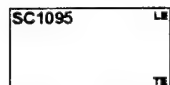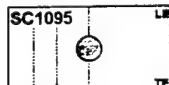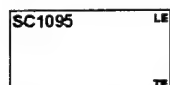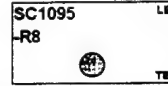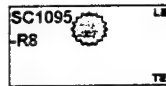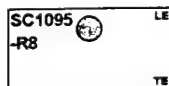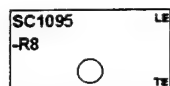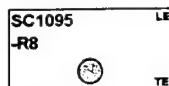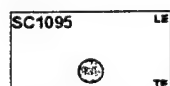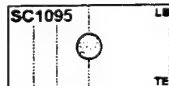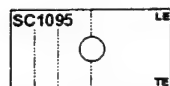
Figure 20: Case Comparison Summary

102
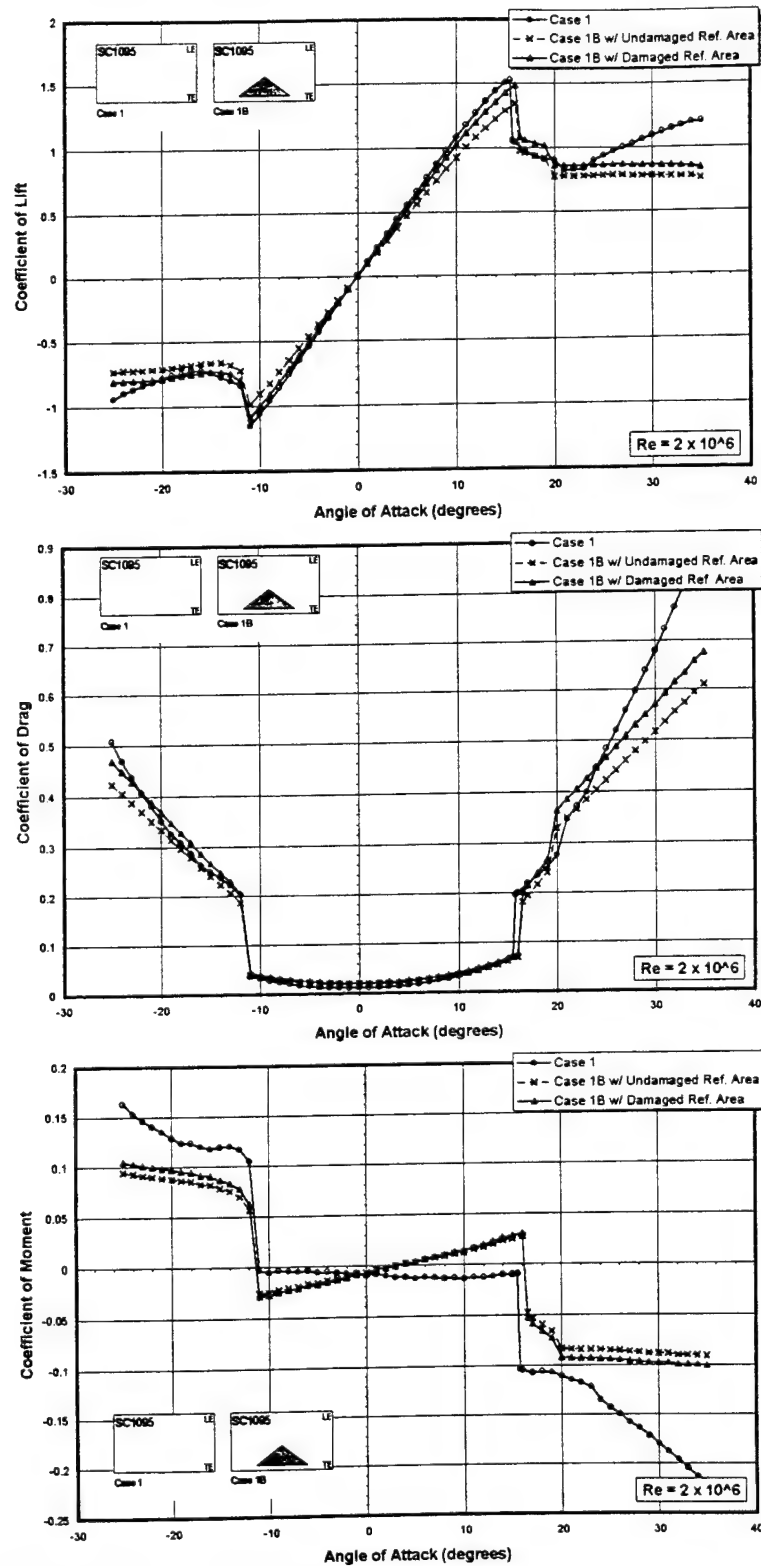
Figure 21: Aerodynamic Characteristics of Case 1 and Case 1B Blade Sections Non-Dimensionalized by Undamaged and Damaged Blade Section Areas at Re = 2 x 10^6
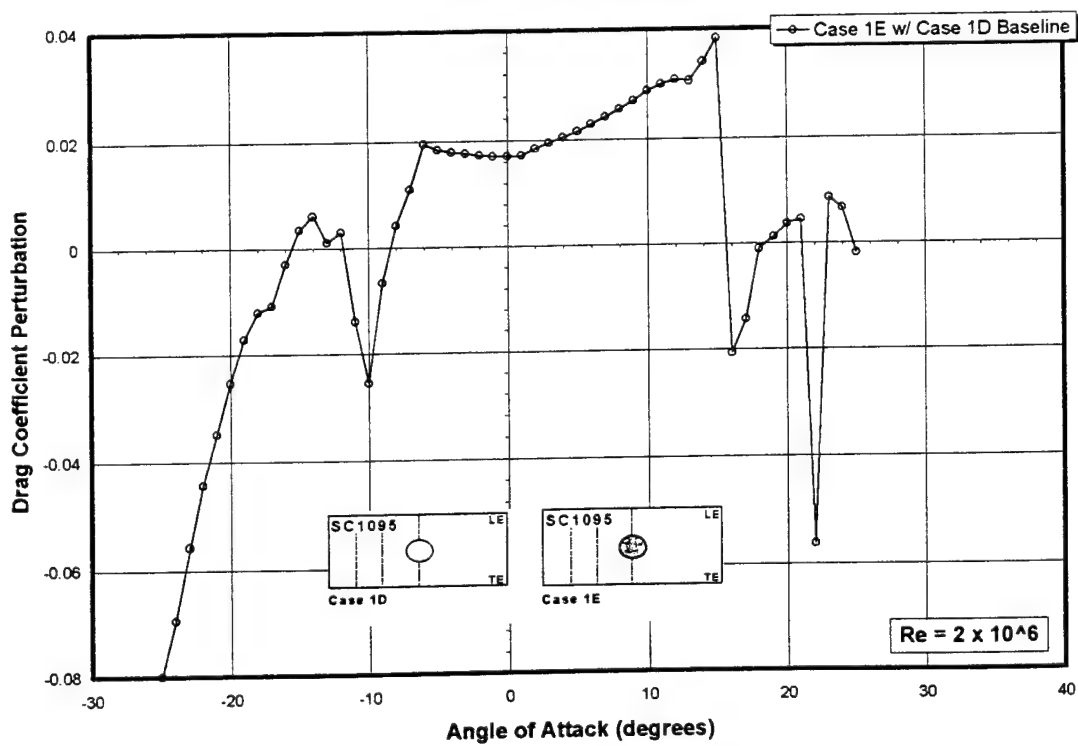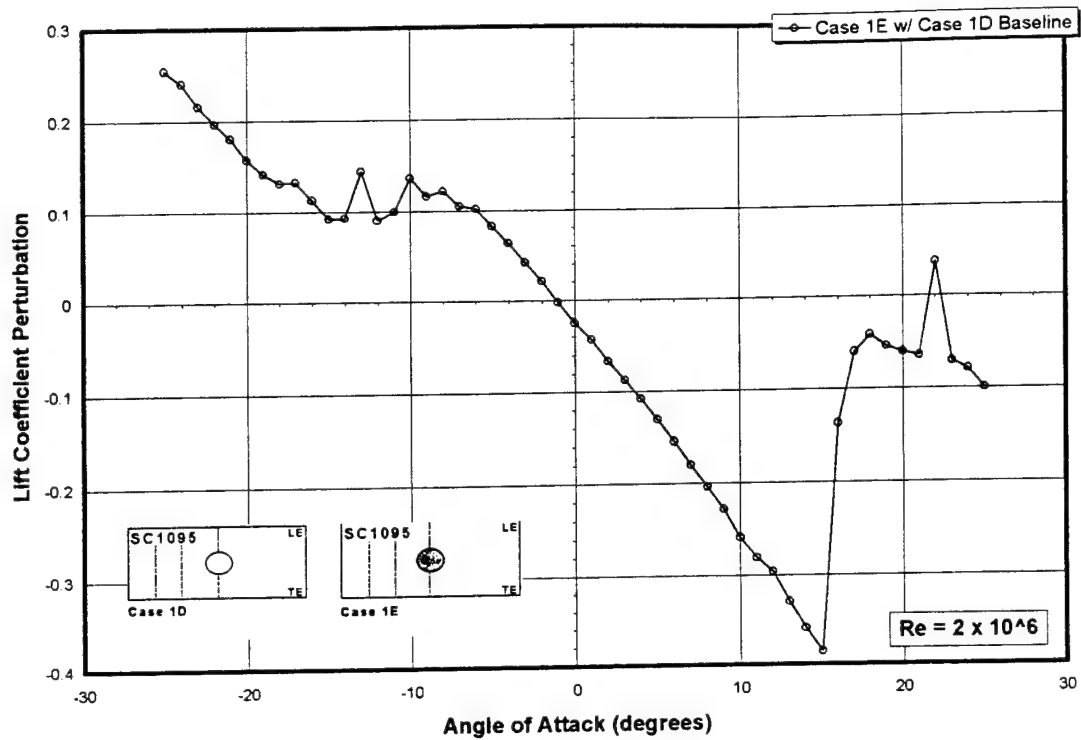
Figure 22a: Lift and Drag Perturbations of Case 1E from Baseline (Case 1D) at Re = 2×10^6
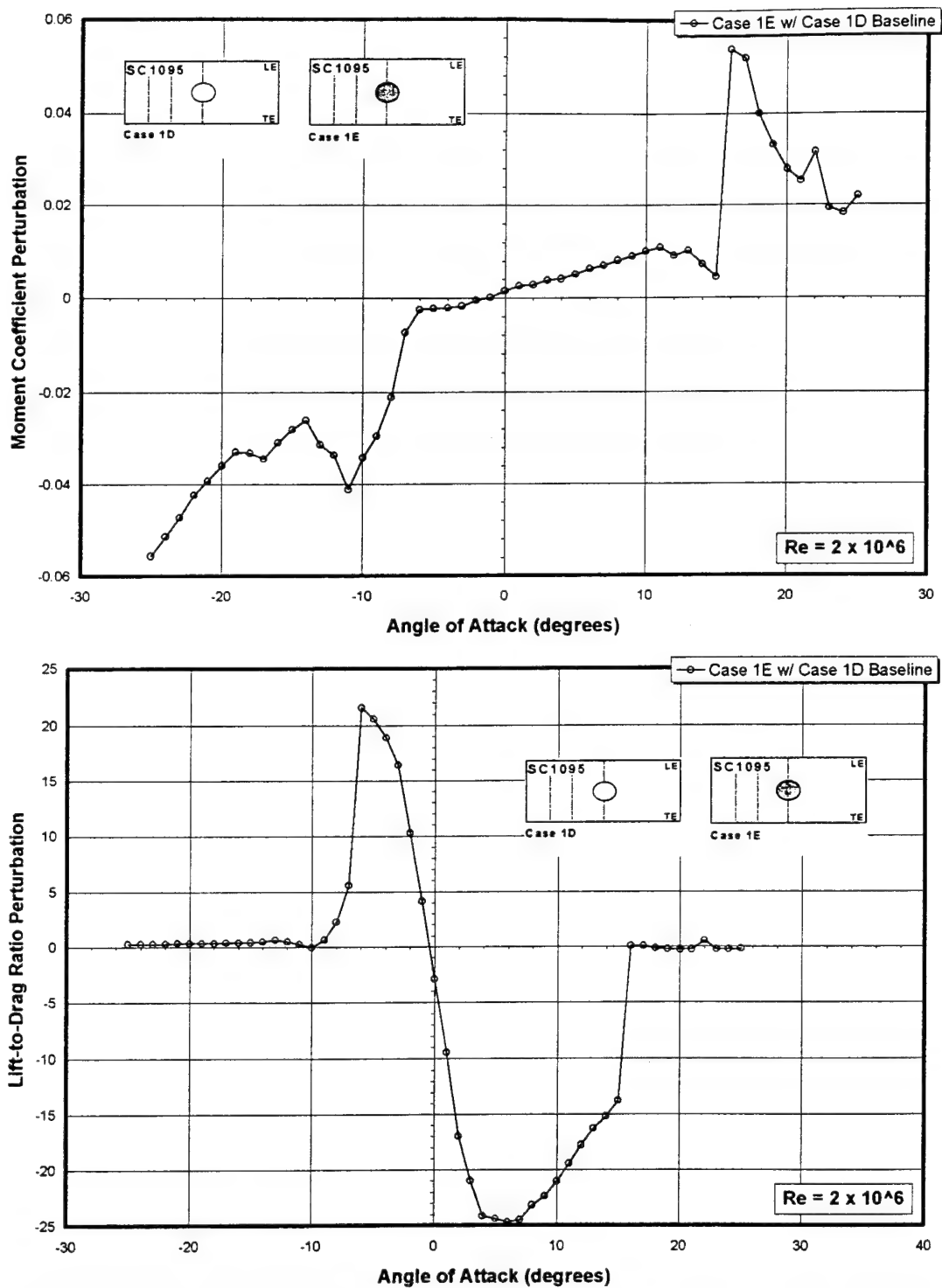
Figure 22b: Moment and Lift-to-Drag Ratio Perturbations of Case 1E from Baseline (Case 1D) at Re = 2×10^6
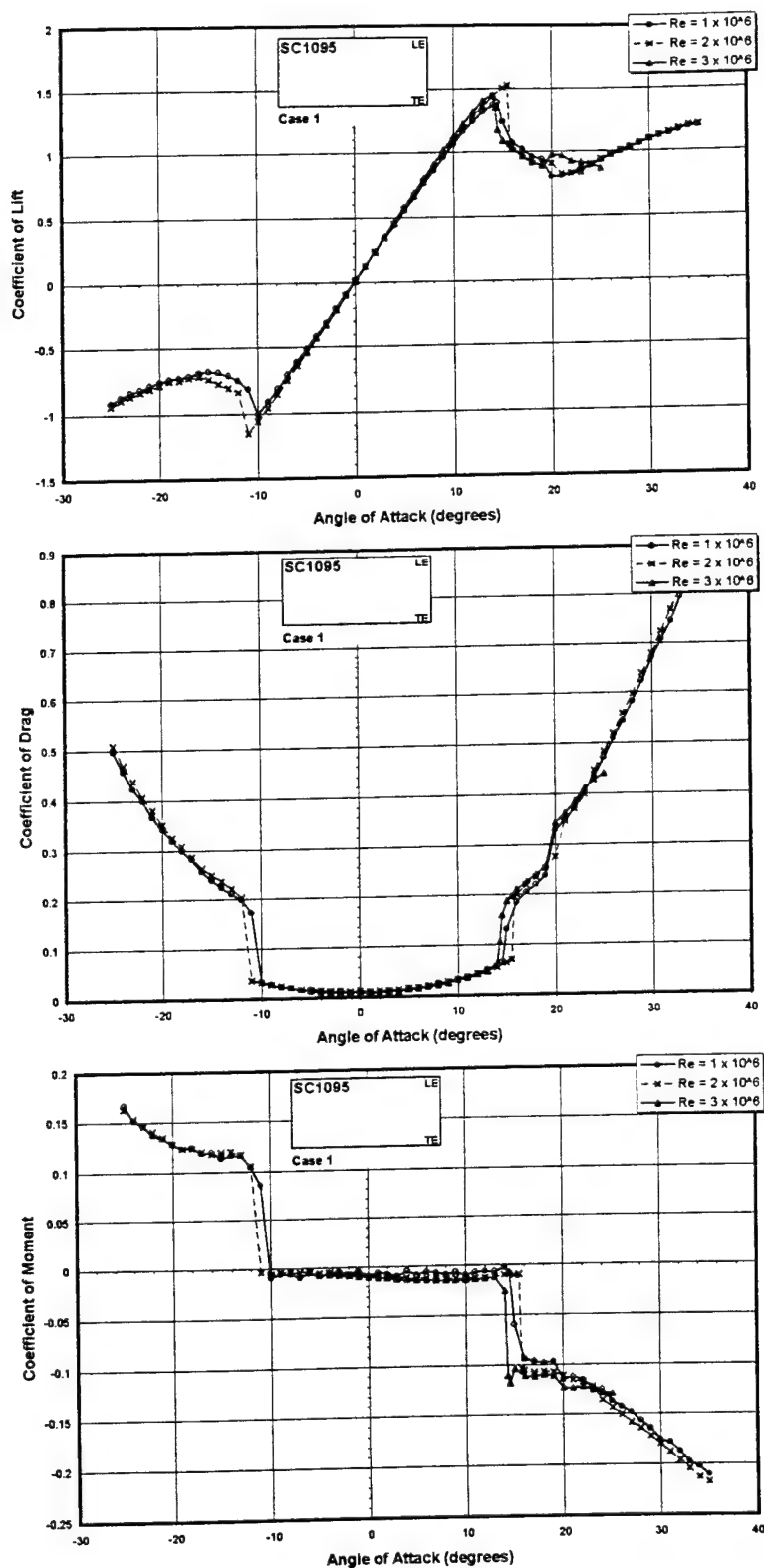
Figure 23: Aerodynamic Characteristics of Case 1 Blade Section Measured at
Reynolds Numbers of 1×10^6, 2×10^6, and 3×10^6
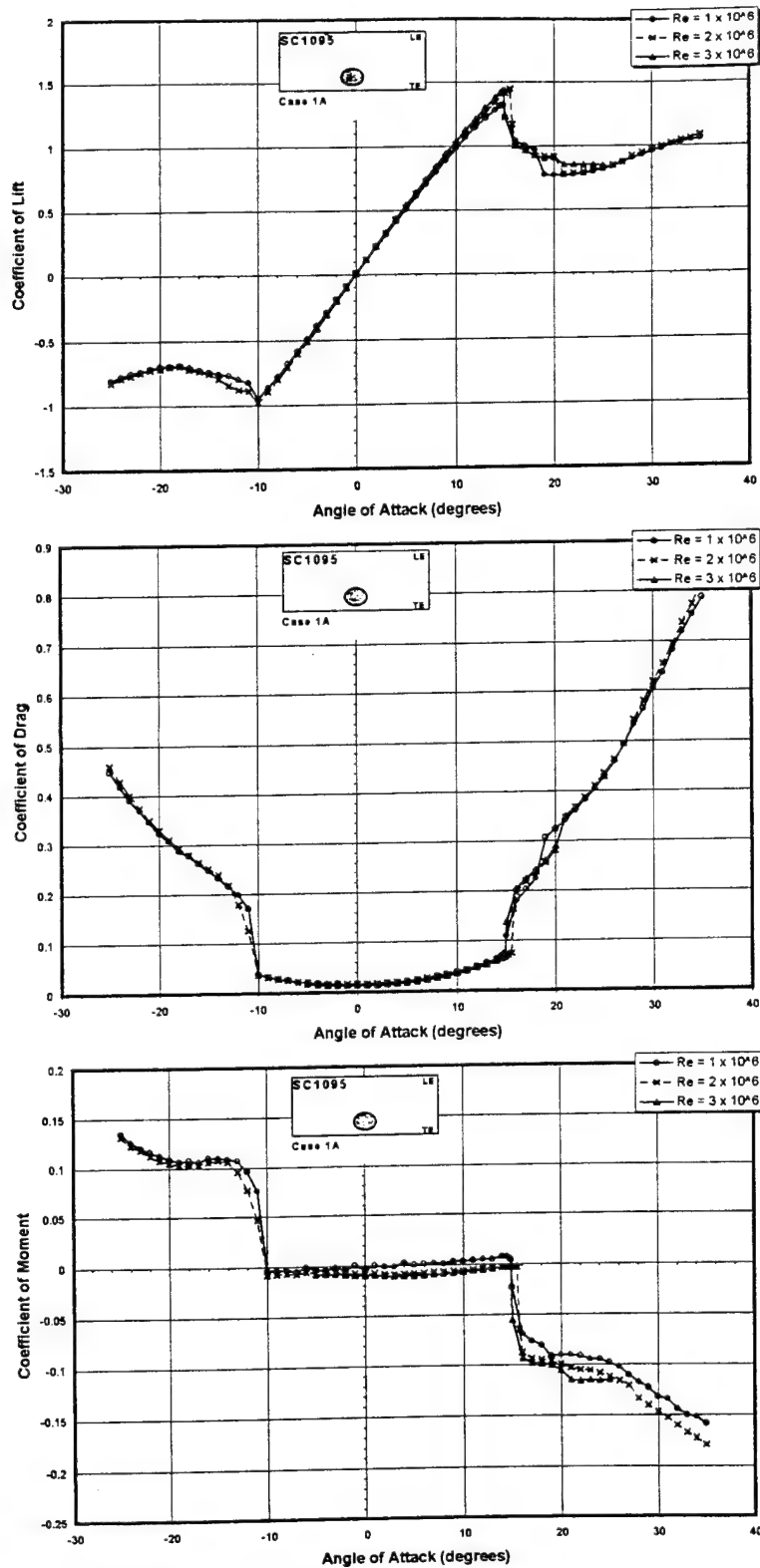
Figure 24: Aerodynamic Characteristics of Case 1A Blade Section Measured at
Reynolds Numbers of 1×10^6, 2×10^6, and 3×10^6

107
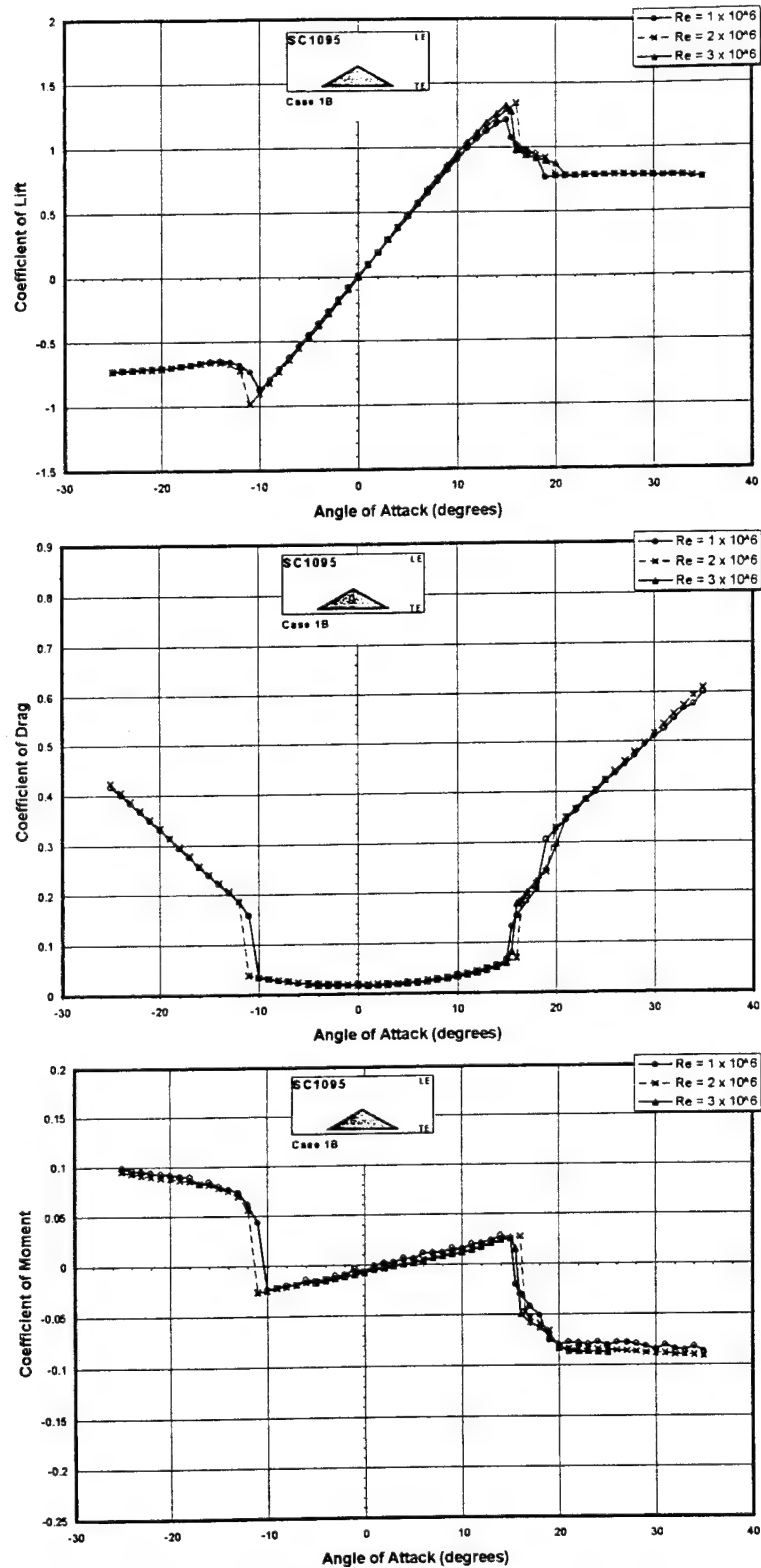
Figure 25: Aerodynamic Characteristics of Case 1B Blade Section Measured at Reynolds Numbers of 1 x 10⁶, 2 x 10⁶, and 3 x 10⁶
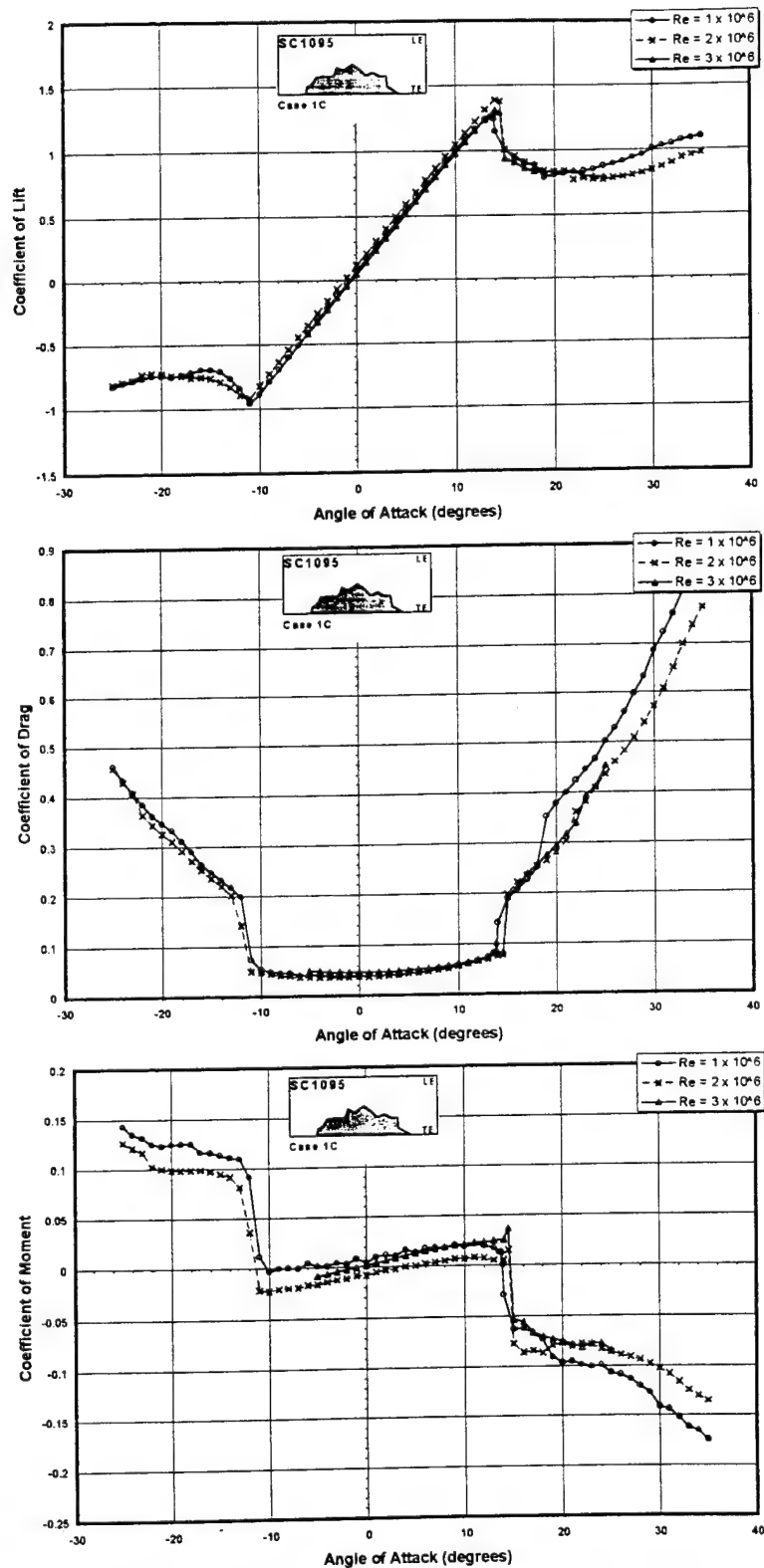
Figure 26: Aerodynamic Characteristics of Case 1C Blade Section Measured at
Reynolds Numbers of 1×10^6, 2×10^6, and 3×10^6
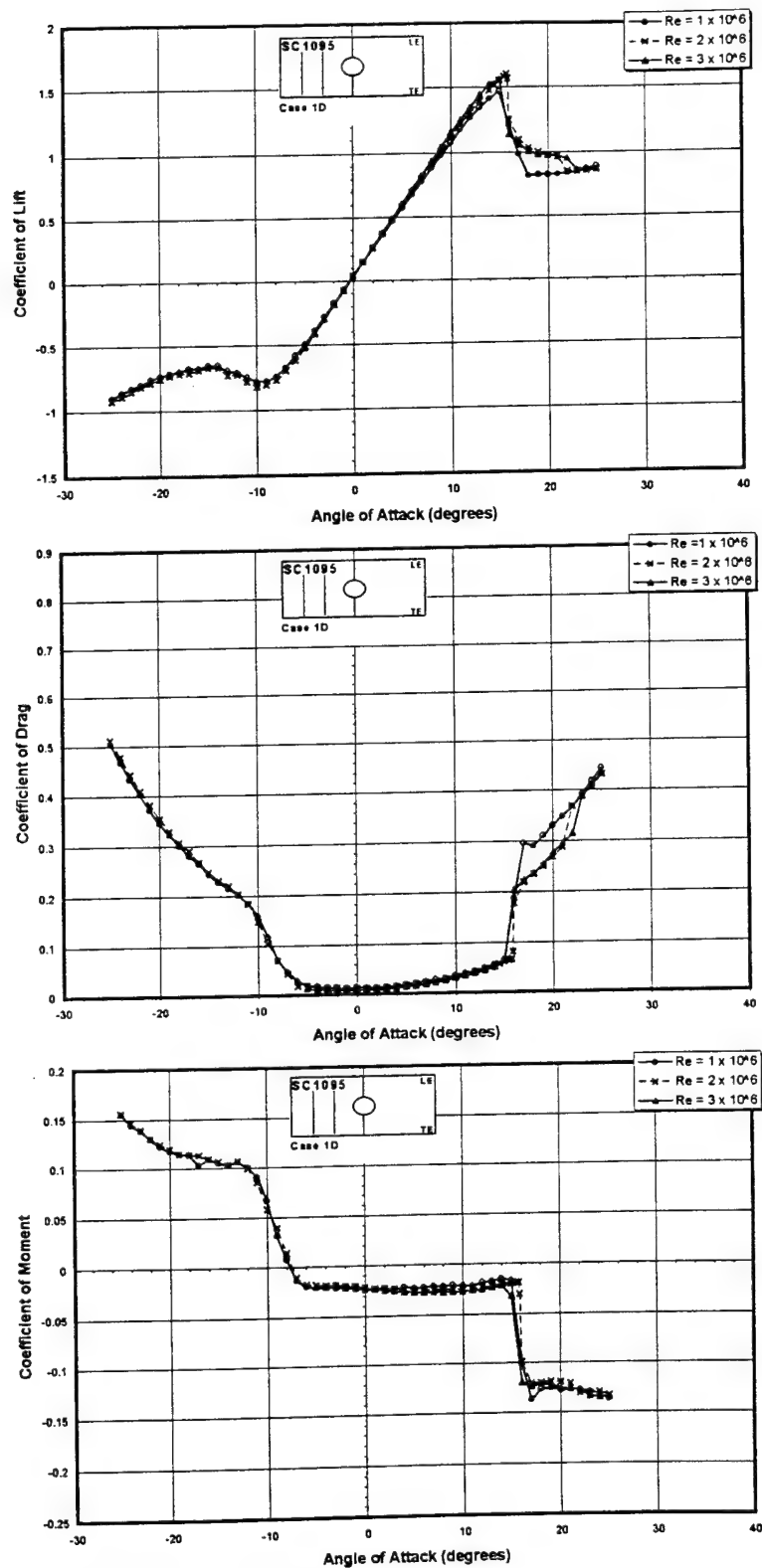
Figure 27: Aerodynamic Characteristics of Case 1D Blade Section Measured at Reynolds Numbers of 1 x 10⁶, 2 x 10⁶, and 3 x 10⁶
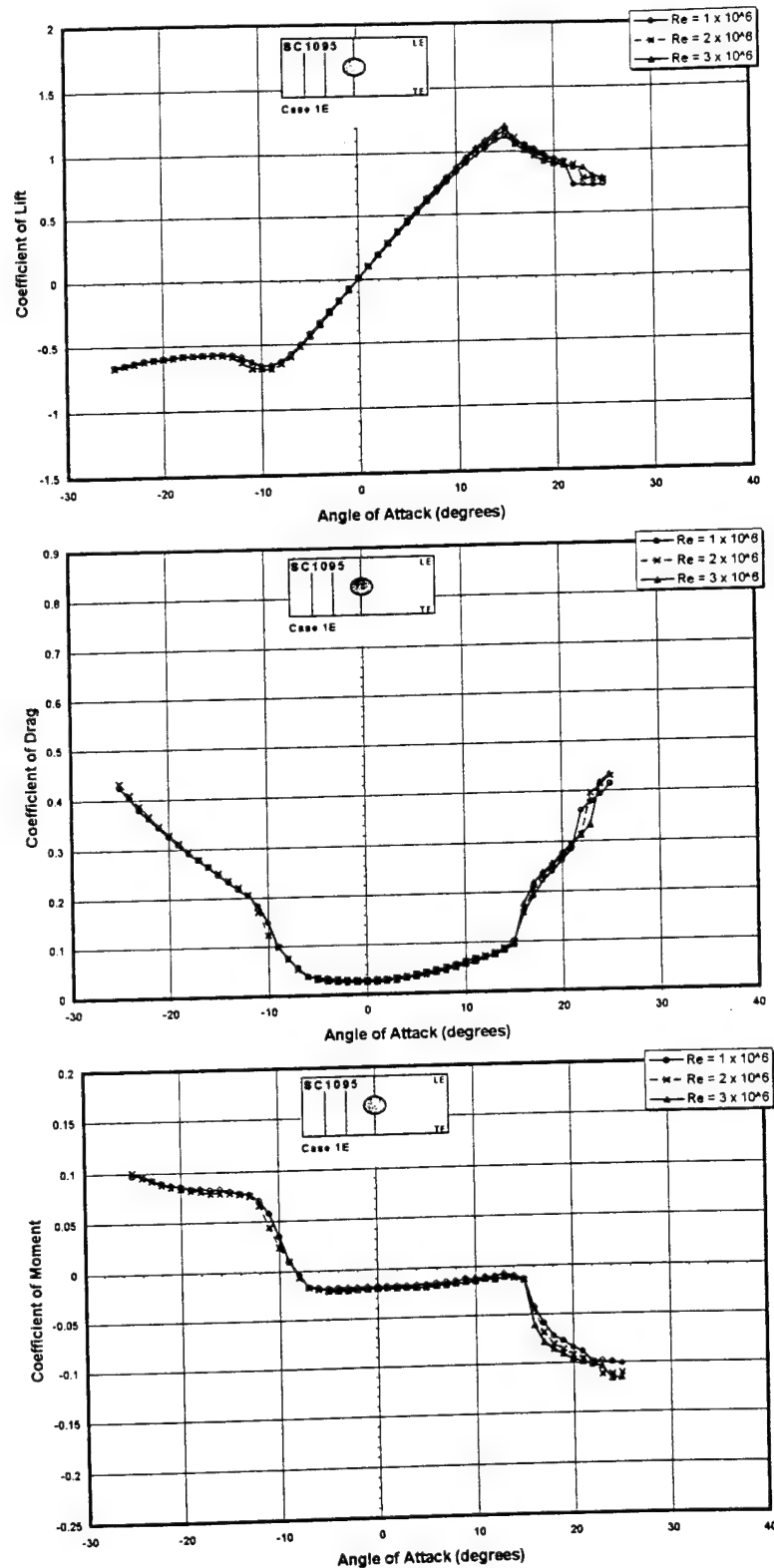
Figure 28: Aerodynamic Characteristics of Case 1E Blade Section Measured at
Reynolds Numbers of 1×10^6, 2×10^6, and 3×10^6
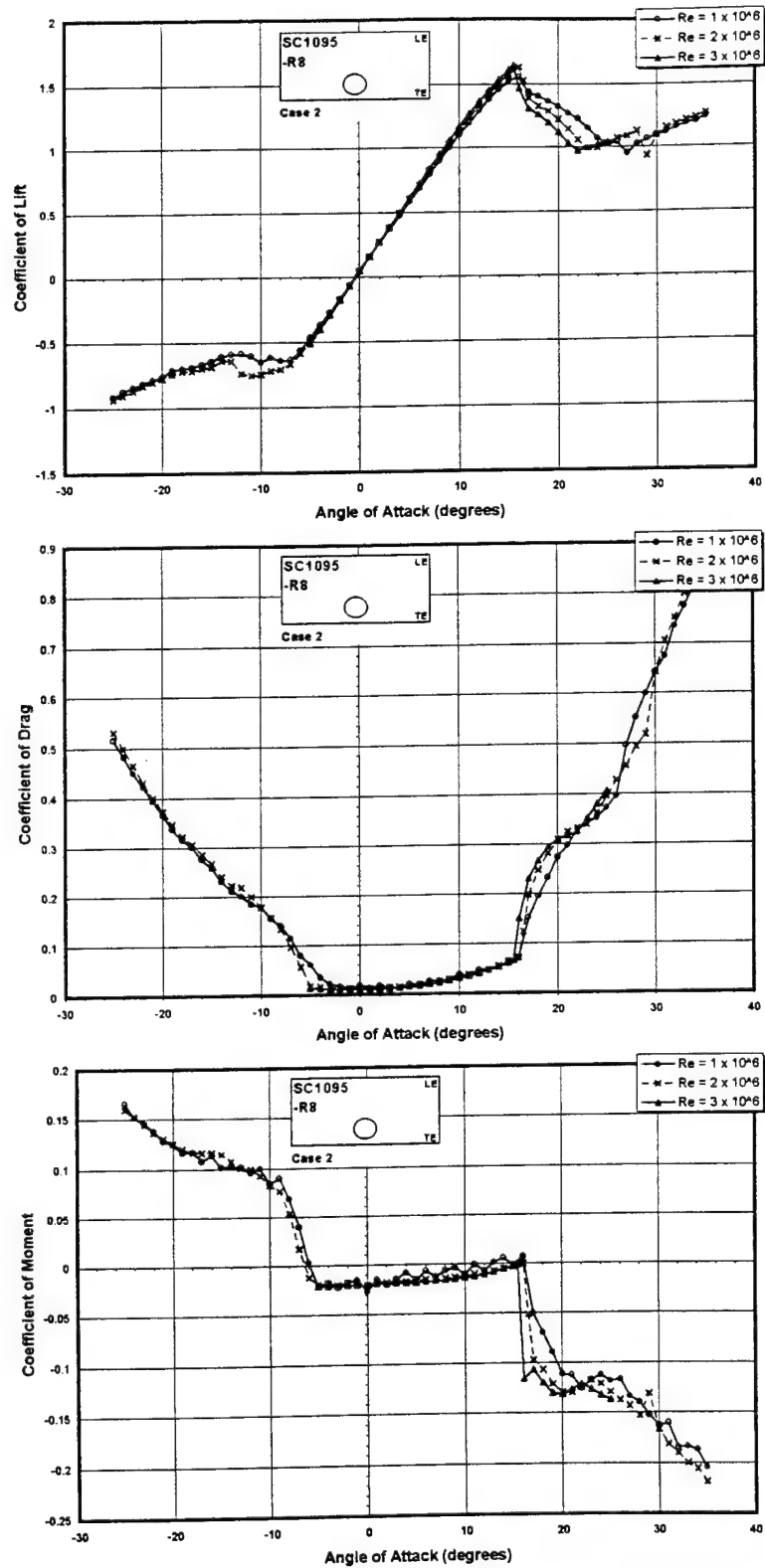
Figure 29: Aerodynamic Characteristics of Case 2 Blade Section Measured at Reynolds Numbers of 1×10^6, 2×10^6, and 3×10^6
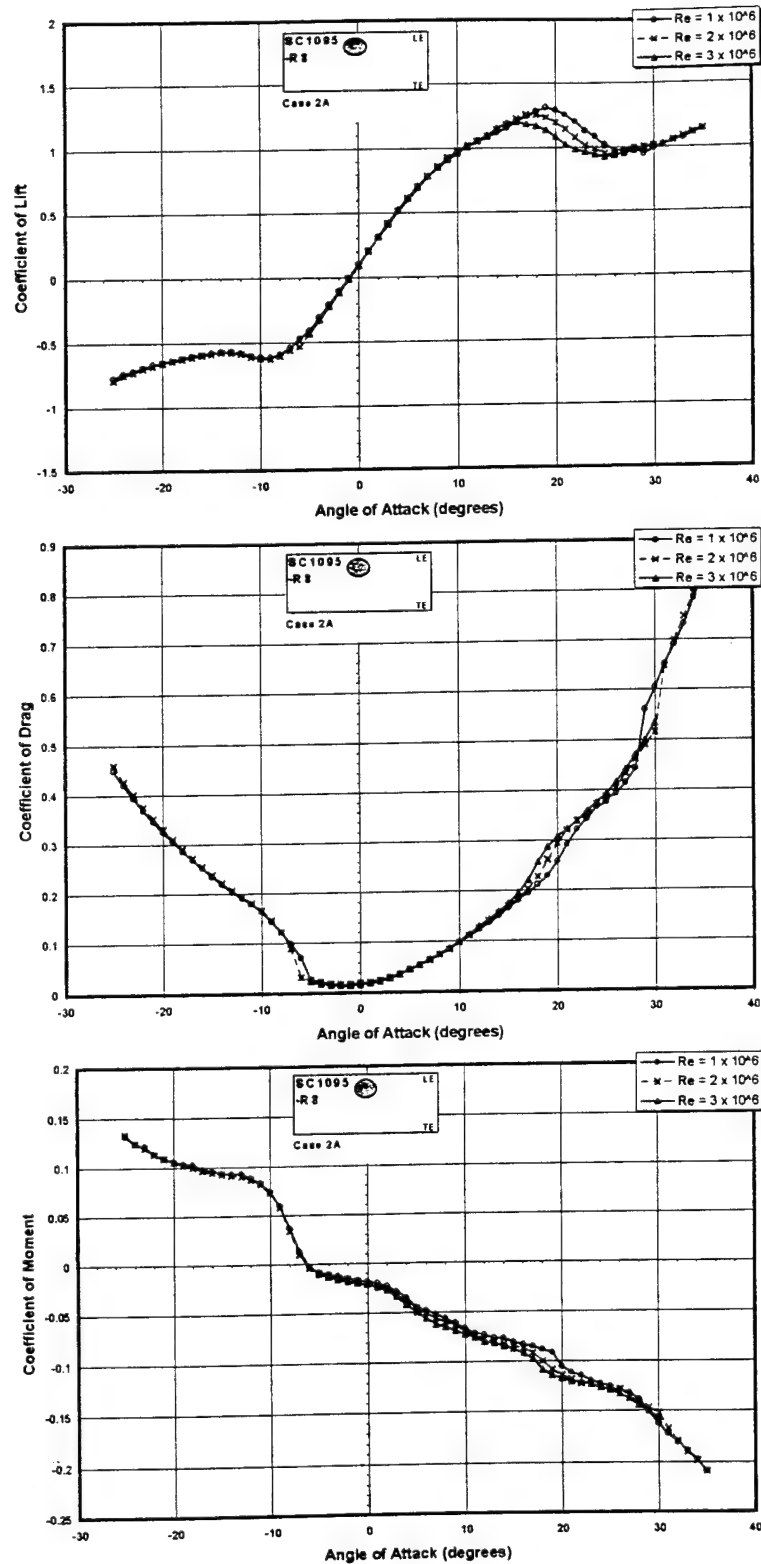
Figure 30: Aerodynamic Characteristics of Case 2A Blade Section Measured at
Reynolds Numbers of 1×10^6, 2×10^6, and 3×10^6
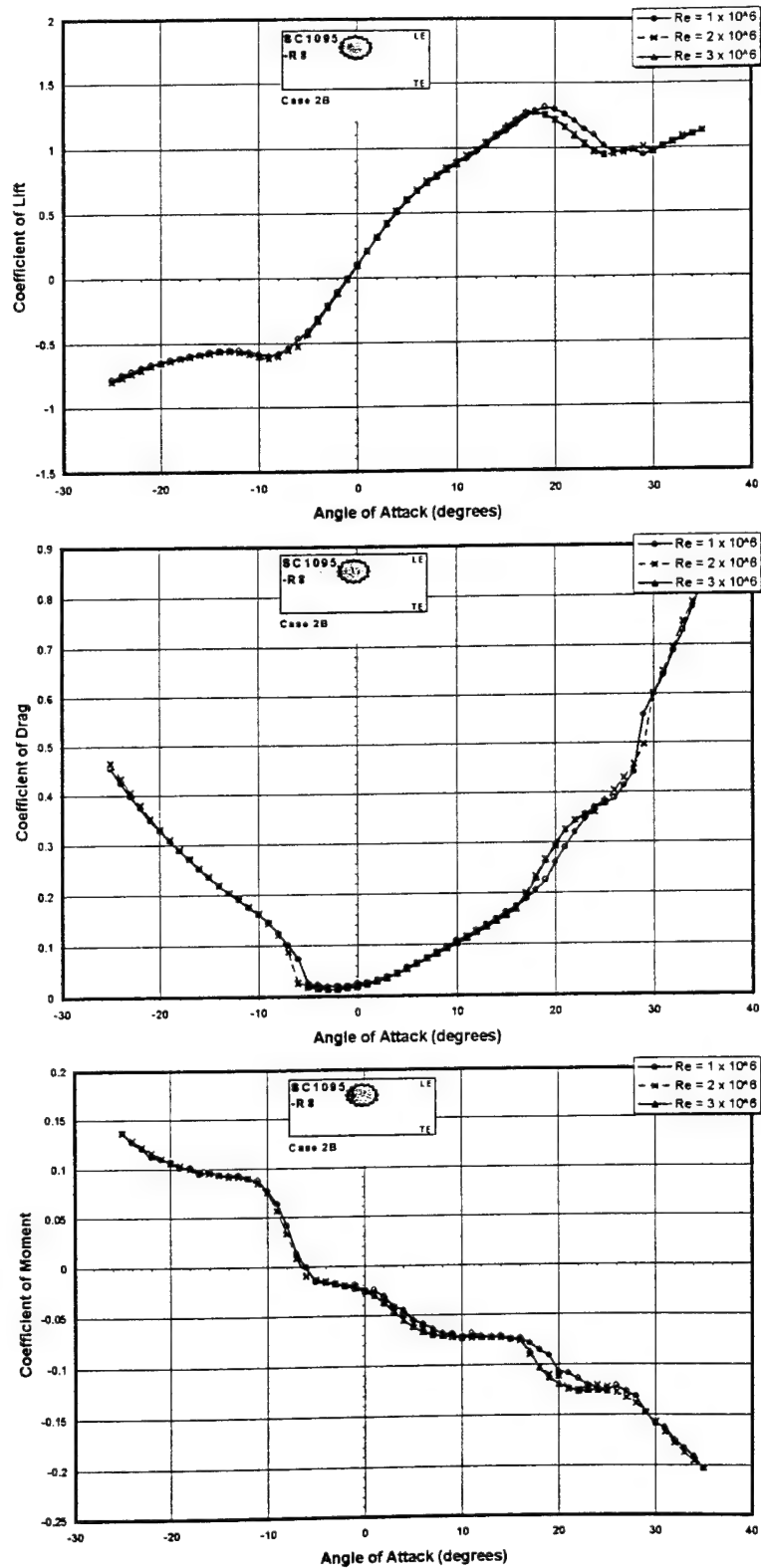
Figure 31: Aerodynamic Characteristics of Case 2B Blade Section Measured at
Reynolds Numbers of 1×10^6, 2×10^6, and 3×10^6

114
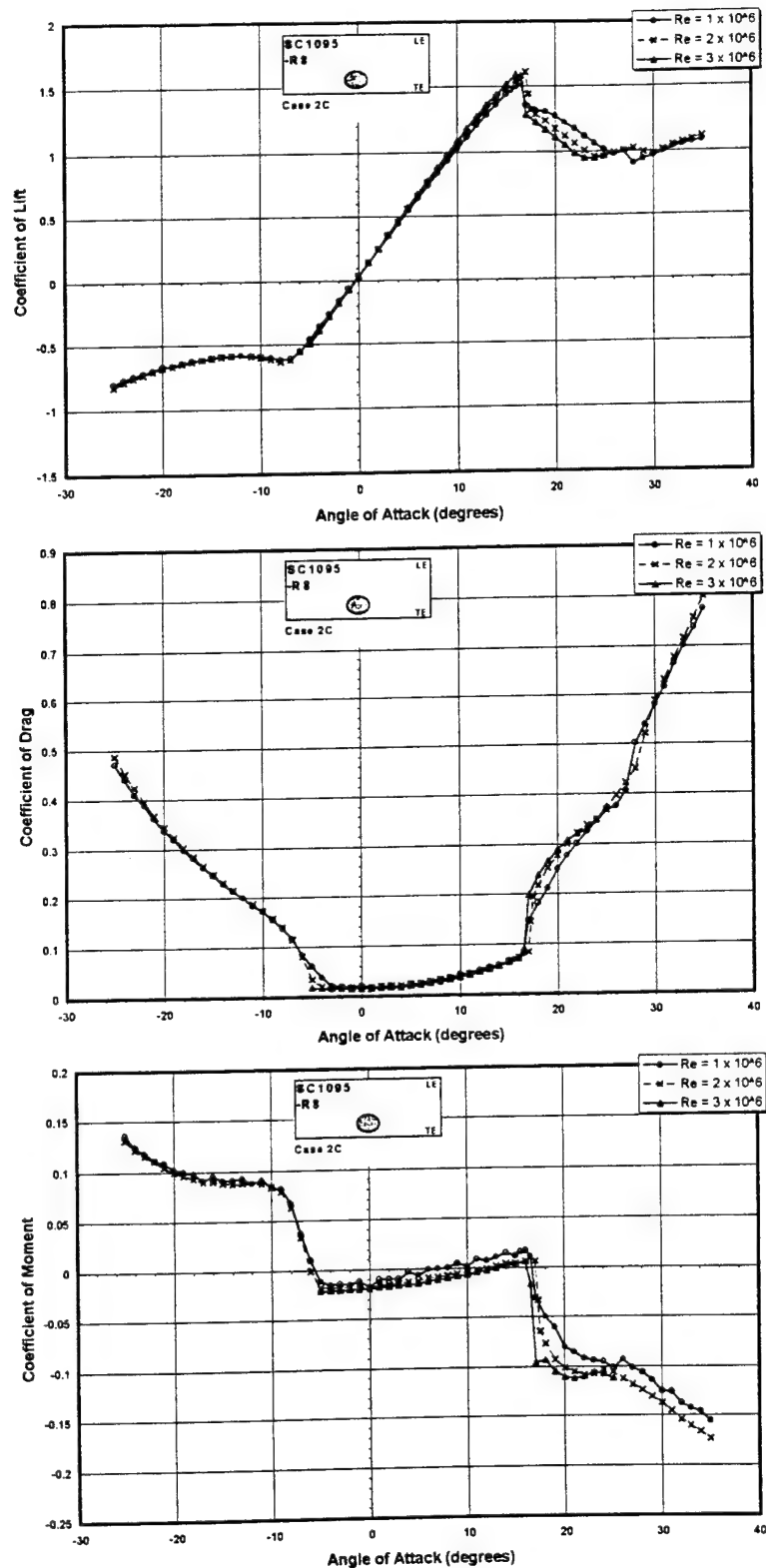
Figure 32: Aerodynamic Characteristics of Case 2C Blade Section Measured at
Reynolds Numbers of 1×10^6, 2×10^6, and 3×10^6

115
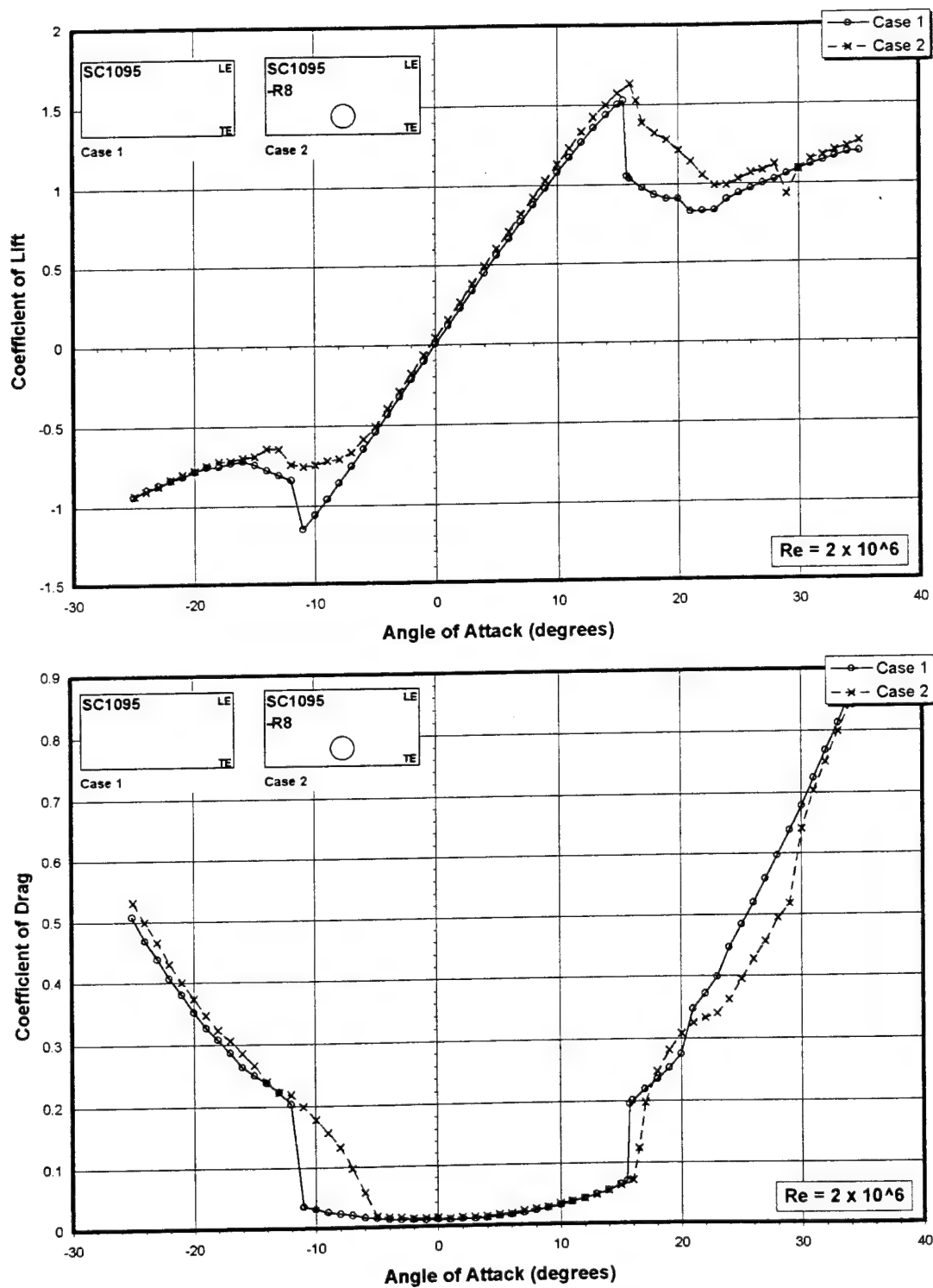
Figure 33a: Lift and Drag Measurements for Comparison 1 at Re = 2 x 10^6
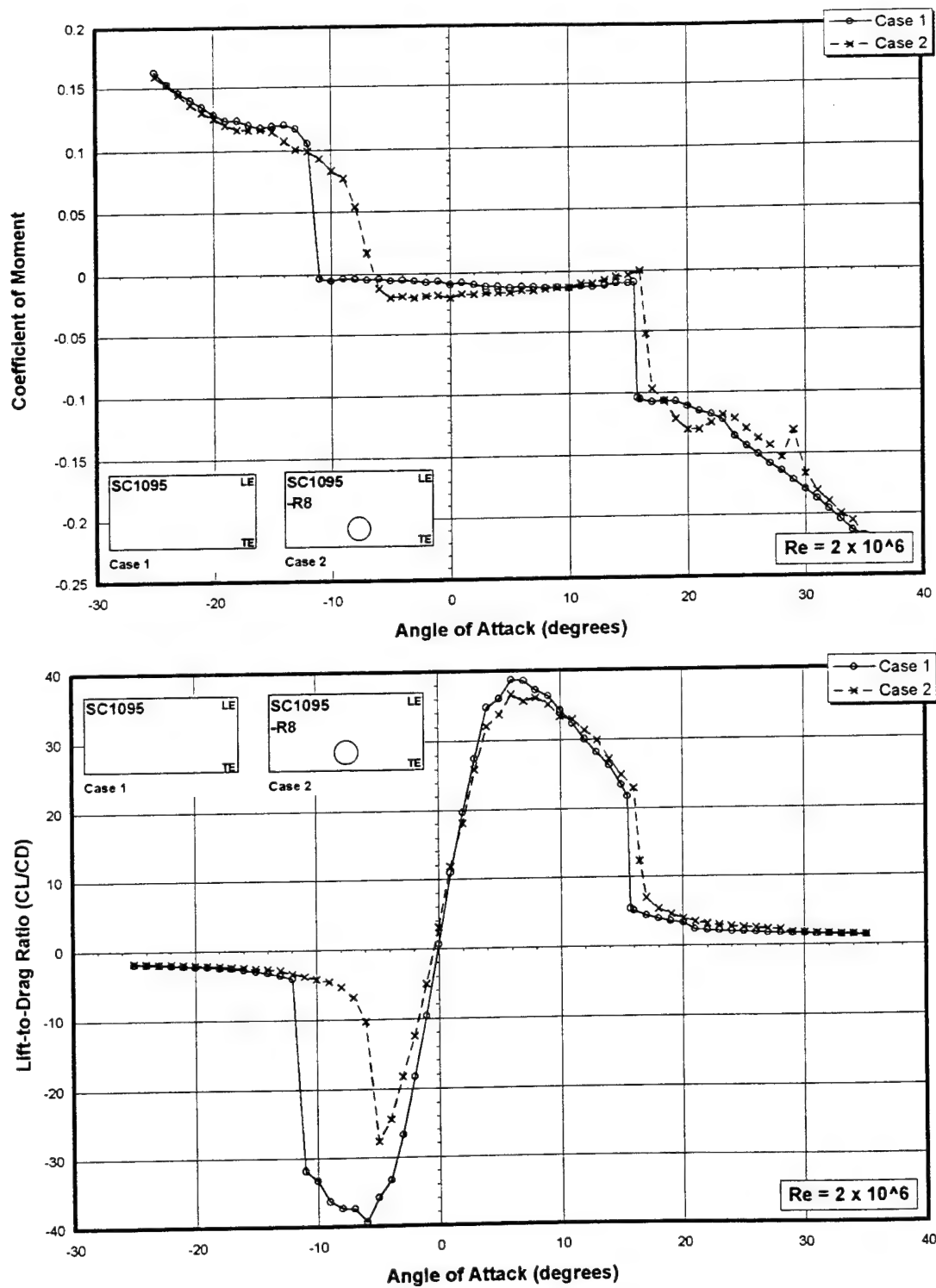
Figure 33b: Moment and Lift-to-Drag Ratio Measurements for Comparison 1 at
Re = 2 x 10^6
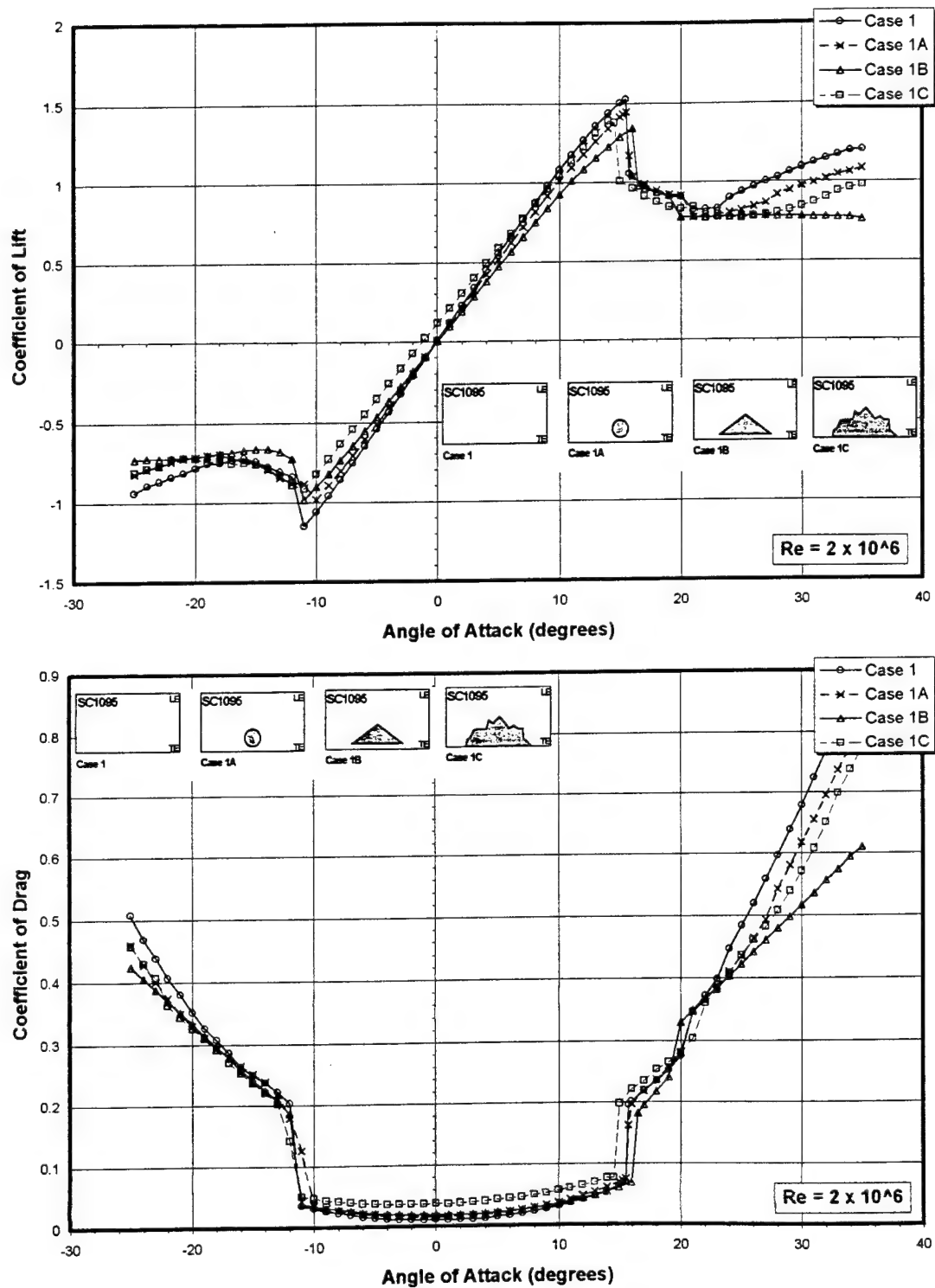
Figure 34a: Lift and Drag Measurements for Comparison 2 at Re = 2 x 10^6

118
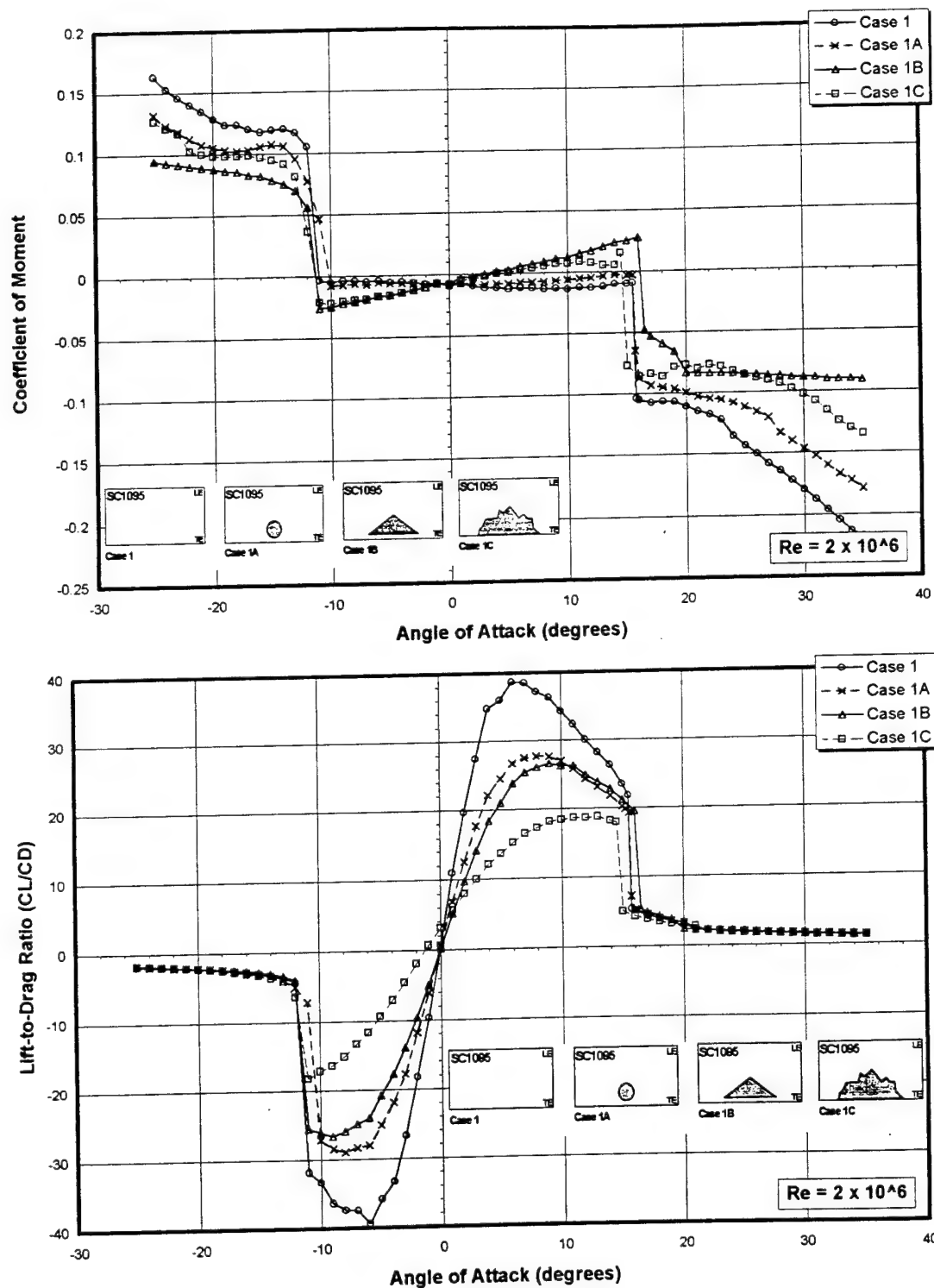
Figure 34b: Moment and Lift-to-Drag Ratio Measurements for Comparison 2 at
Re = 2 x 10^6

119
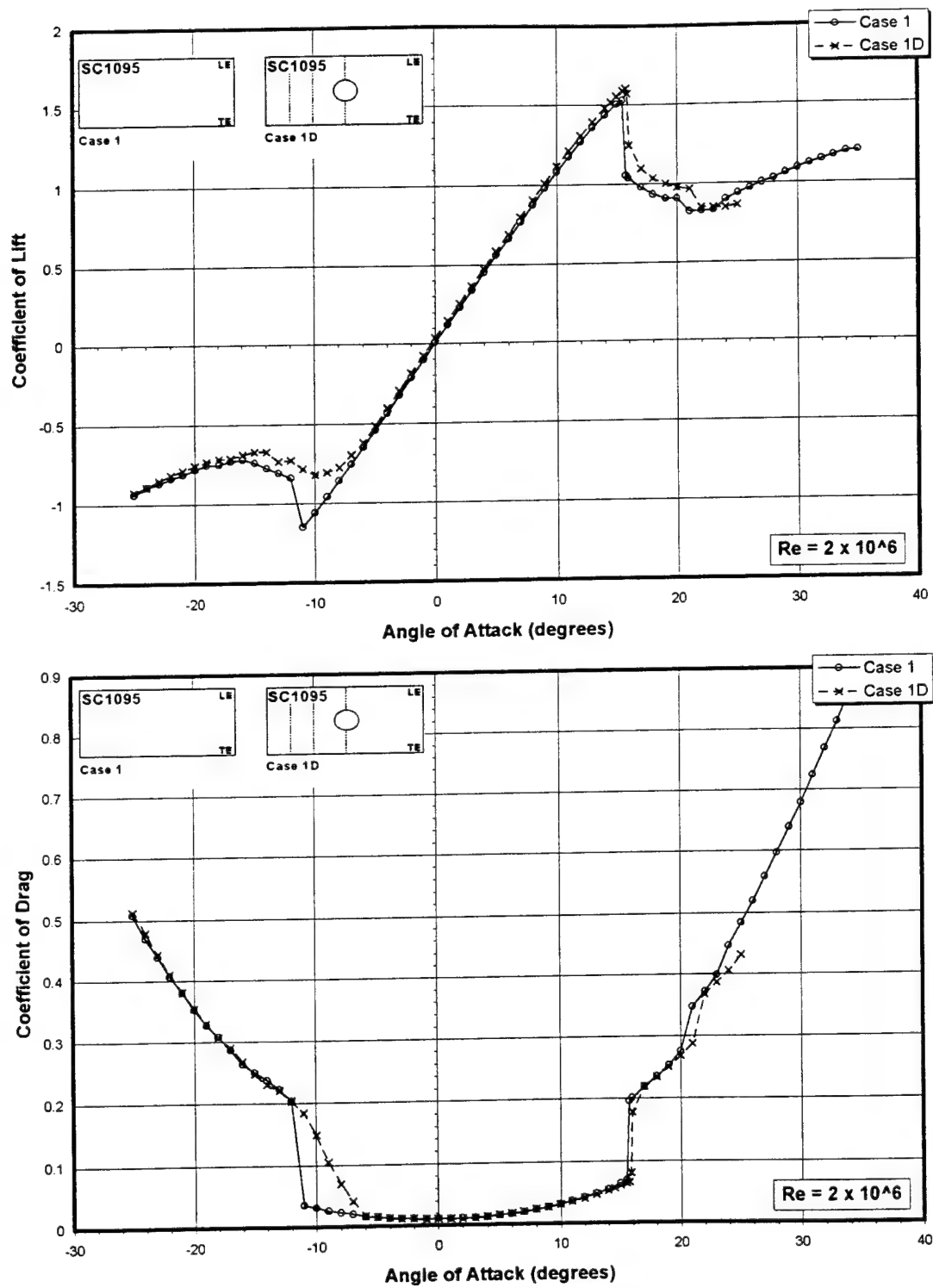
Figure 35a: Lift and Drag Measurements for Comparison 3 at Re = 2×10^6
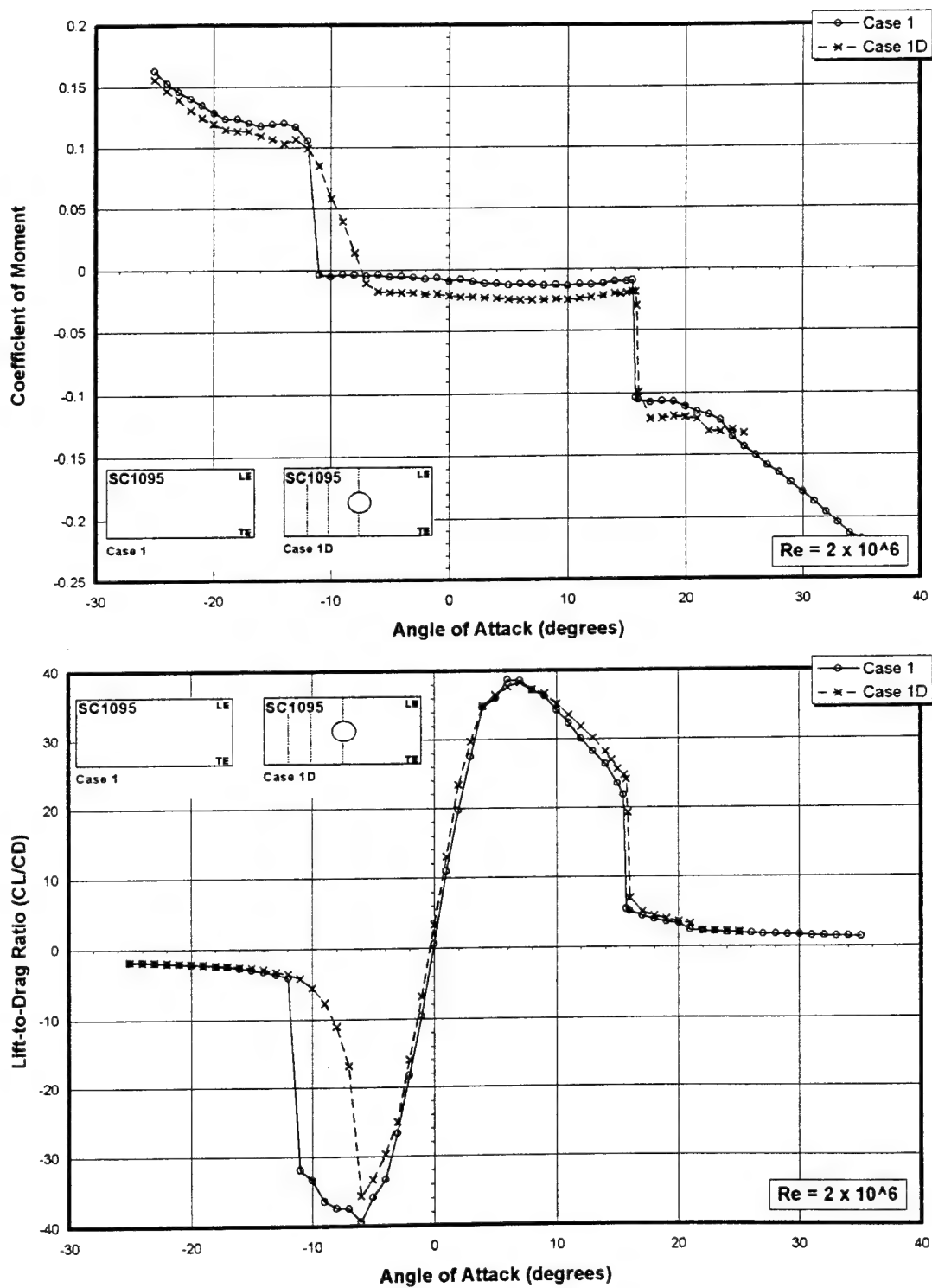
Figure 35b: Moment and Lift-to-Drag Ratio Measurements for Comparison 3 at
$Re = 2 \times 10^6$
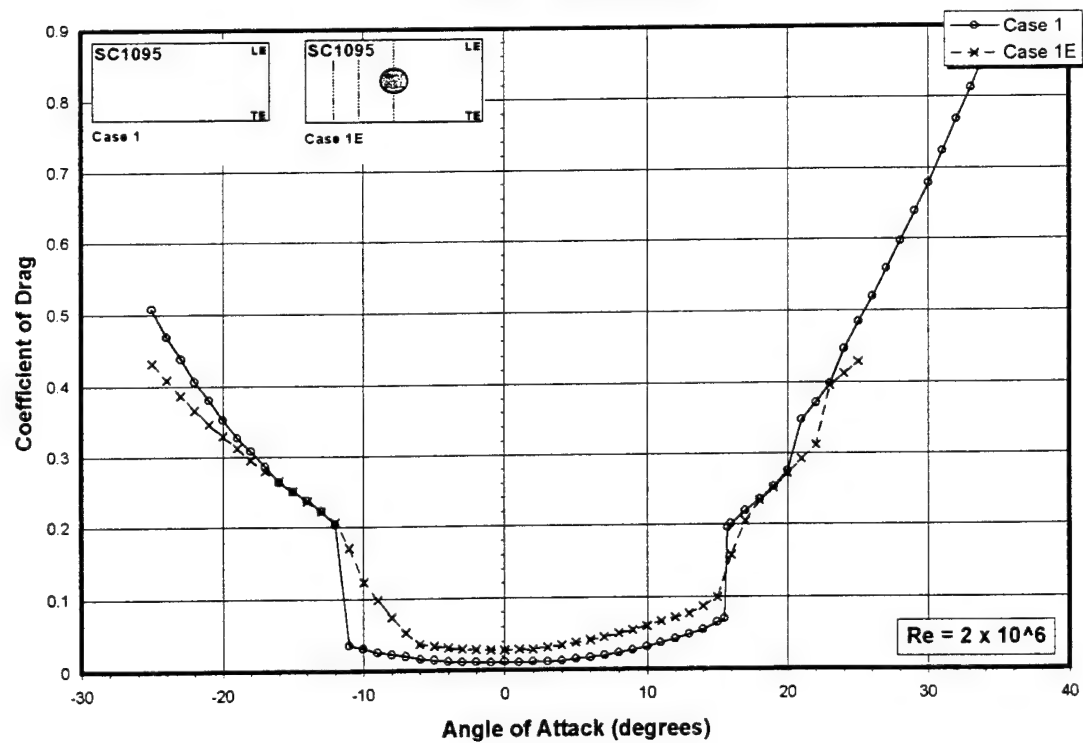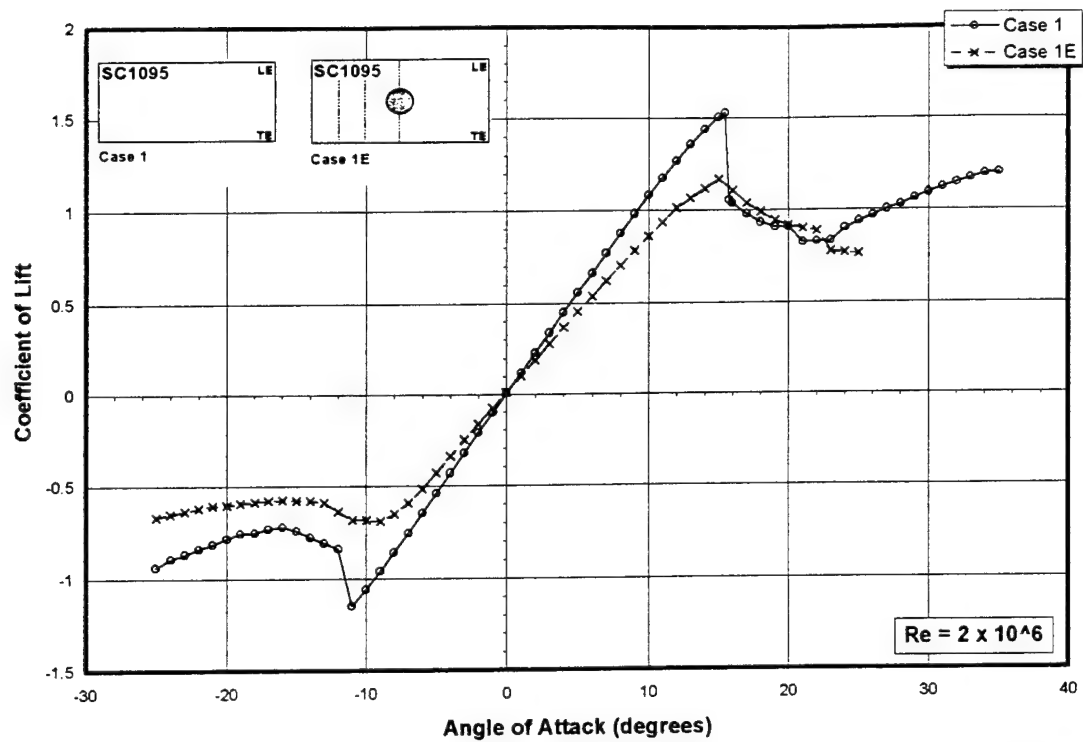
Figure 36a: Lift and Drag Measurements for Comparison 4 at Re = 2×10^6
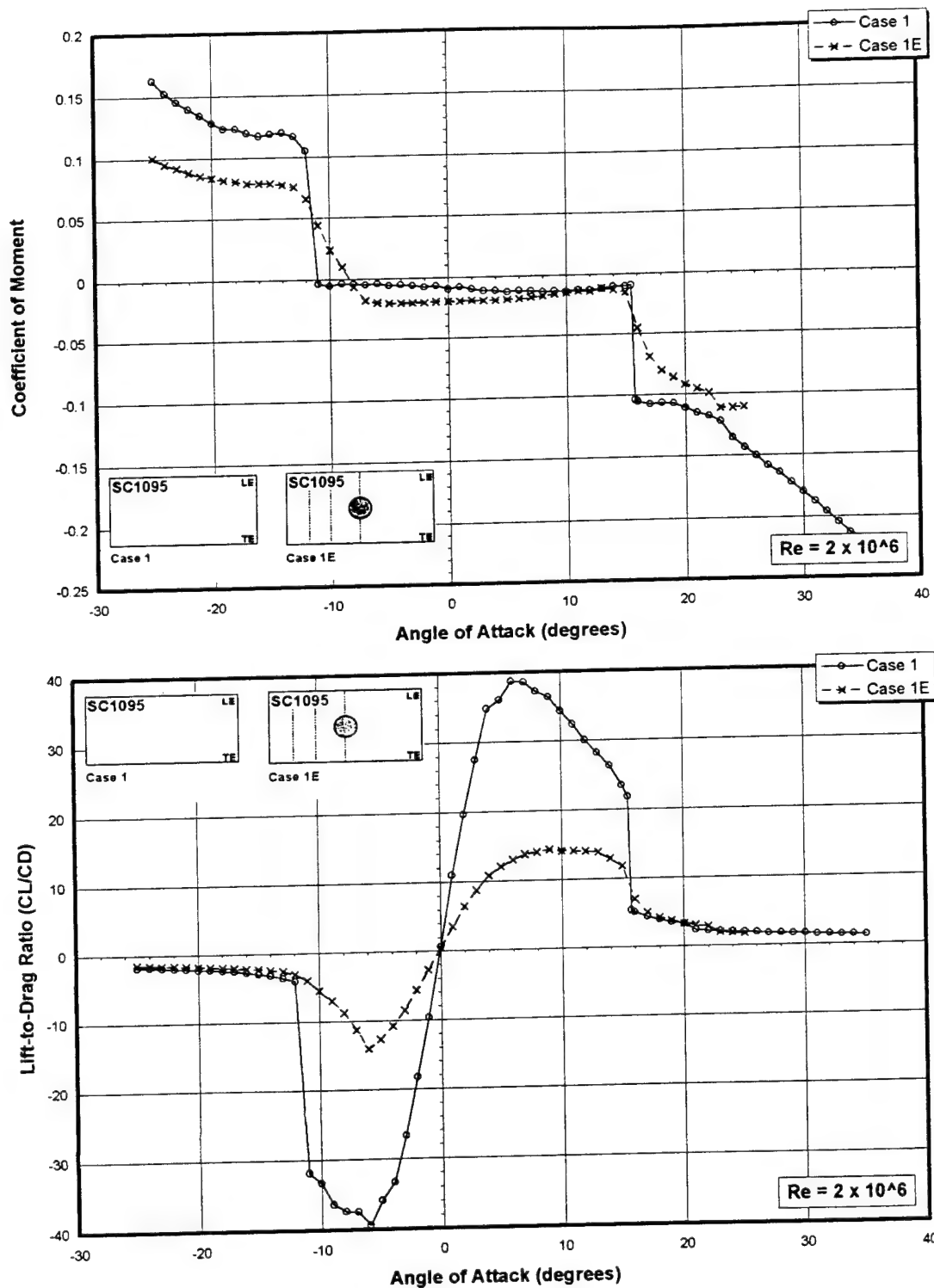
Figure 36b: Moment and Lift-to-Drag Ratio Measurements for Comparison 4 at
Re = 2 x 10^6
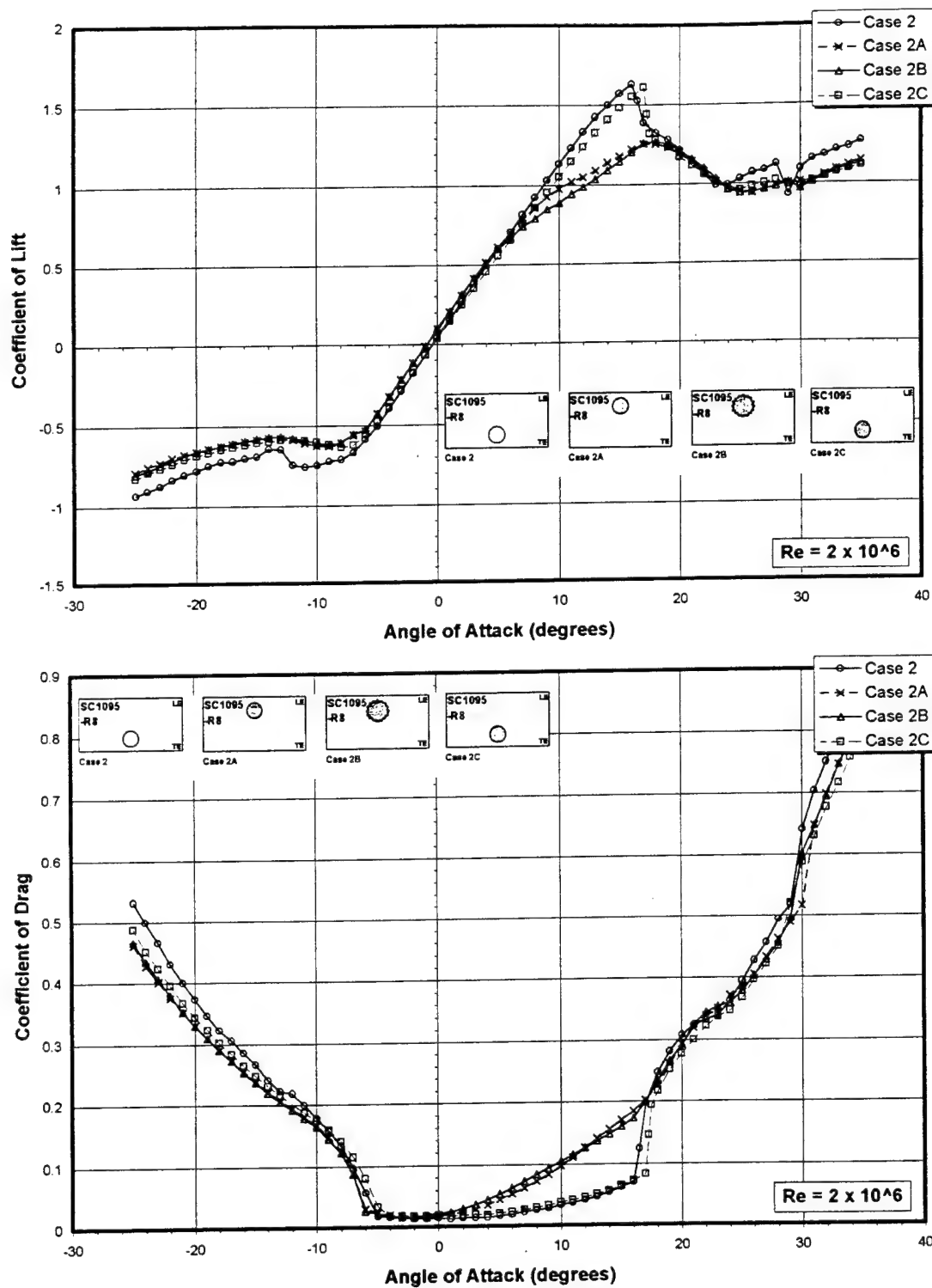
Figure 37a: Lift and Drag Measurements for Comparison 5 at Re = 2 x 10^6

124
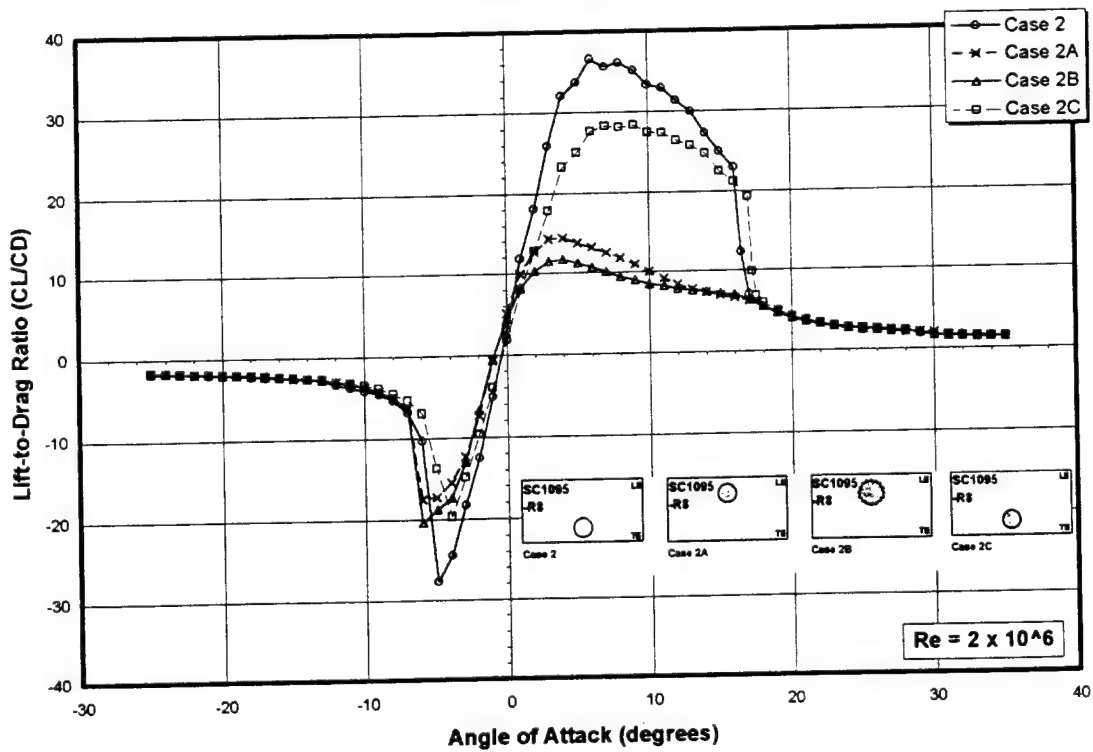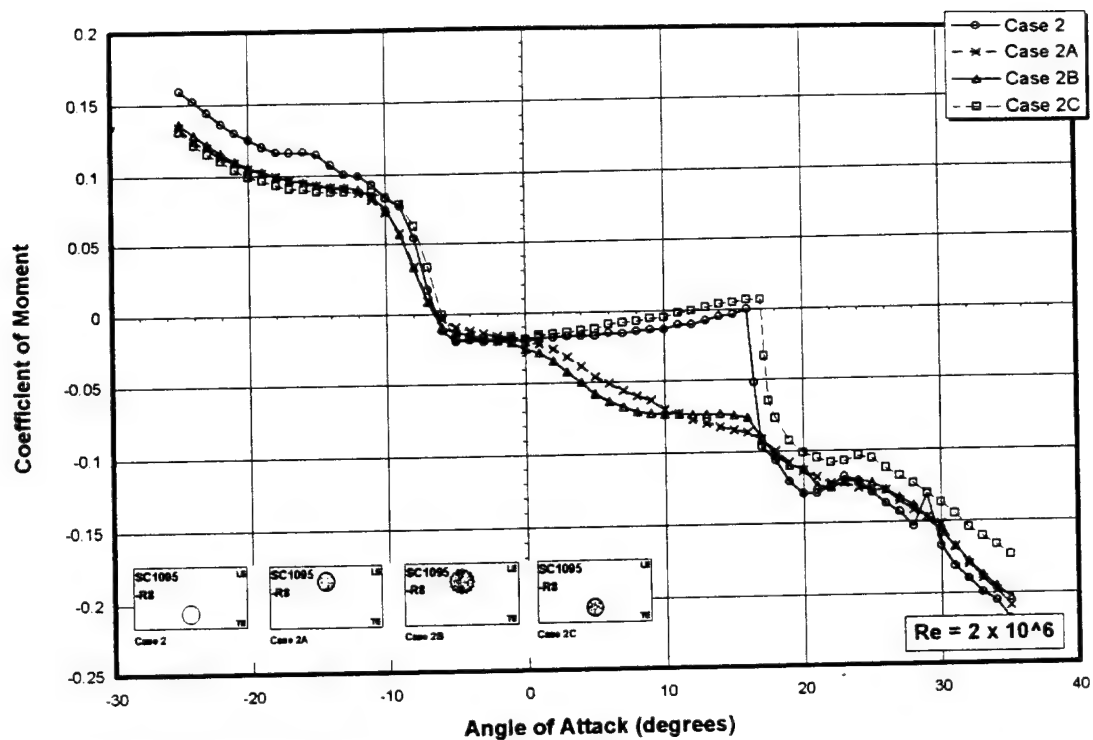
Figure 37b: Moment and Lift-to-Drag Ratio Measurements for Comparison 5 at $Re = 2 \times 10^6$

125
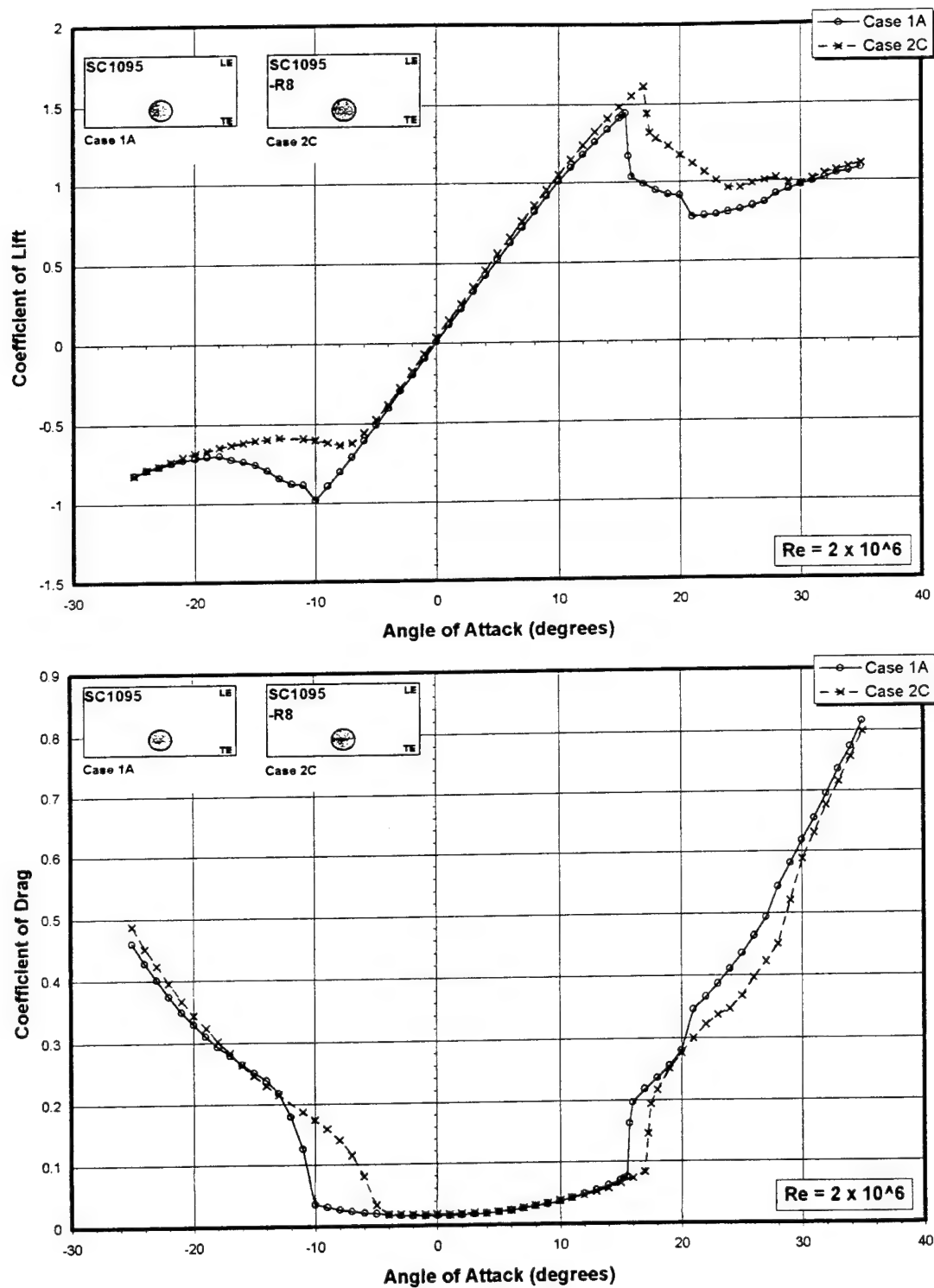
Figure 38a: Lift and Drag Measurements for Comparison 6 at Re = 2 x 10⁶

126

Figure 38b: Moment and Lift-to-Drag Ratio Measurements for Comparison 6 at
$Re = 2 \times 10^6$

127
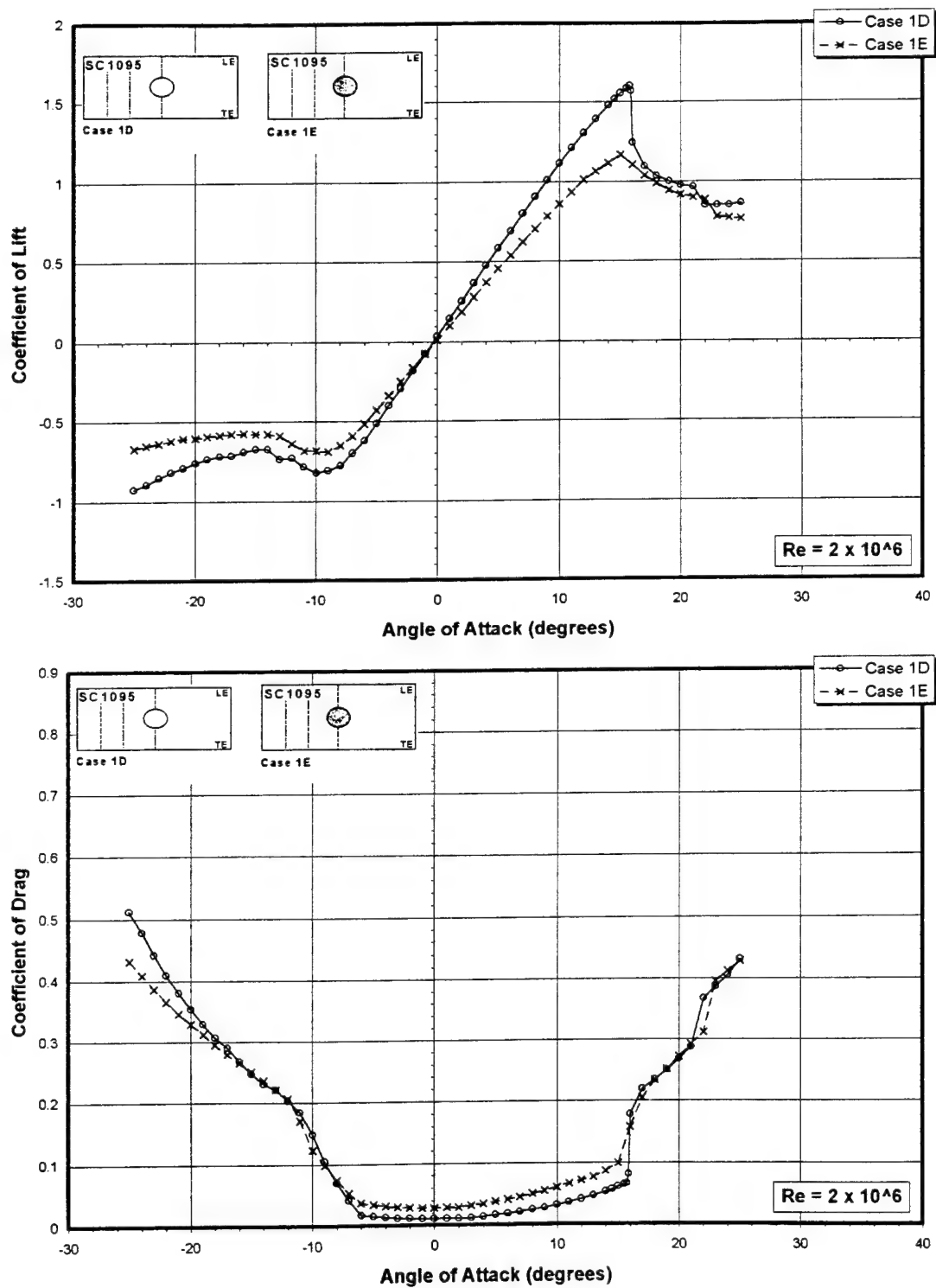
Figure 39a: Lift and Drag Measurements for Comparison 7 at Re = 2 x 10^6
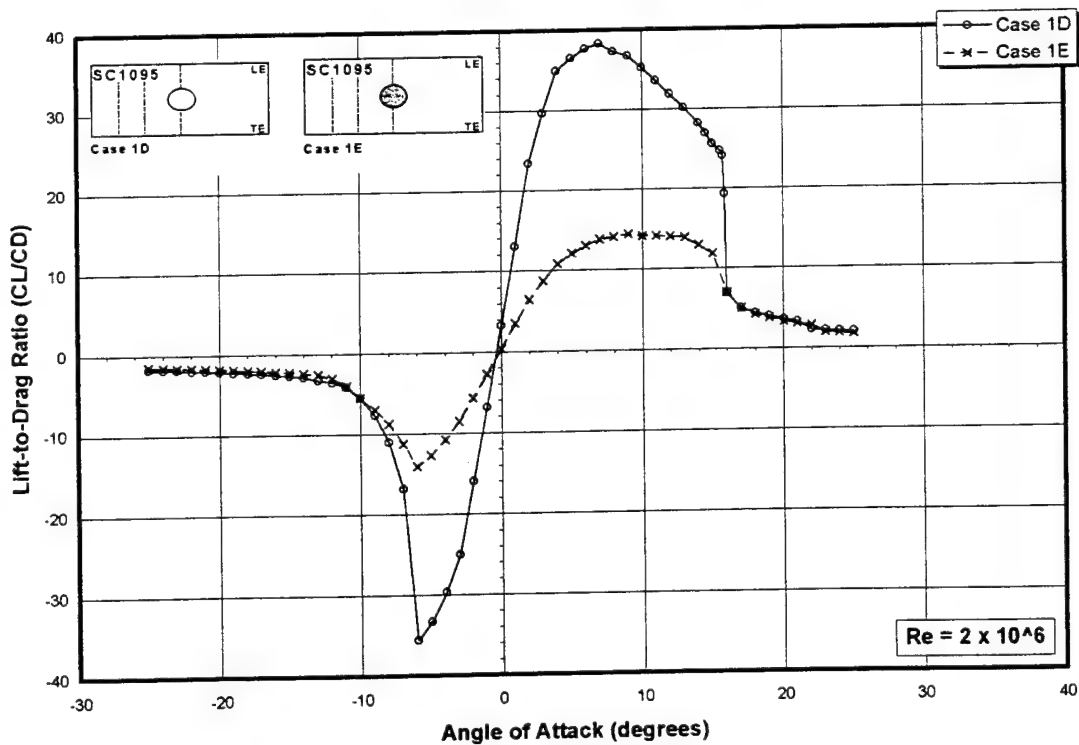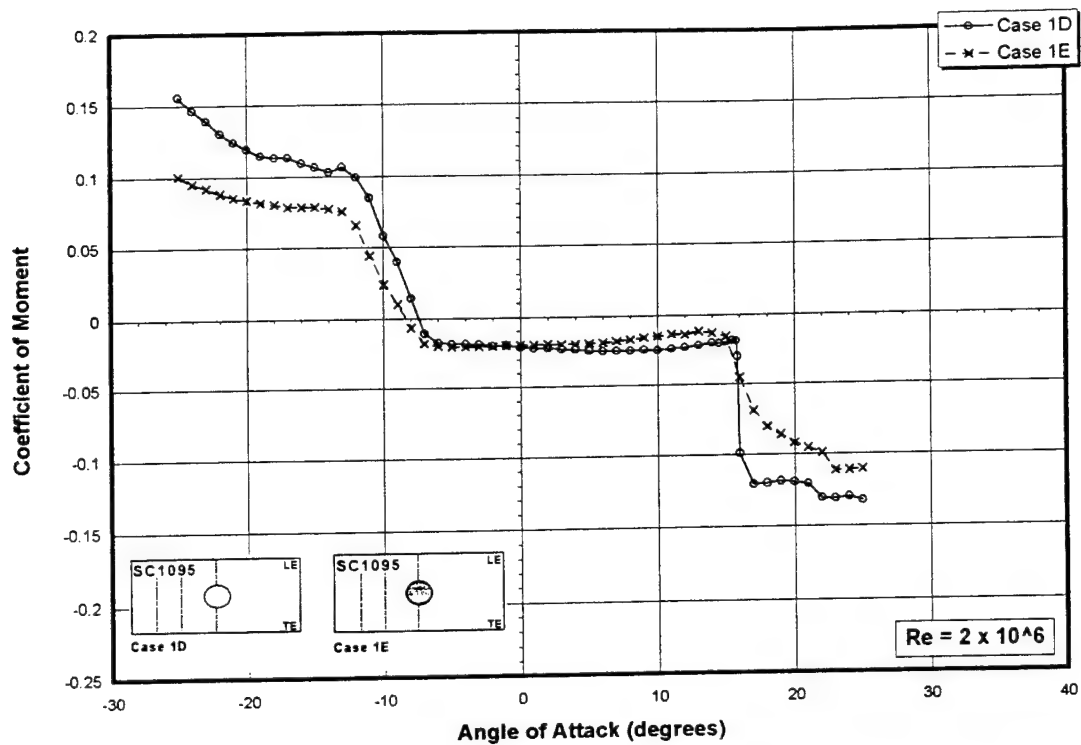
Figure 39b: Moment and Lift-to-Drag Ratio Measurements for Comparison 7 at
Re = 2 x 10^6
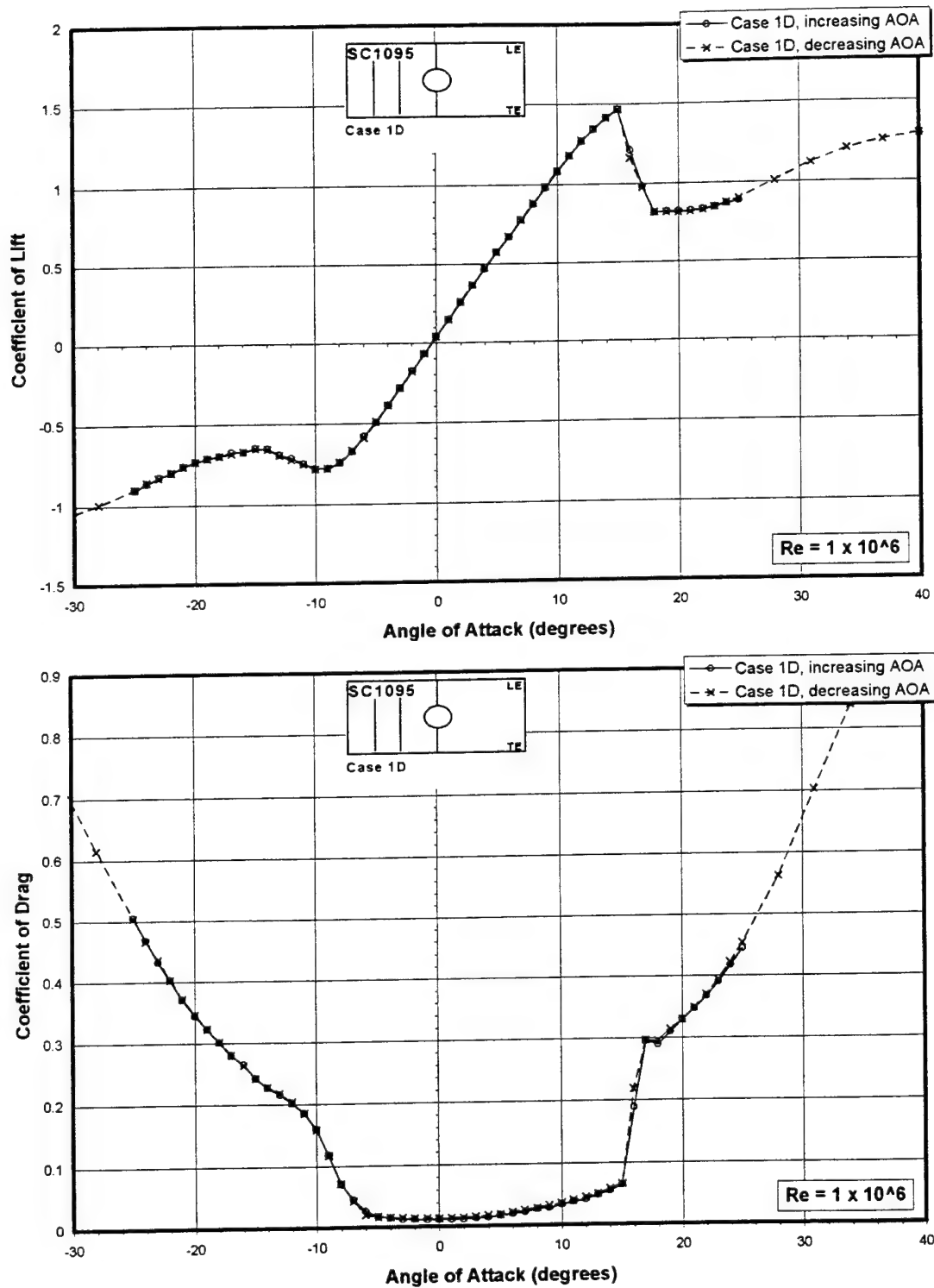
Figure 40a: Lift and Drag Measurements for Increasing and Decreasing Angles of Attack for Case 1D at Re = 1 x 10^6
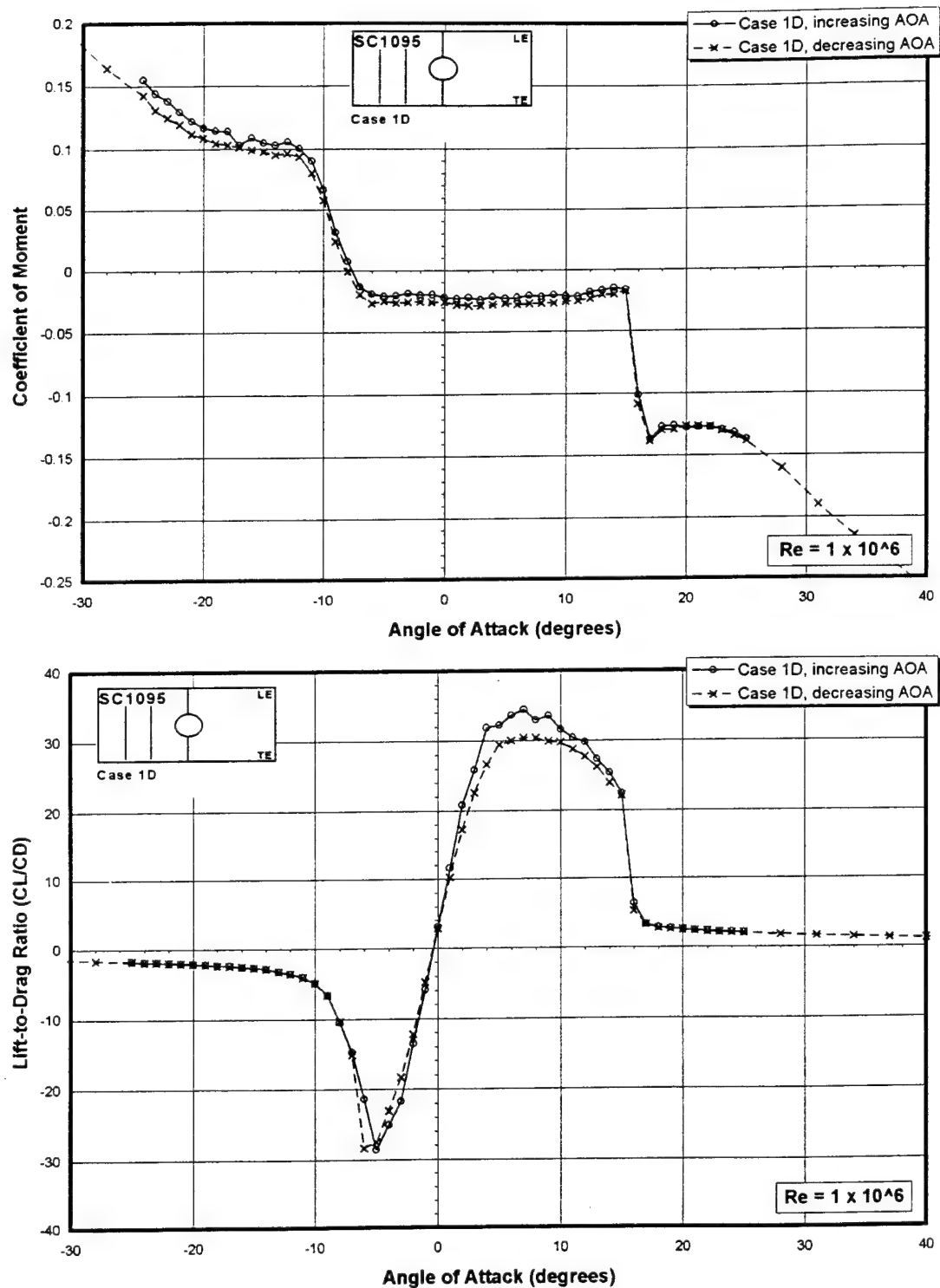
Figure 40b: Moment and Lift-Curve-Slope Measurements for Increasing and Decreasing Angles of Attack for Case 1D at Re = 1 x 10^6

131
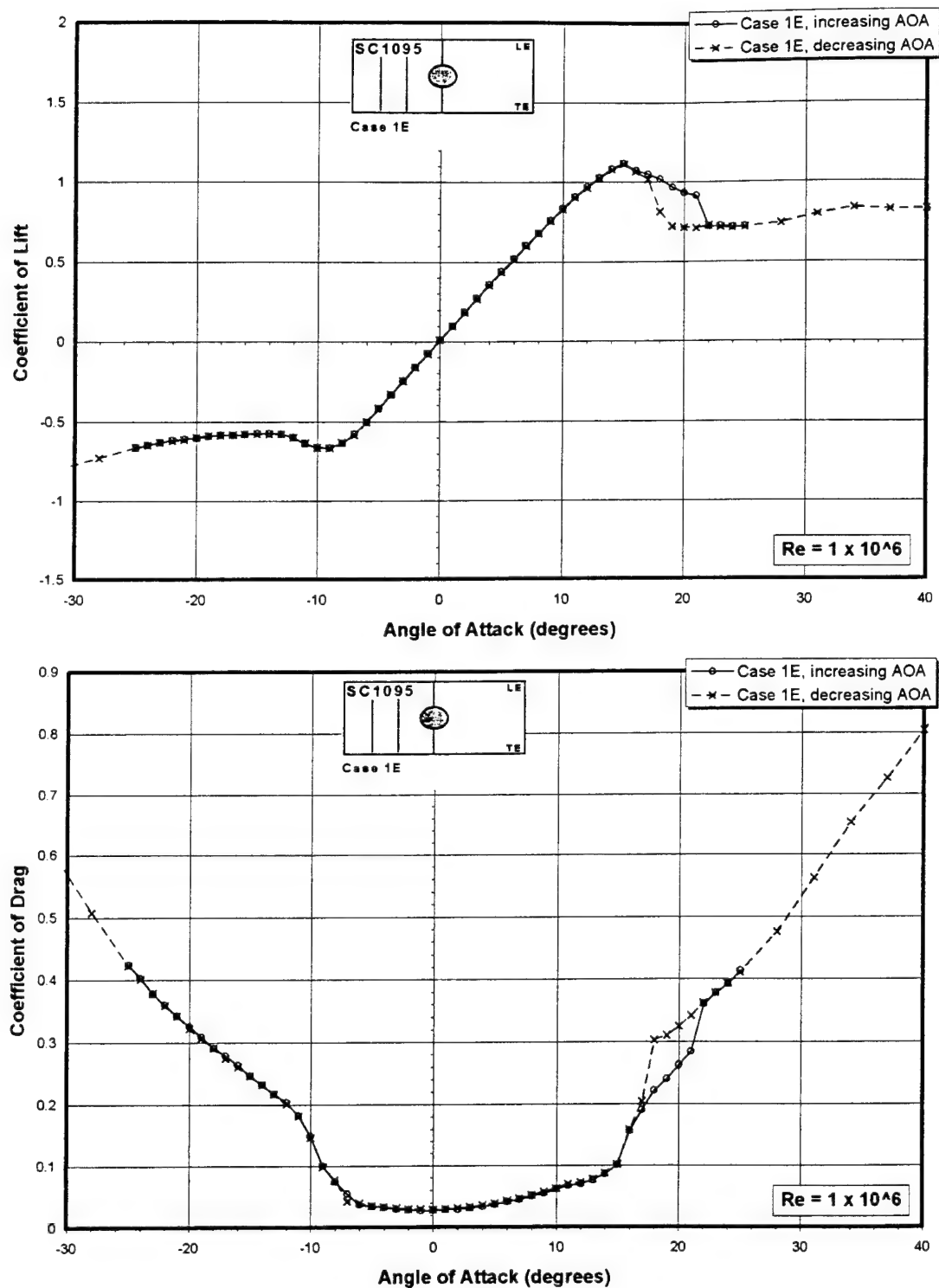
Figure 41a: Lift and Drag Measurements for Increasing and Decreasing Angles of Attack for Case 1E at Re = 1 x 10^6

132
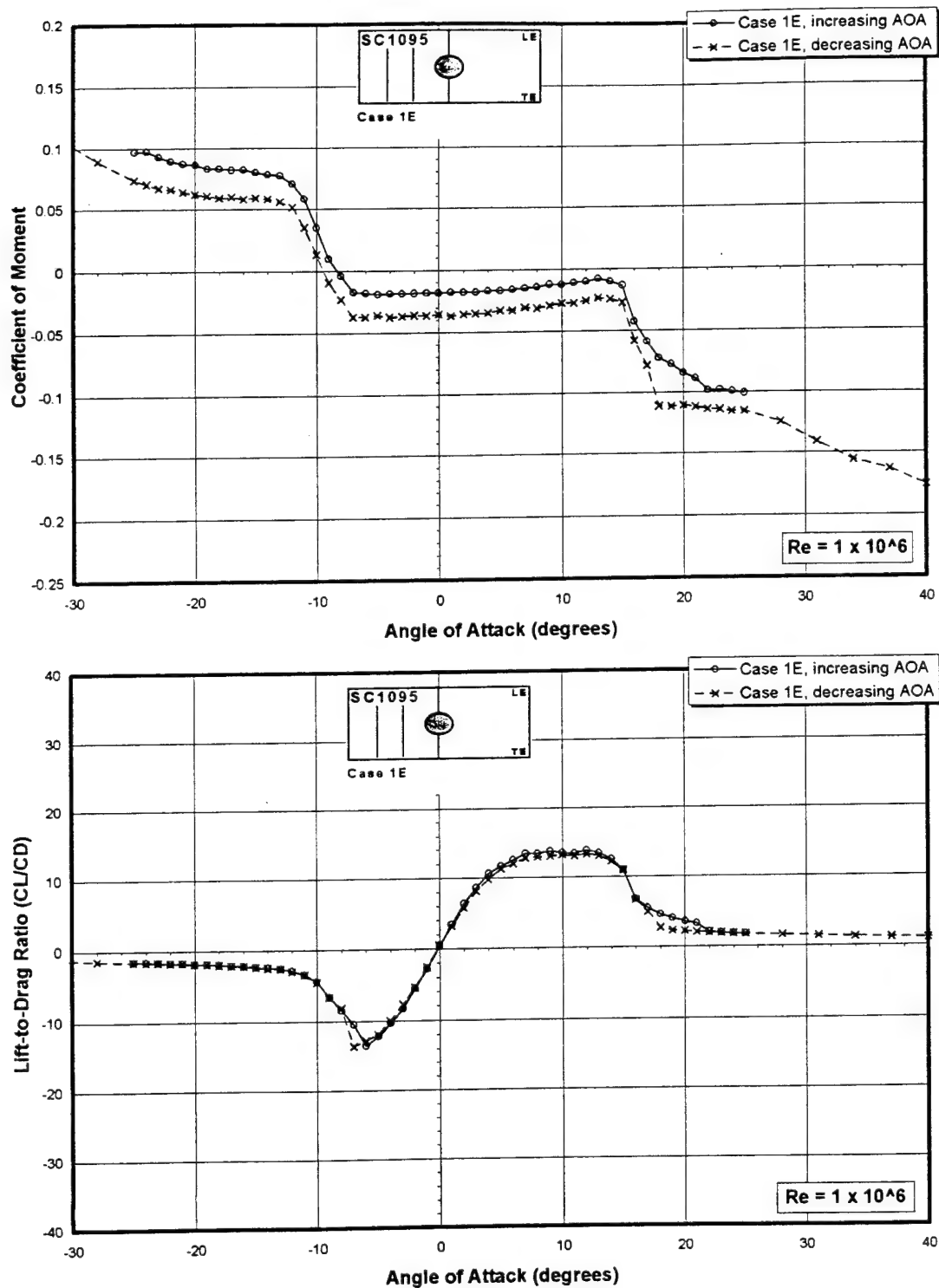
Figure 41b: Moment and Lift-Curve-Slope Measurements for Increasing and Decreasing Angles of Attack for Case 1E at Re = 1 x 10^{6}
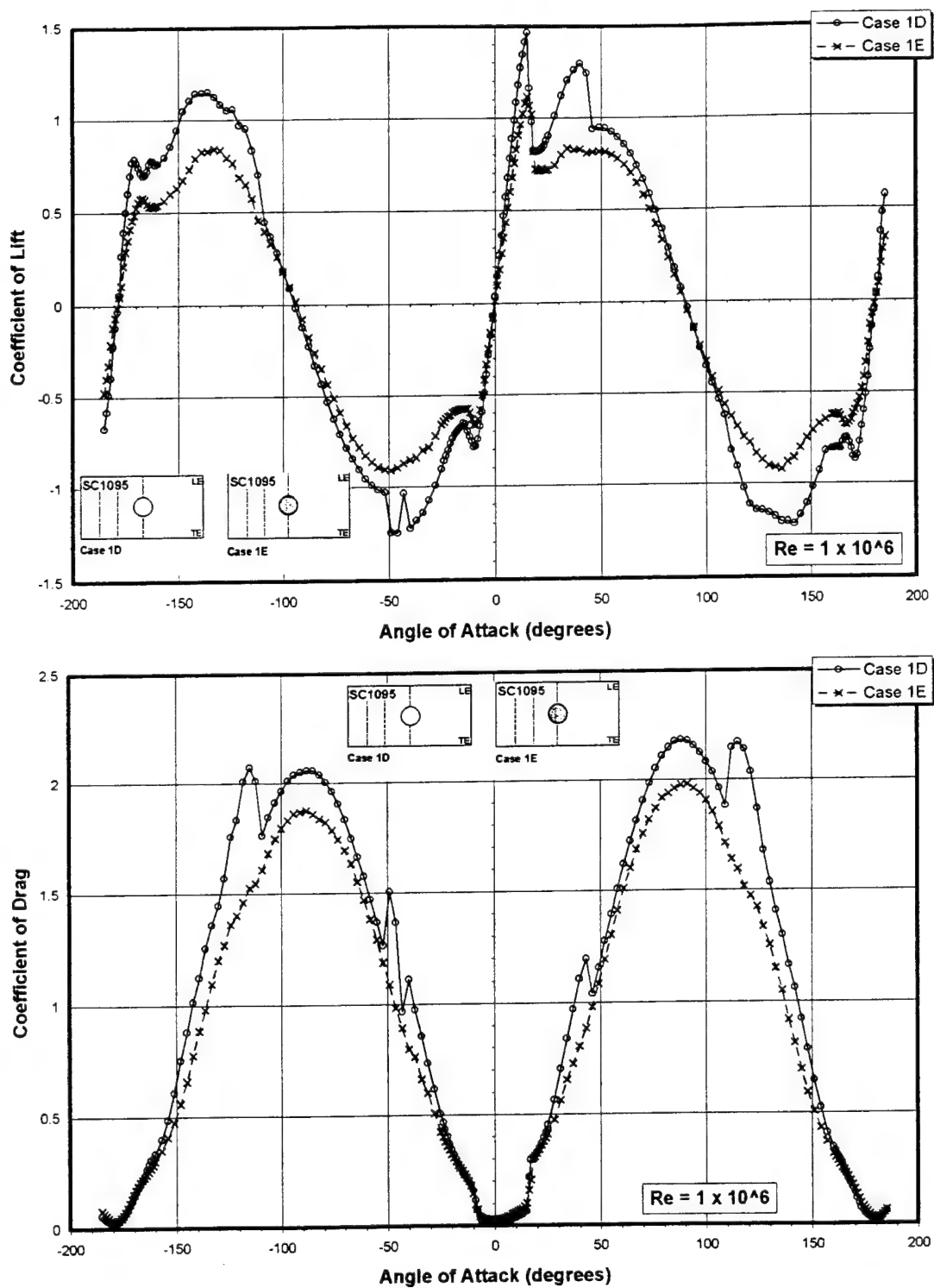
Figure 42a: Lift and Drag Characteristics in the High Angle of Attack and Reverse Flow Regions for Case 1D and Case 1E at Re = 1 x 10^{6}
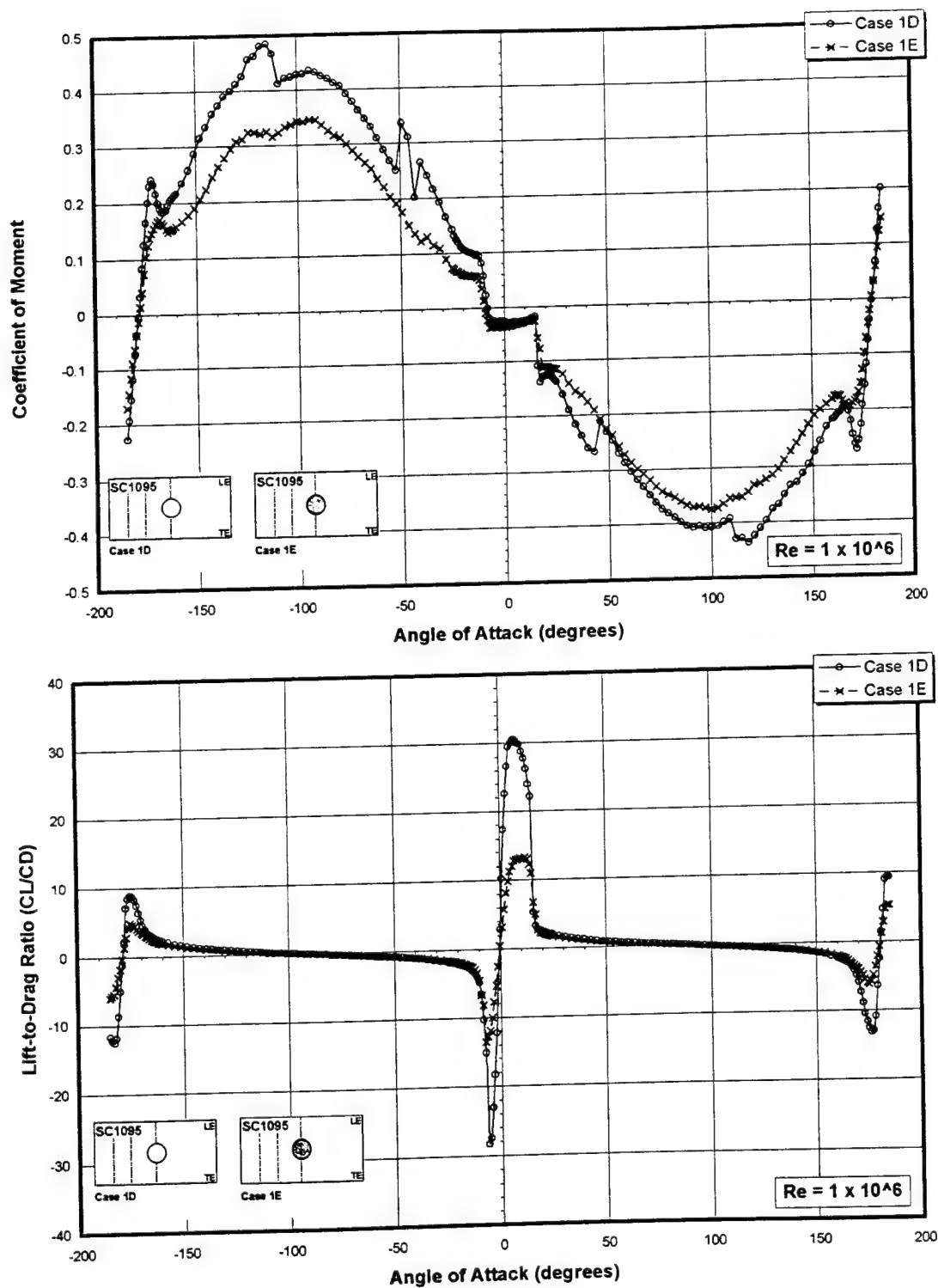
Figure 42b: Moment and Lift-Curve-Slope Characteristics in the High Angle of Attack and Reverse Flow Regions for Case 1D and Case 1E at Re = 1 x 10^6
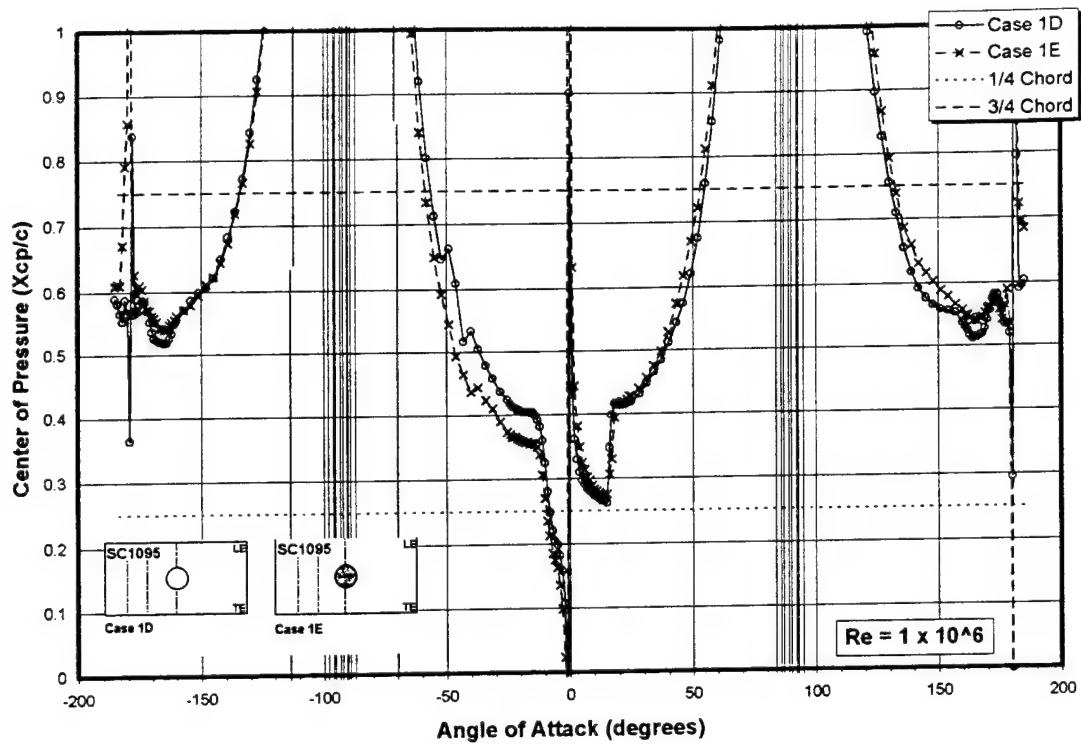
Figure 42c: Center of Pressure Characteristics in the High Angle of Attack and Reverse Flow Regions for Case 1D and Case 1E at Re = 1 x 10^6
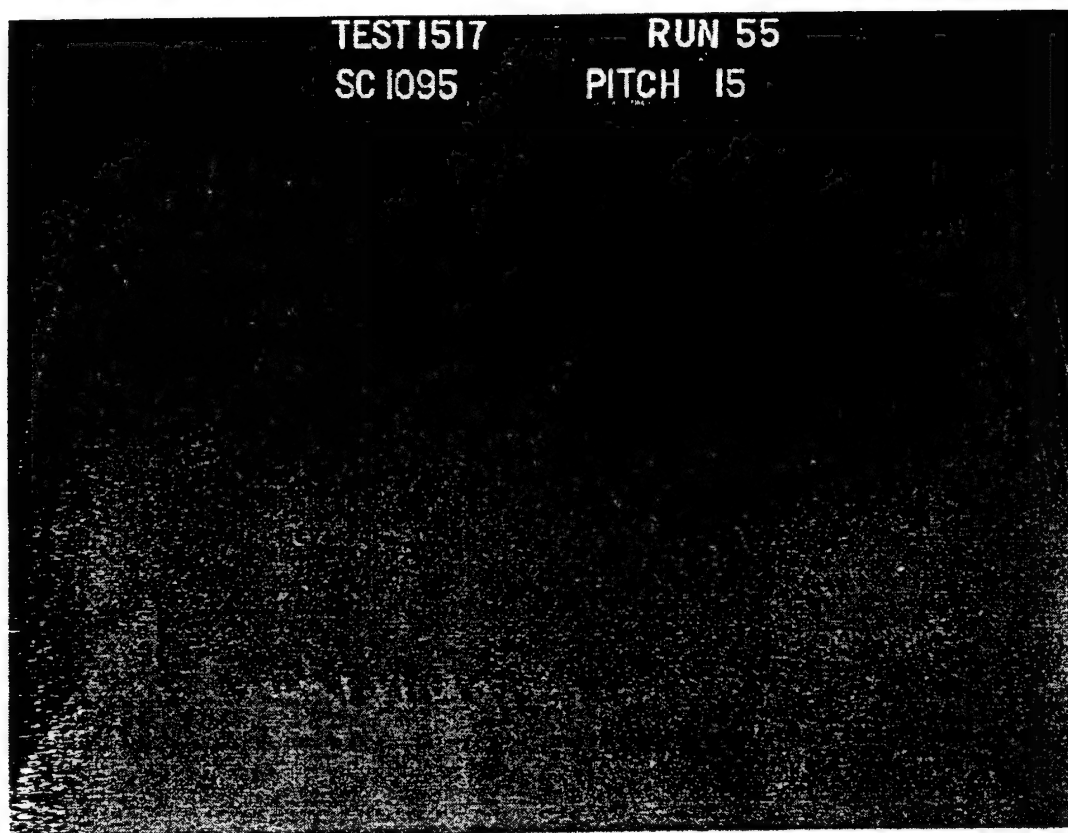
Figure 43: Flow Visualization of Case 1 at 15 degrees Angle of Attack at
$Re = 2 \times 10^6$
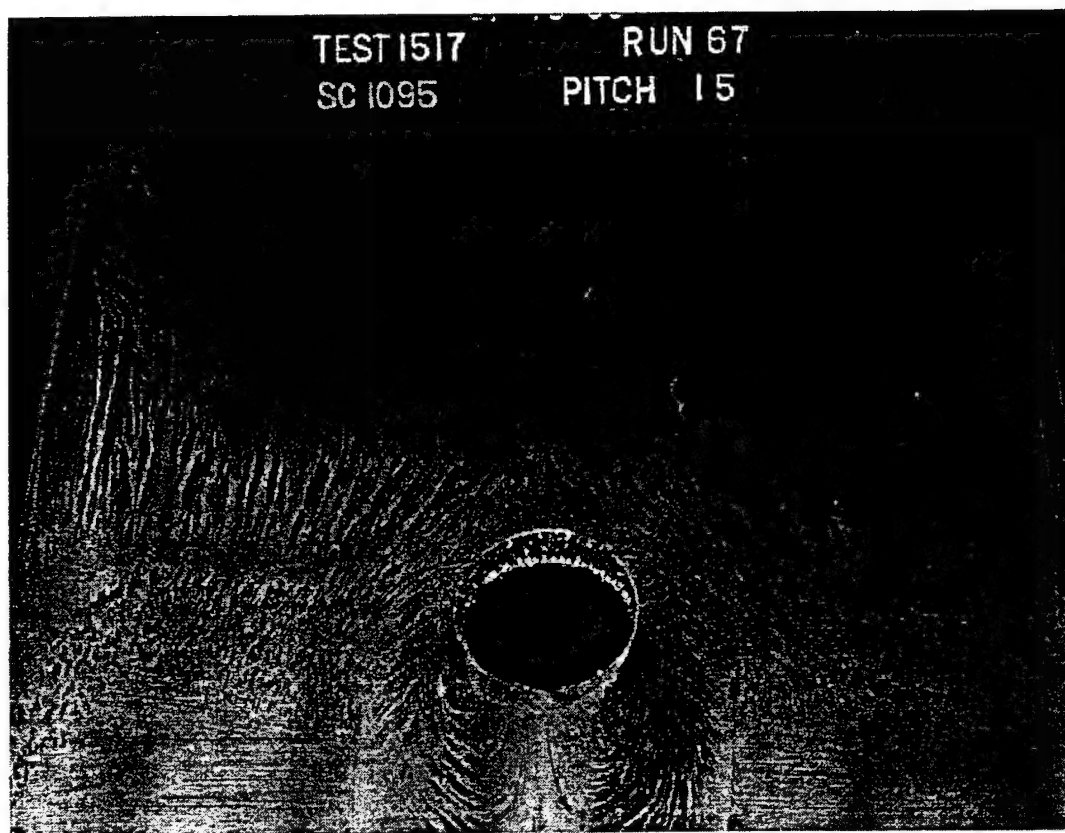
Figure 44: Flow Visualization of Case 1A at 15 degrees Angle of Attack at
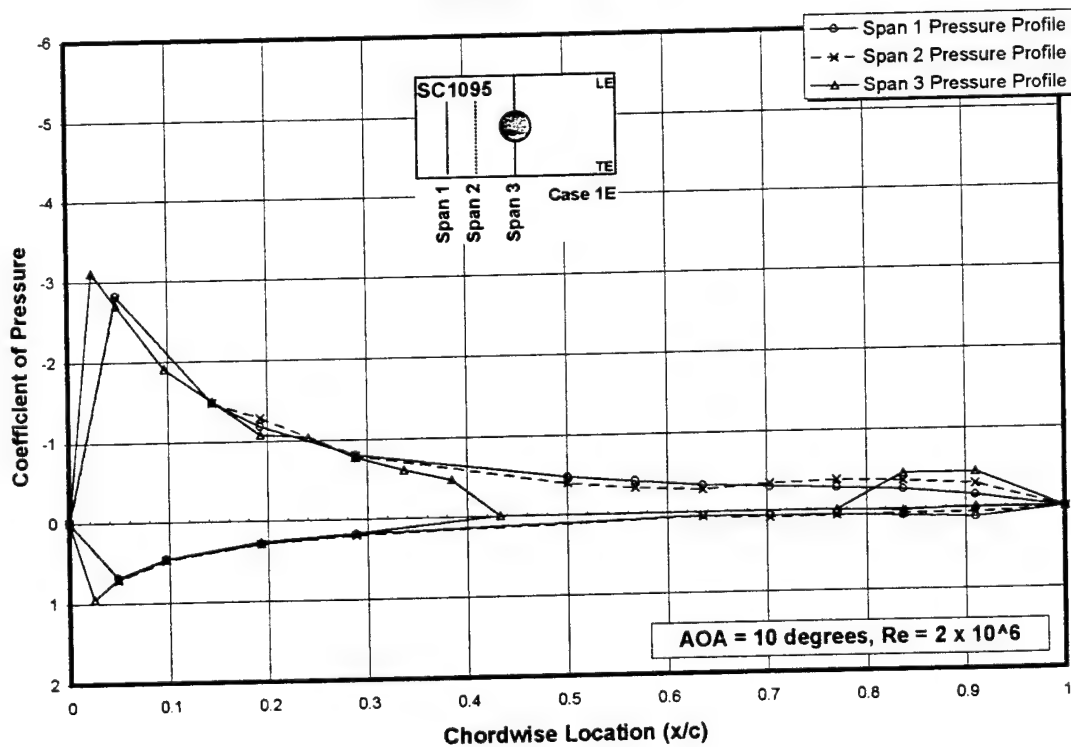$Re = 2 \times 10^6$

138
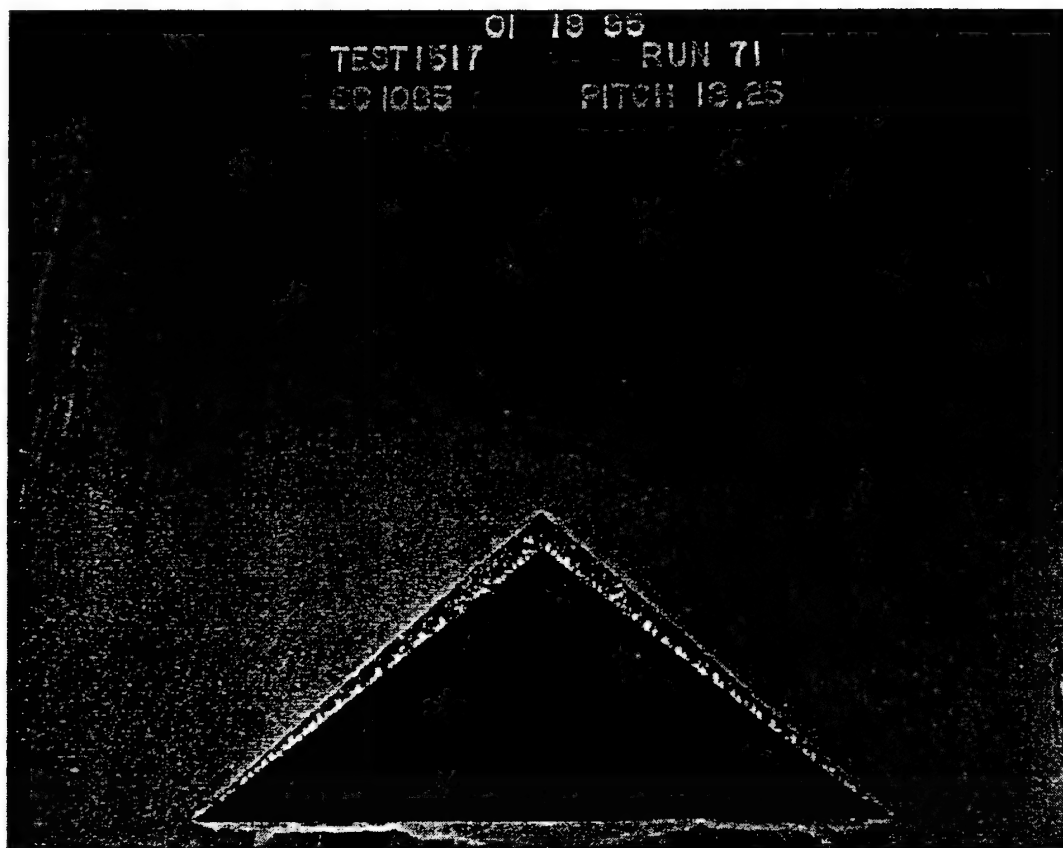
Figure 45: Flow Visualization of Case 1B at 13.25 degrees Angle of Attack at
$Re = 2 \times 10^6$
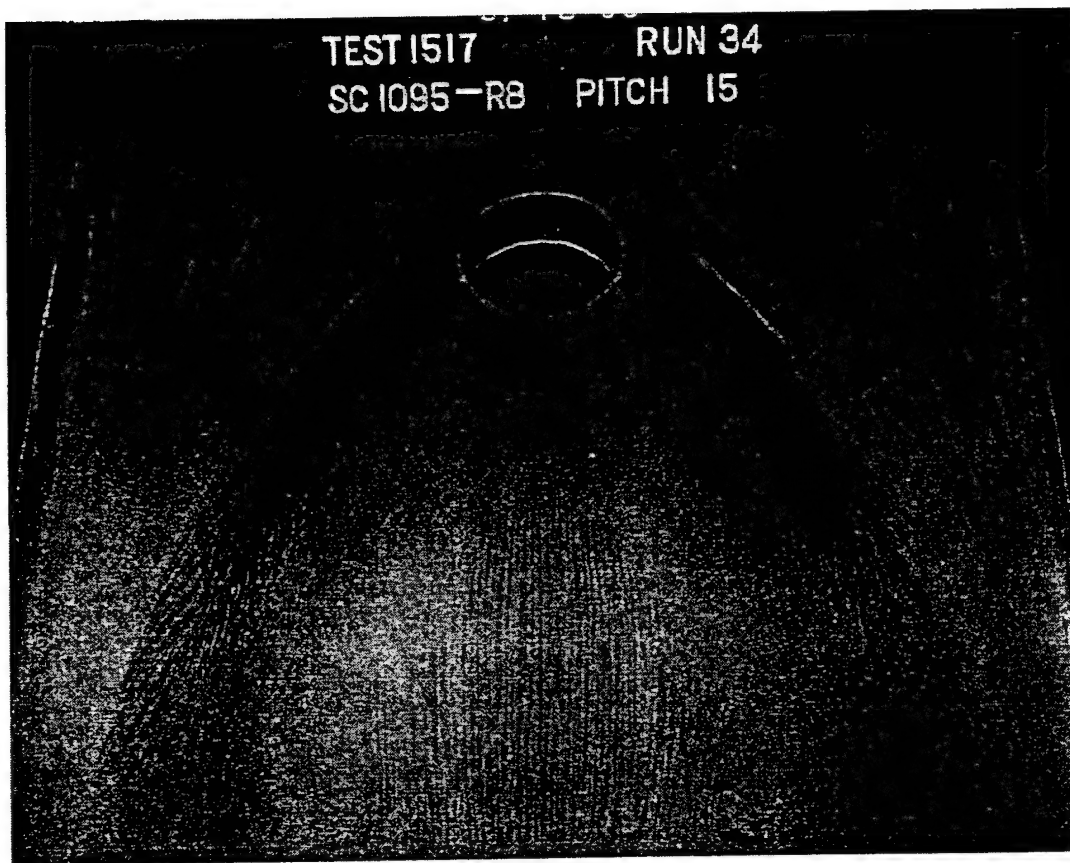
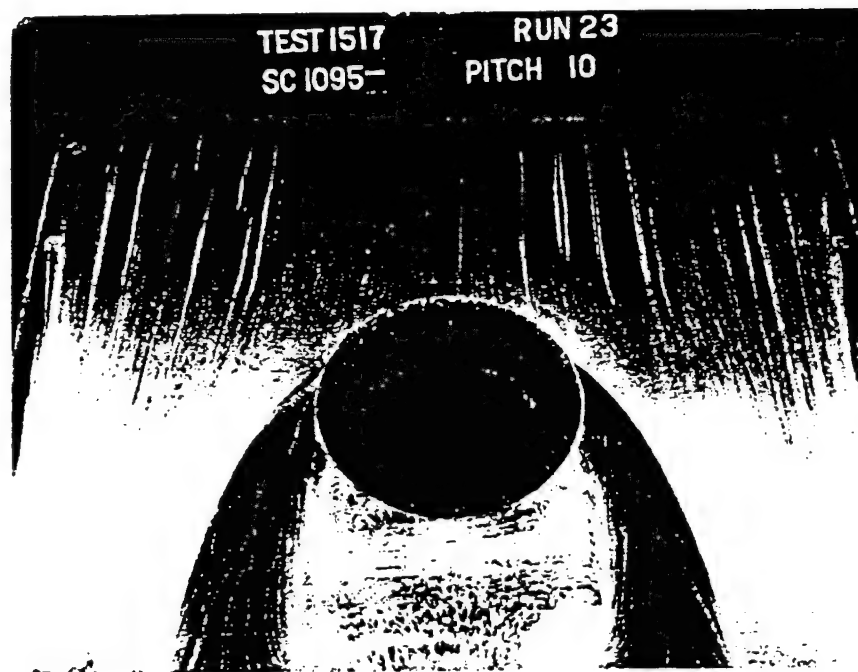Figure 46: Flow Visualization of Case 2A at 15 degrees Angle of Attack at
$Re = 2 \times 10^6$
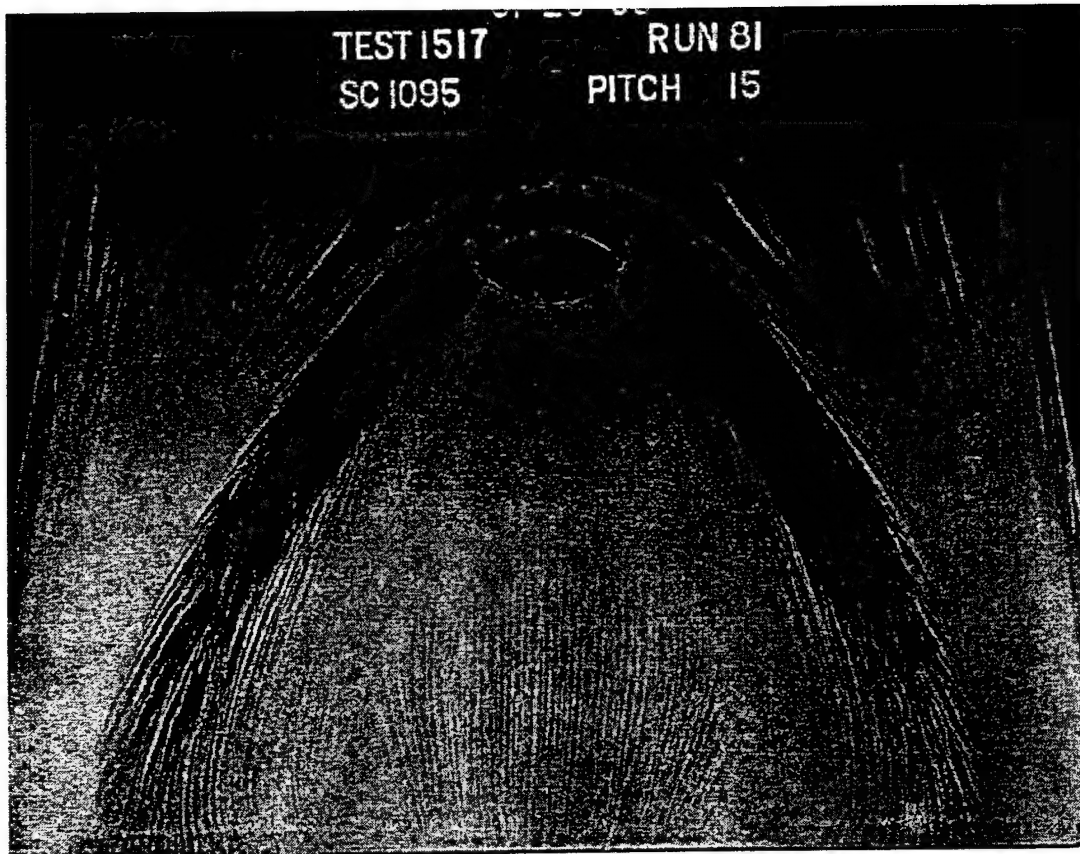
Figure 47: Flow Visualization of Case 2B at 15 degrees Angle of Attack at
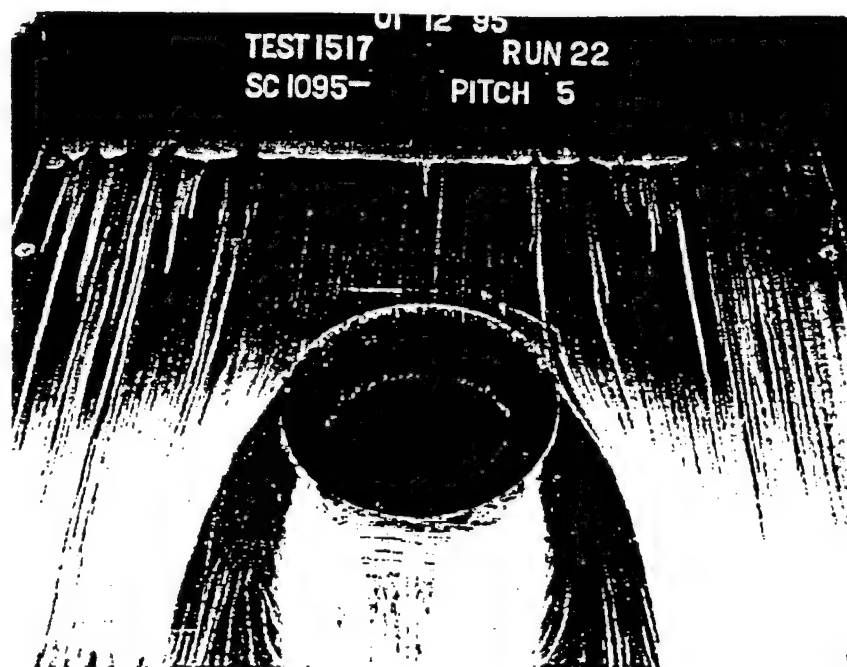$Re = 2 \times 10^6$
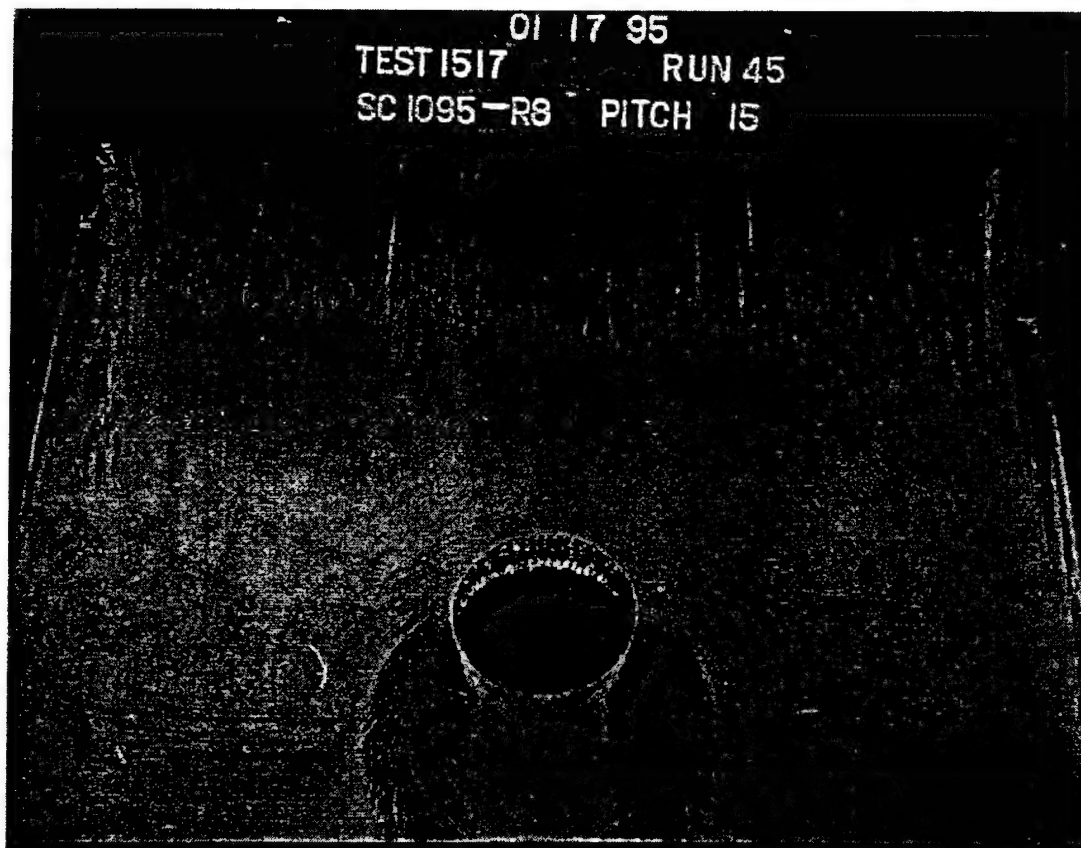
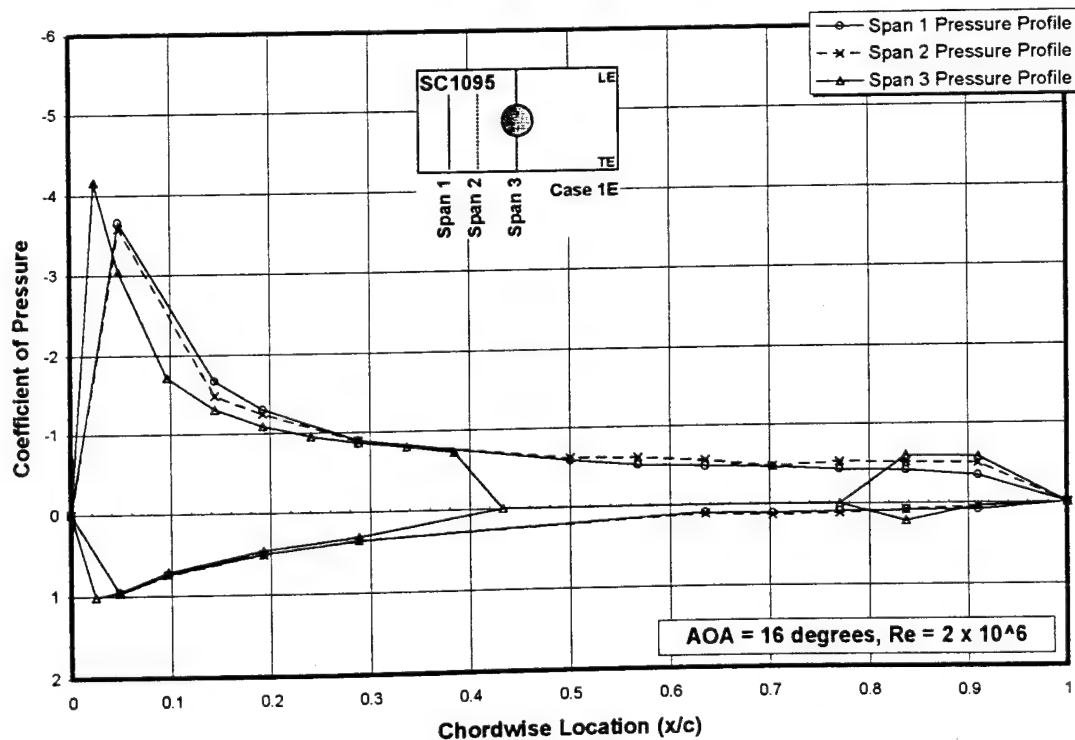Figure 48: Flow Visualization of Case 2C at 15 degrees Angle of Attack at
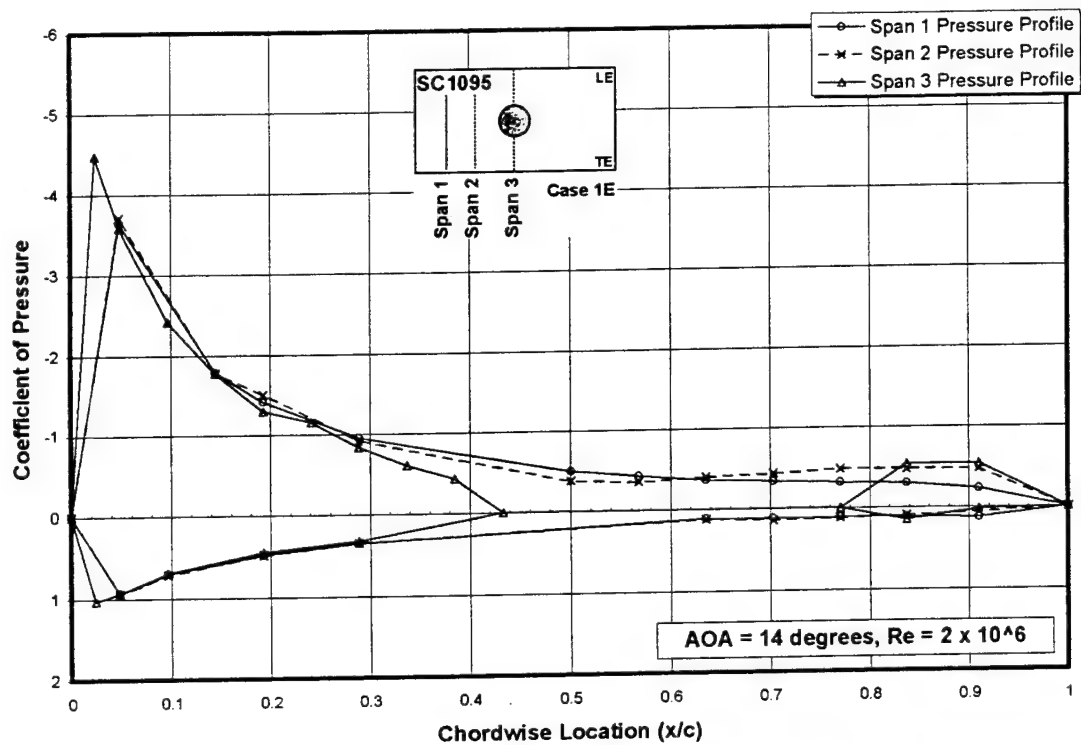$Re = 2 \times 10^6$
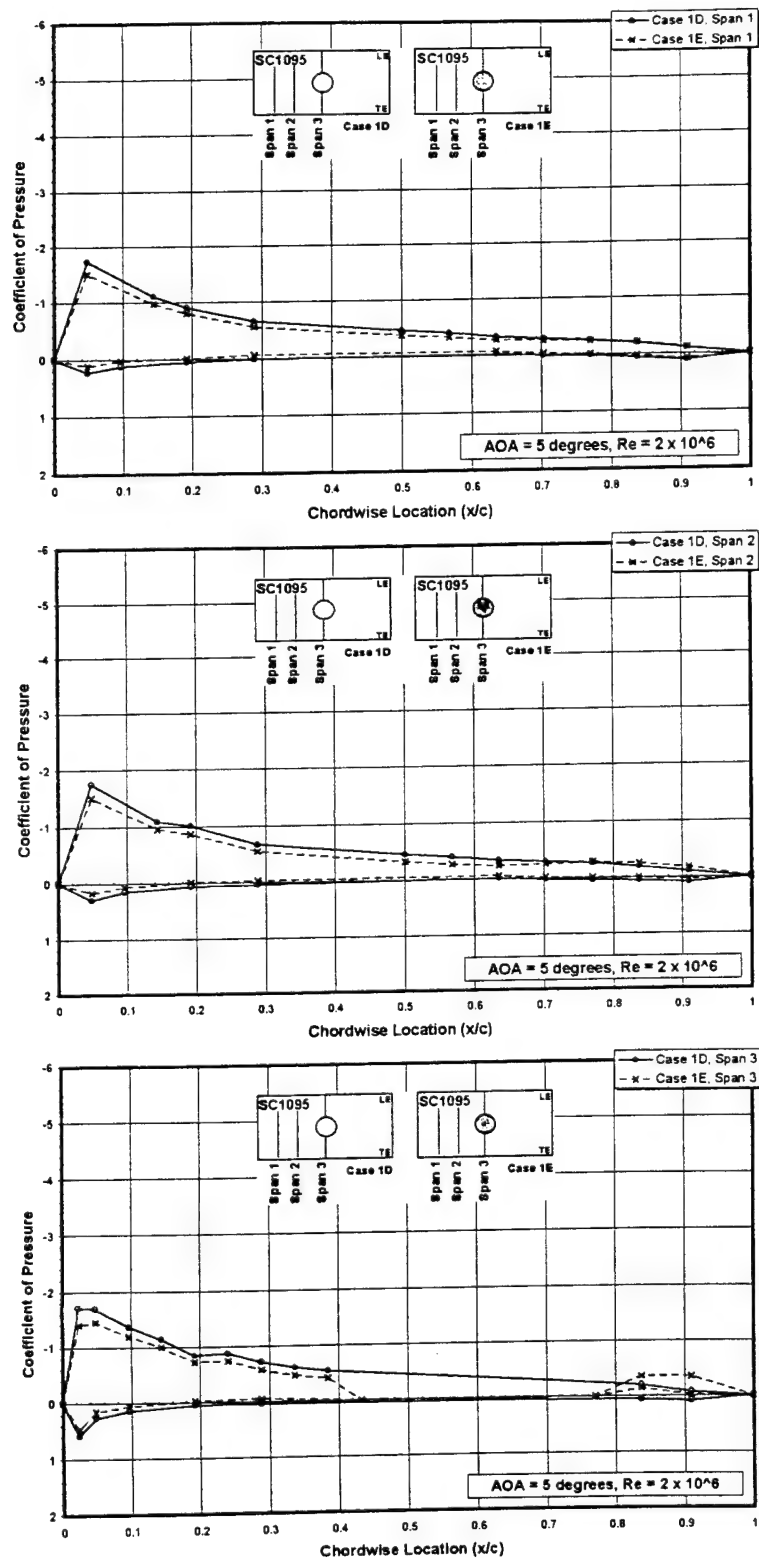
Figure 49: Combined Spanwise Pressure Profiles for Case 1D and Case 1E at 5 degrees Angle of Attack and Re = 2 x 10^6

143
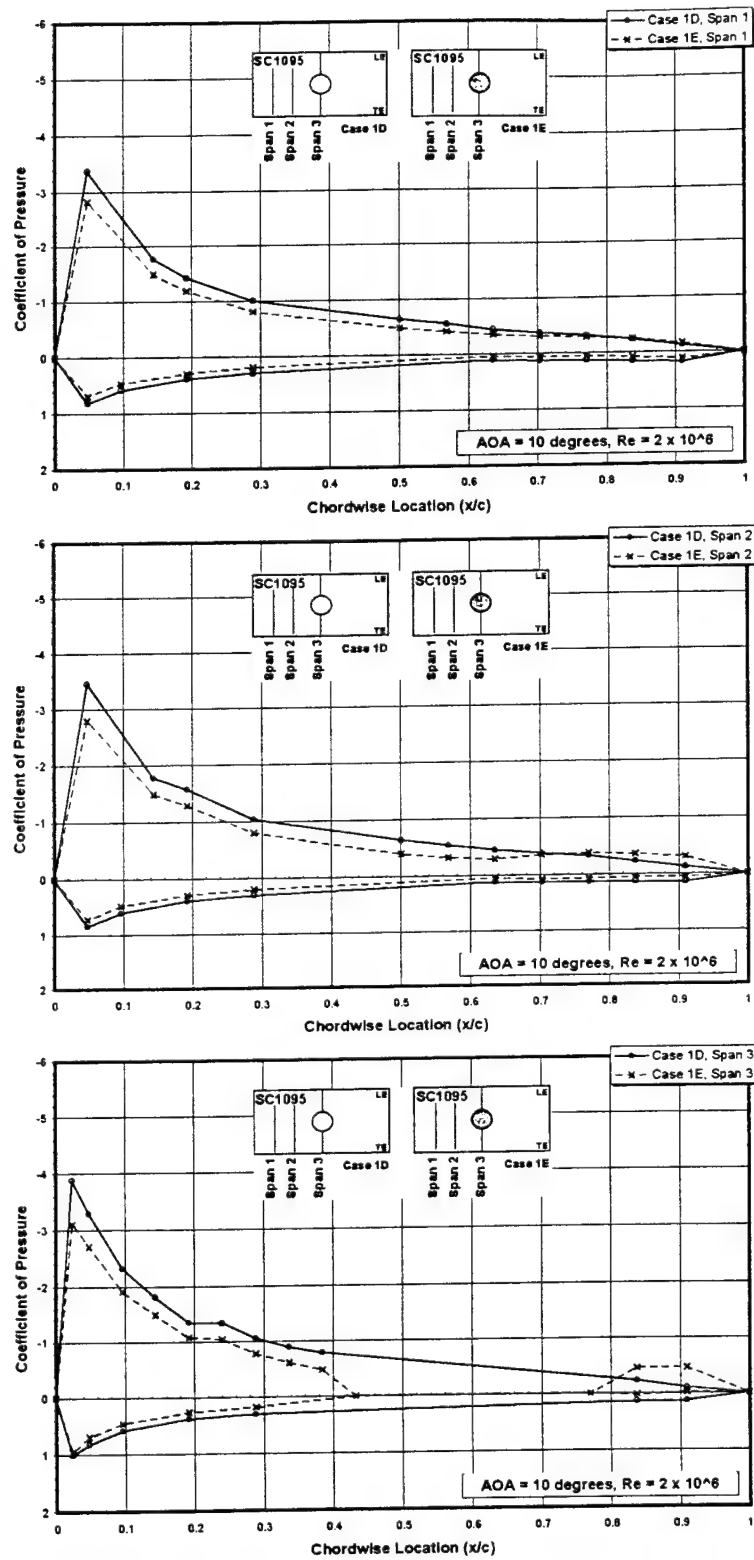
Figure 50: Combined Spanwise Pressure Profiles for Case 1D and Case 1E at 10 degrees Angle of Attack and Re = 2 x 10^6
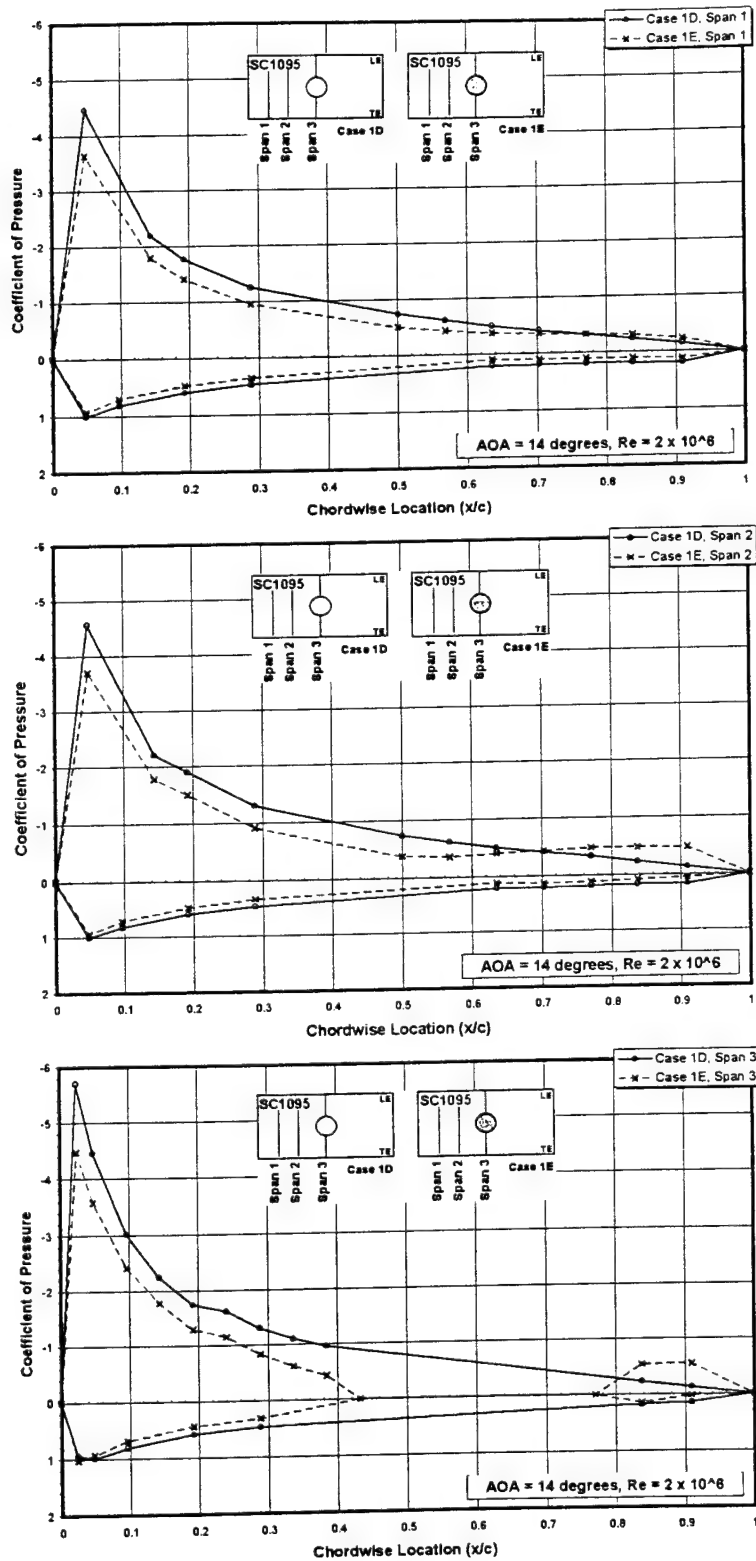
Figure 51: Combined Spanwise Pressure Profiles for Case 1D and Case 1E at 14 degrees Angle of Attack and Re = 2 x 10^6

145
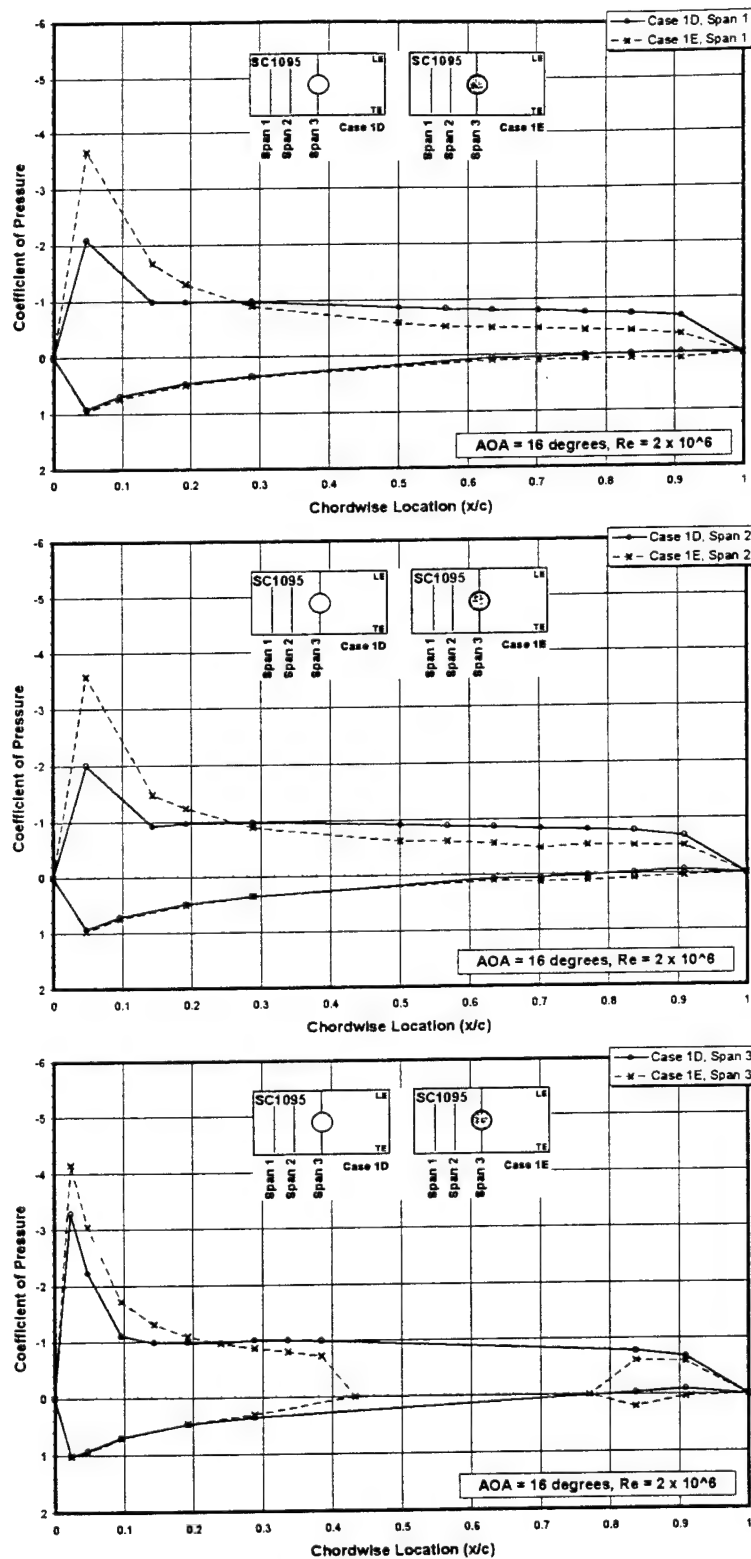
Figure 52: Combined Spanwise Pressure Profiles for Case 1D and Case 1E at 16 degrees Angle of Attack and Re = 2 x 10^6

146
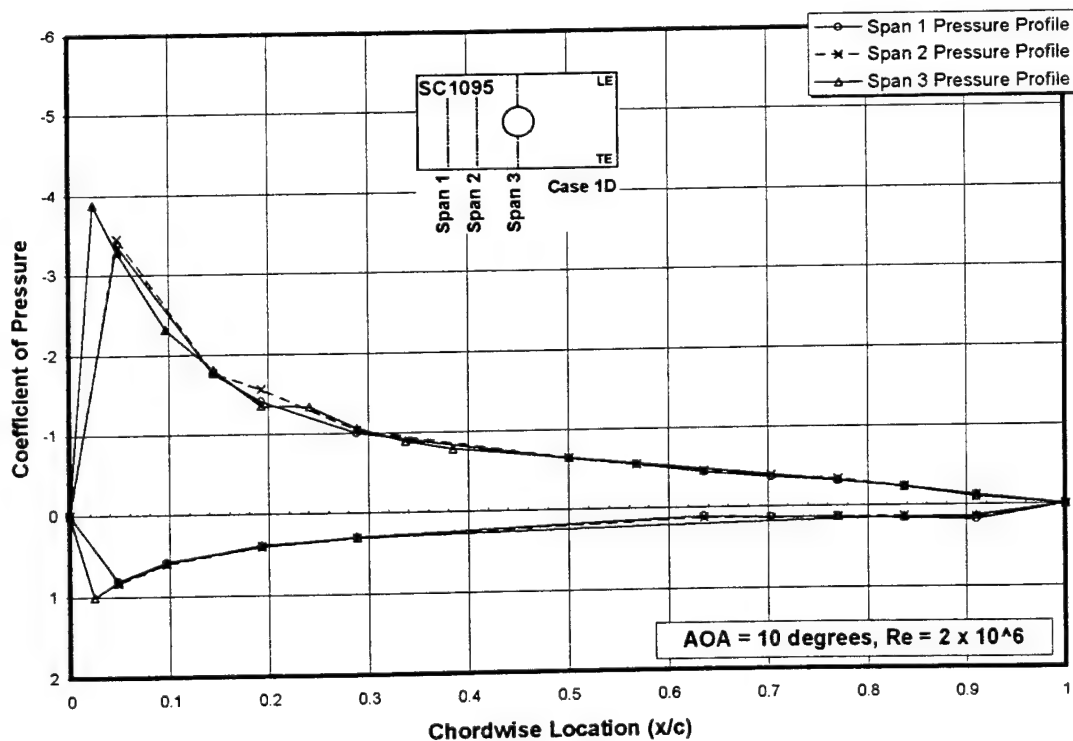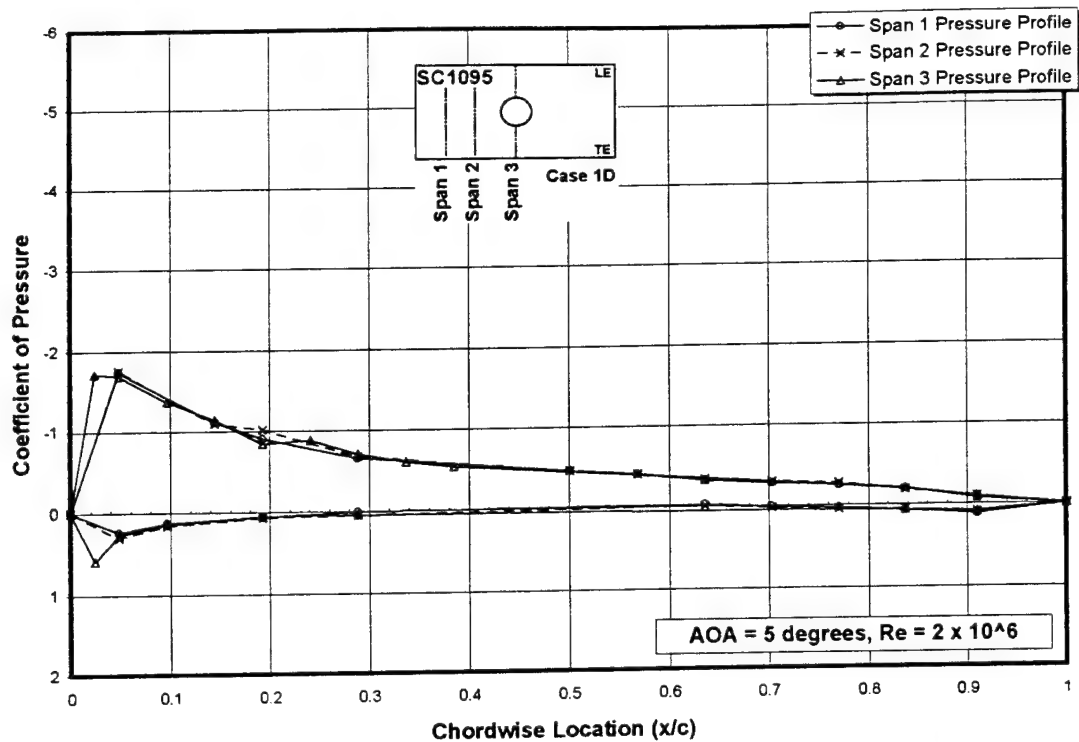
Figure 53: Spanwise Pressure Profiles for Case 1D at 5 and 10 degrees Angle of Attack at Re = 2 x 10^6
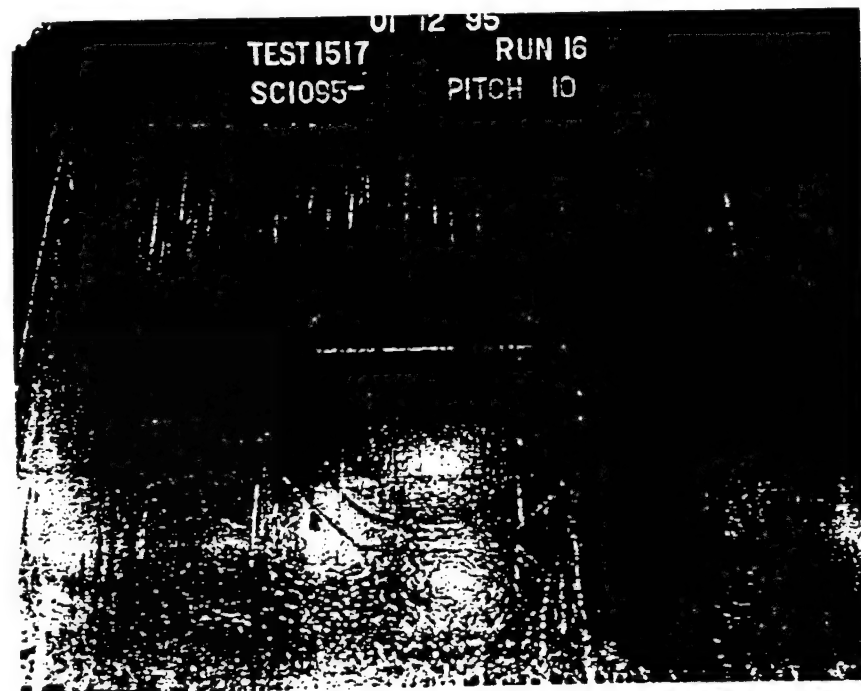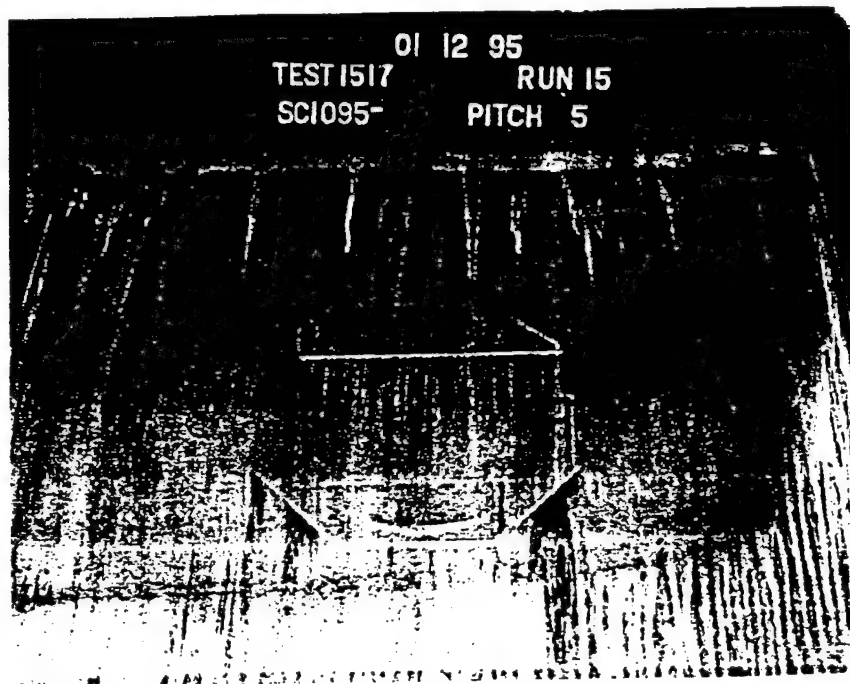
Figure 54: Flow Visualization of Case 1D at 5 and 10 degrees Angle of Attack at
$Re = 2 \times 10^6$
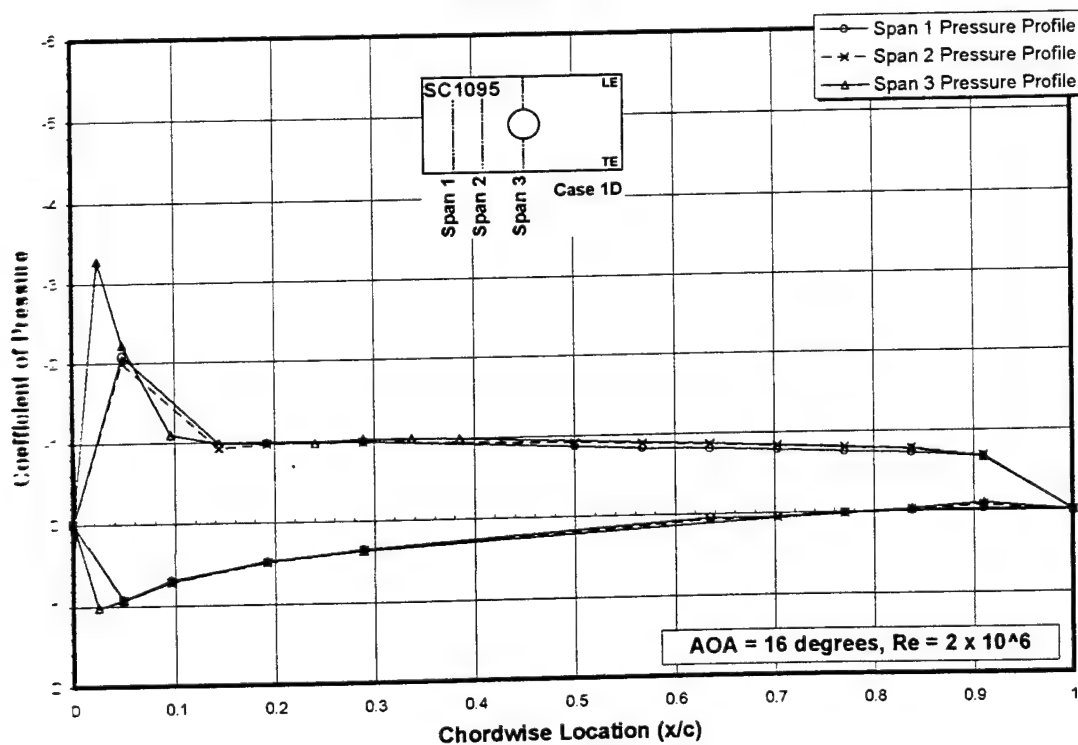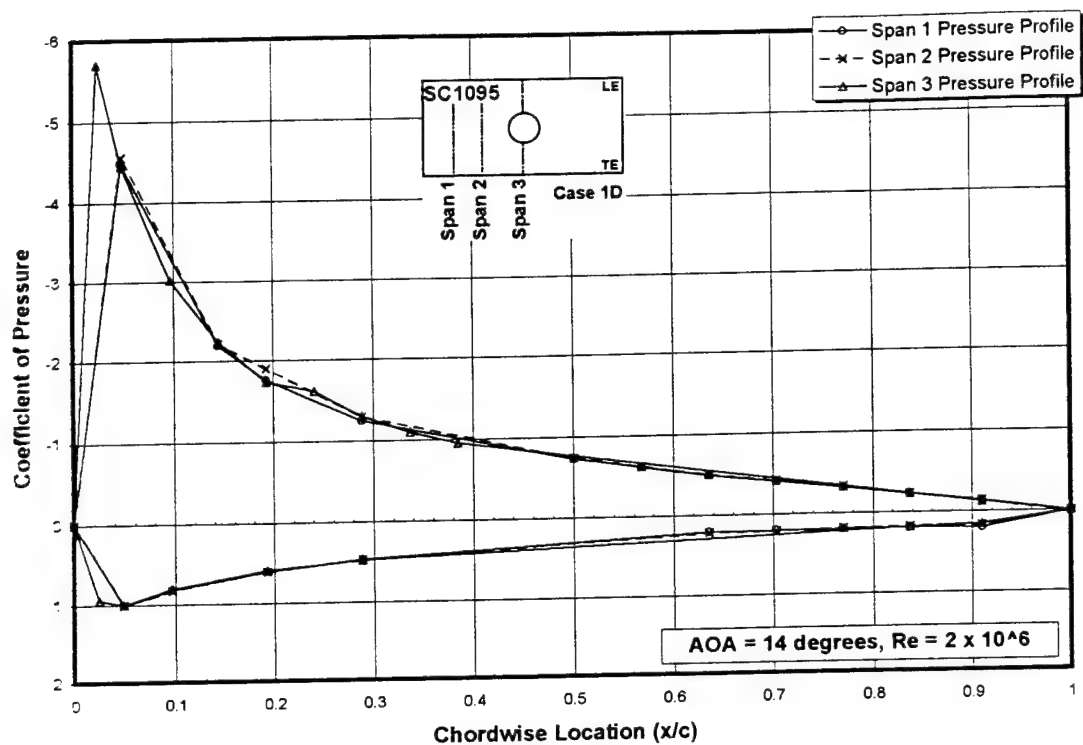
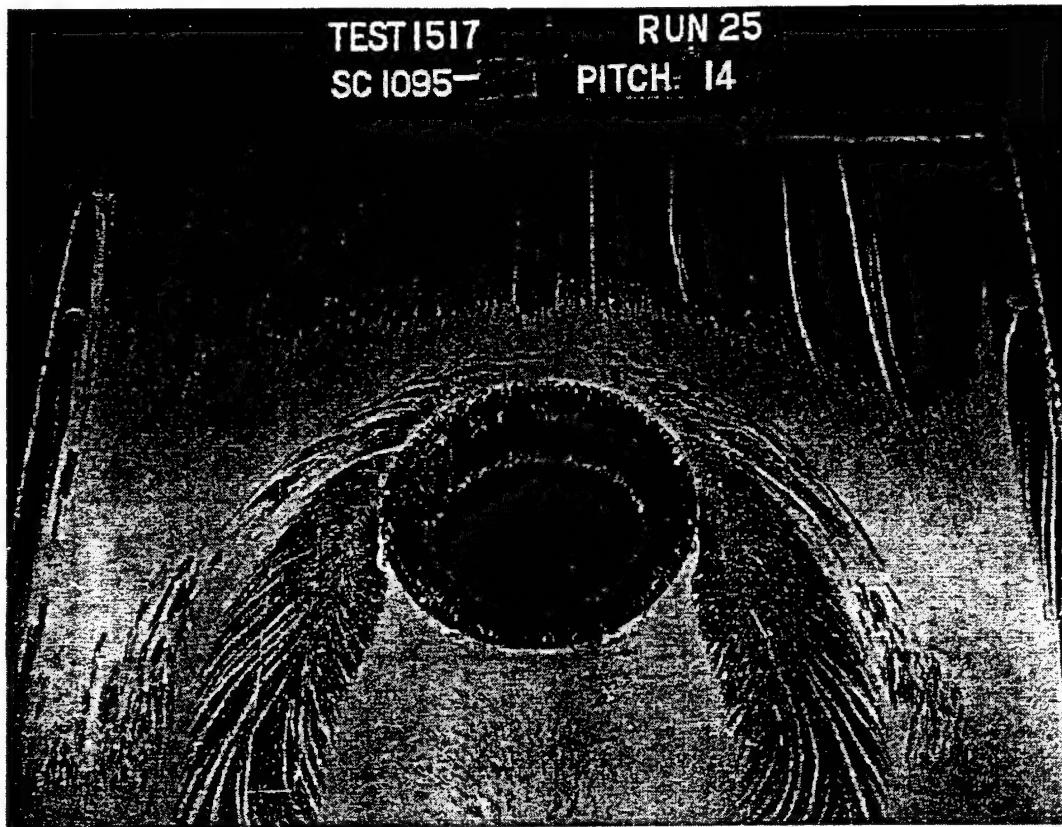Figure 55: Spanwise Pressure Profiles for Case 1D at 14 and 16 degrees Angle of Attack at Re = 2 x 10^6
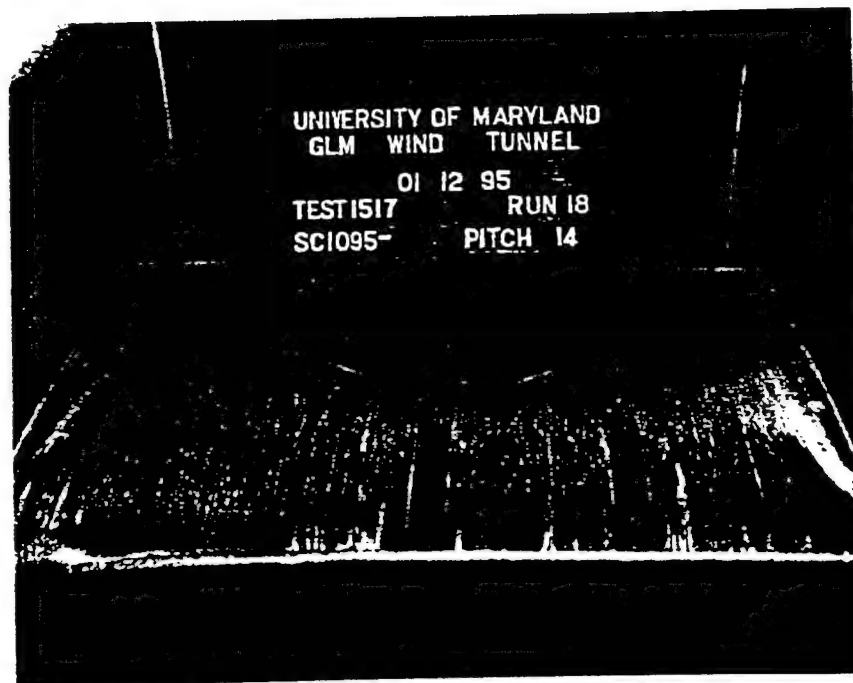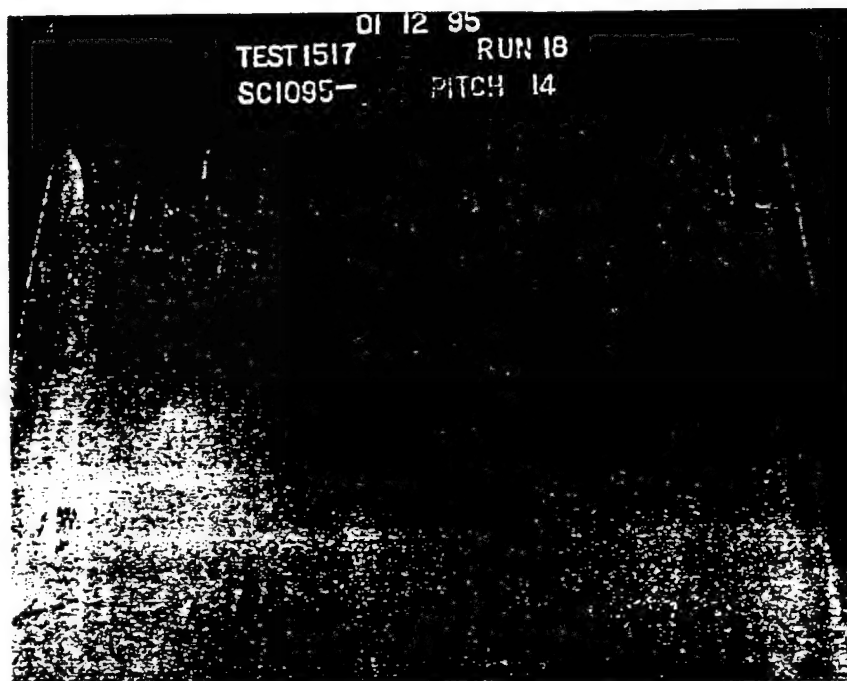
Figure 56: Flow Visualization of Case 1D at 14 degrees Angle of Attack at
$Re = 2 \times 10^6$ (top and front views)
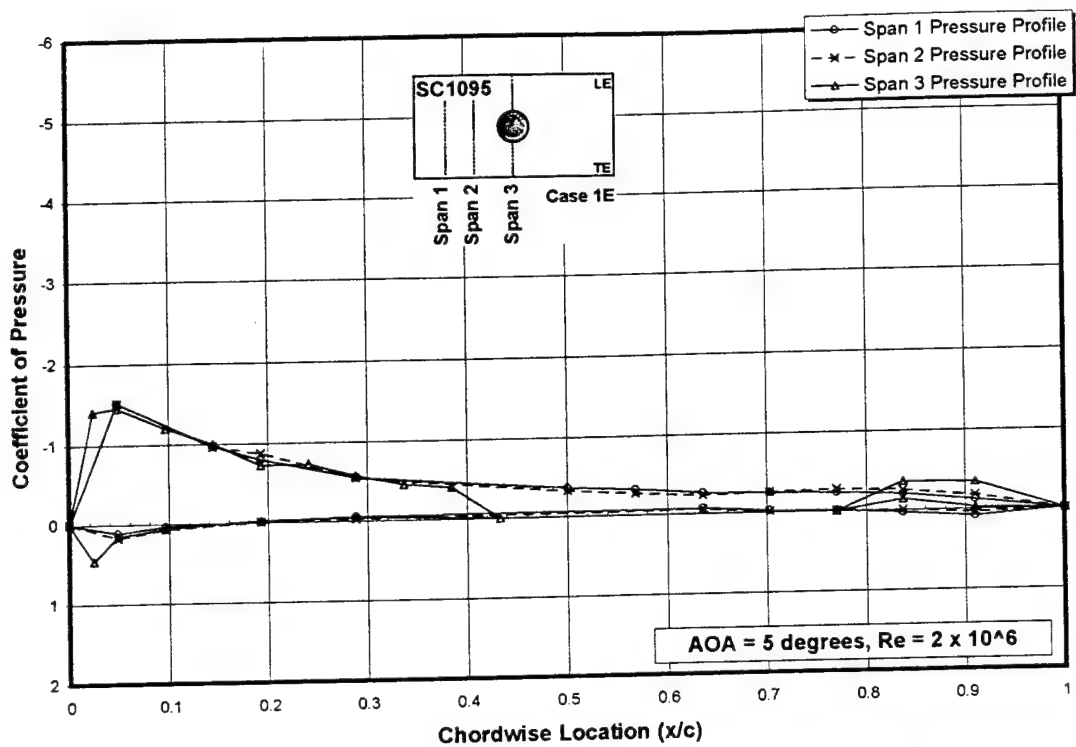
Figure 57: Spanwise Pressure Profiles for Case 1E at 5 and 10 degrees Angle of Attack at Re = 2 x 10^6

Figure 58: Flow Visualization of Case 1E at 5 and 10 degrees Angle of Attack at
$Re = 2 \times 10^6$

Figure 59: Spanwise Pressure Profiles for Case 1E at 14 and 16 degrees Angle of Attack at Re = 2 x 10⁶

Figure 60: Flow Visualization of Case 1E at 14 degrees Angle of Attack at
$Re = 2 \times 10^6$
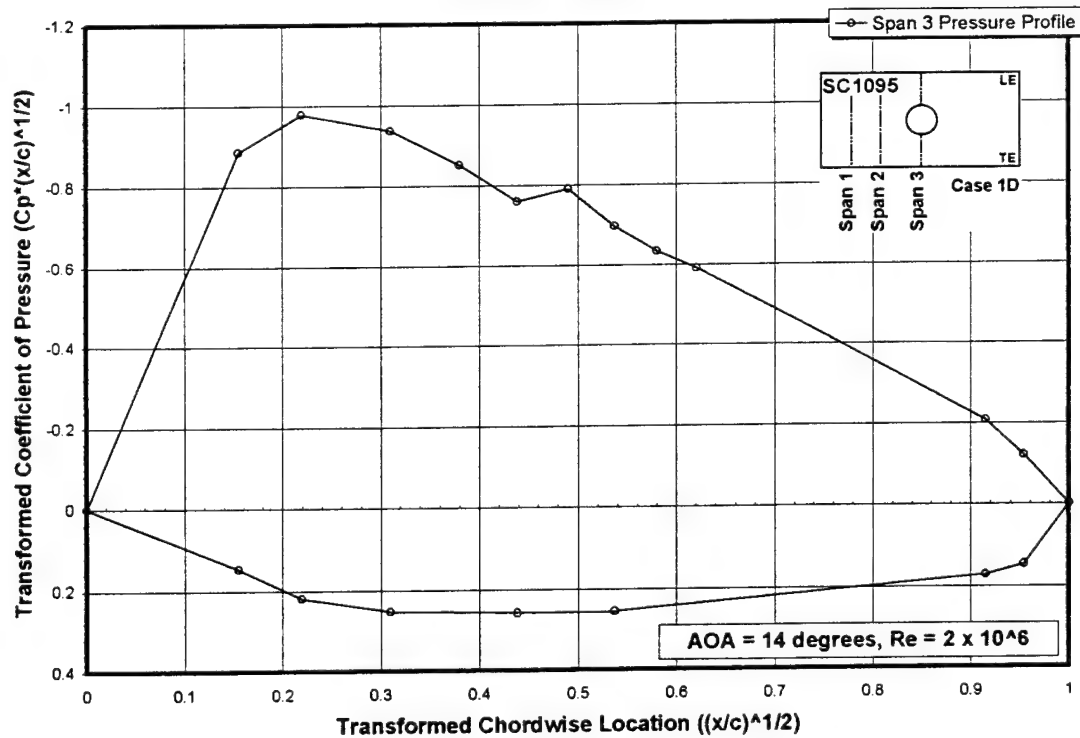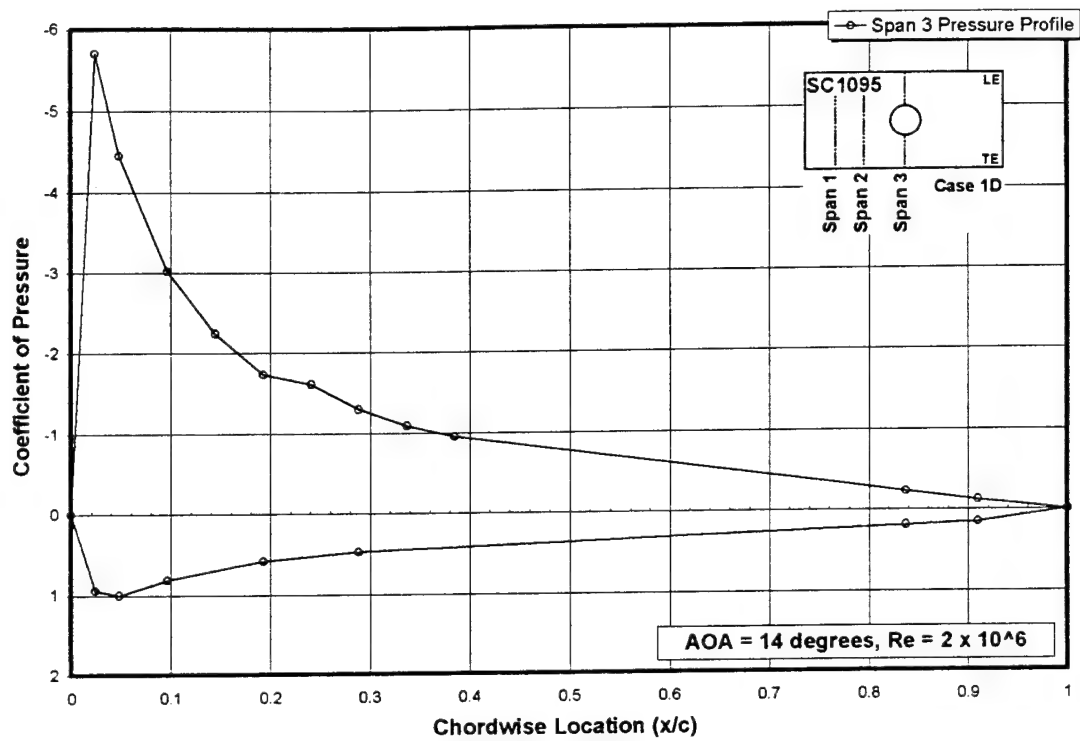
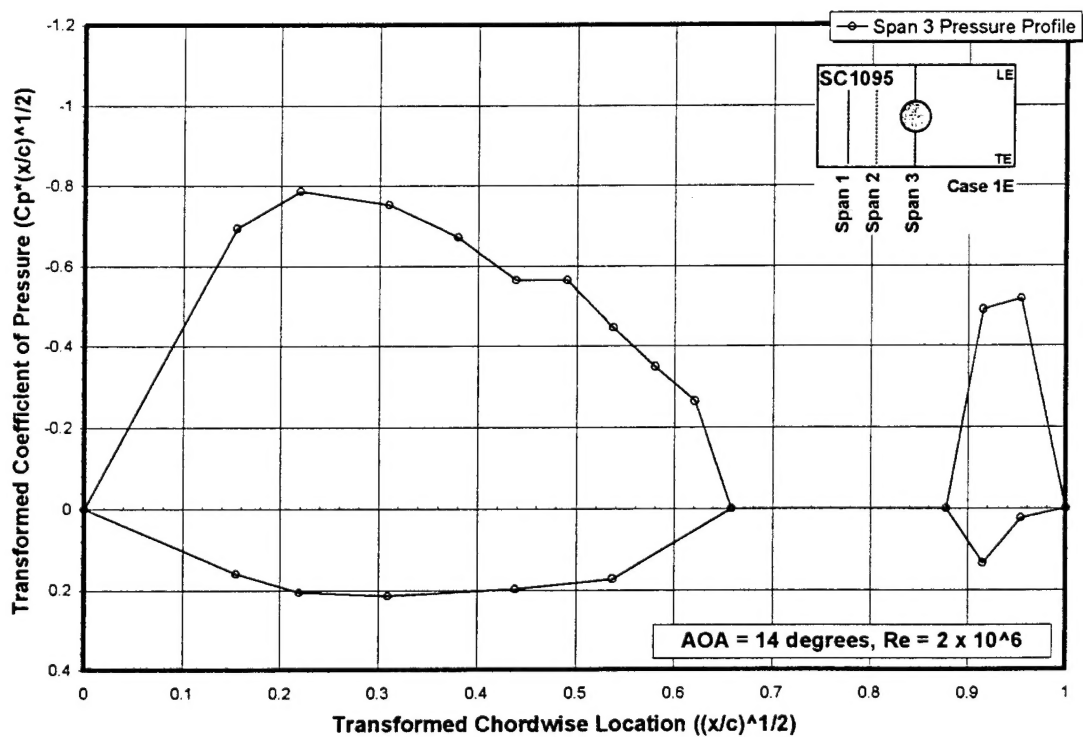Figure 61: Transformation of the Chordwise Pressure Distribution for Case 1D
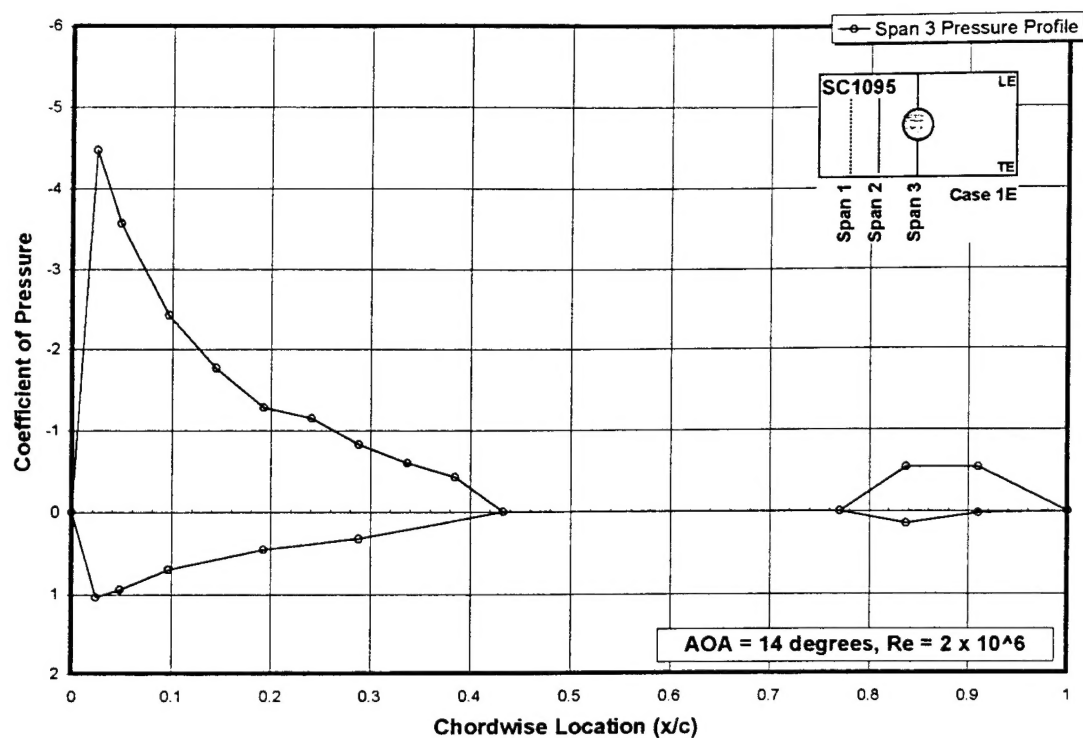
Figure 62: Transformation of the Chordwise Pressure Distribution for Case 1E
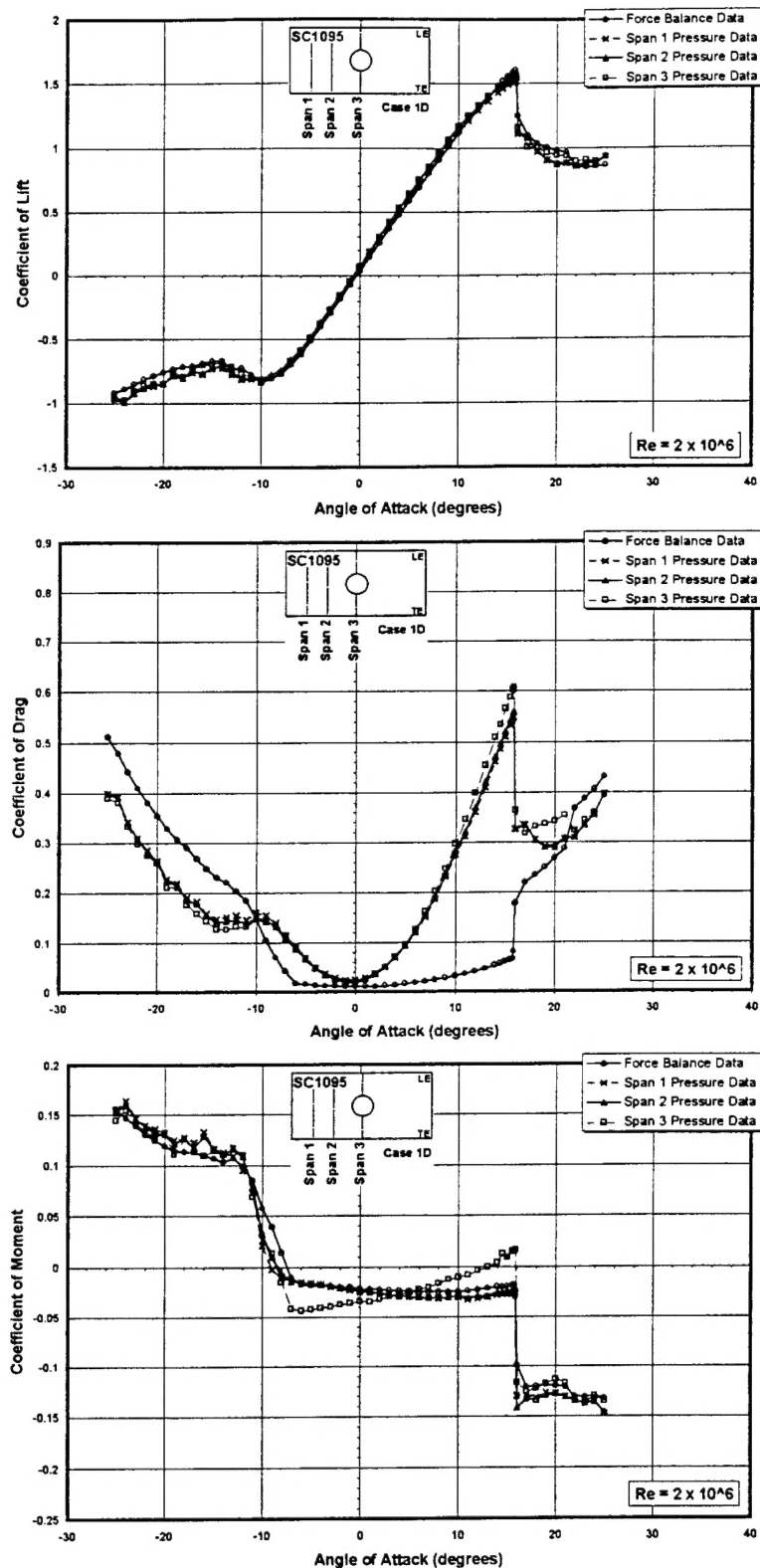
Figure 63: A Comparison of the Aerodynamic Characteristics Derived from Force
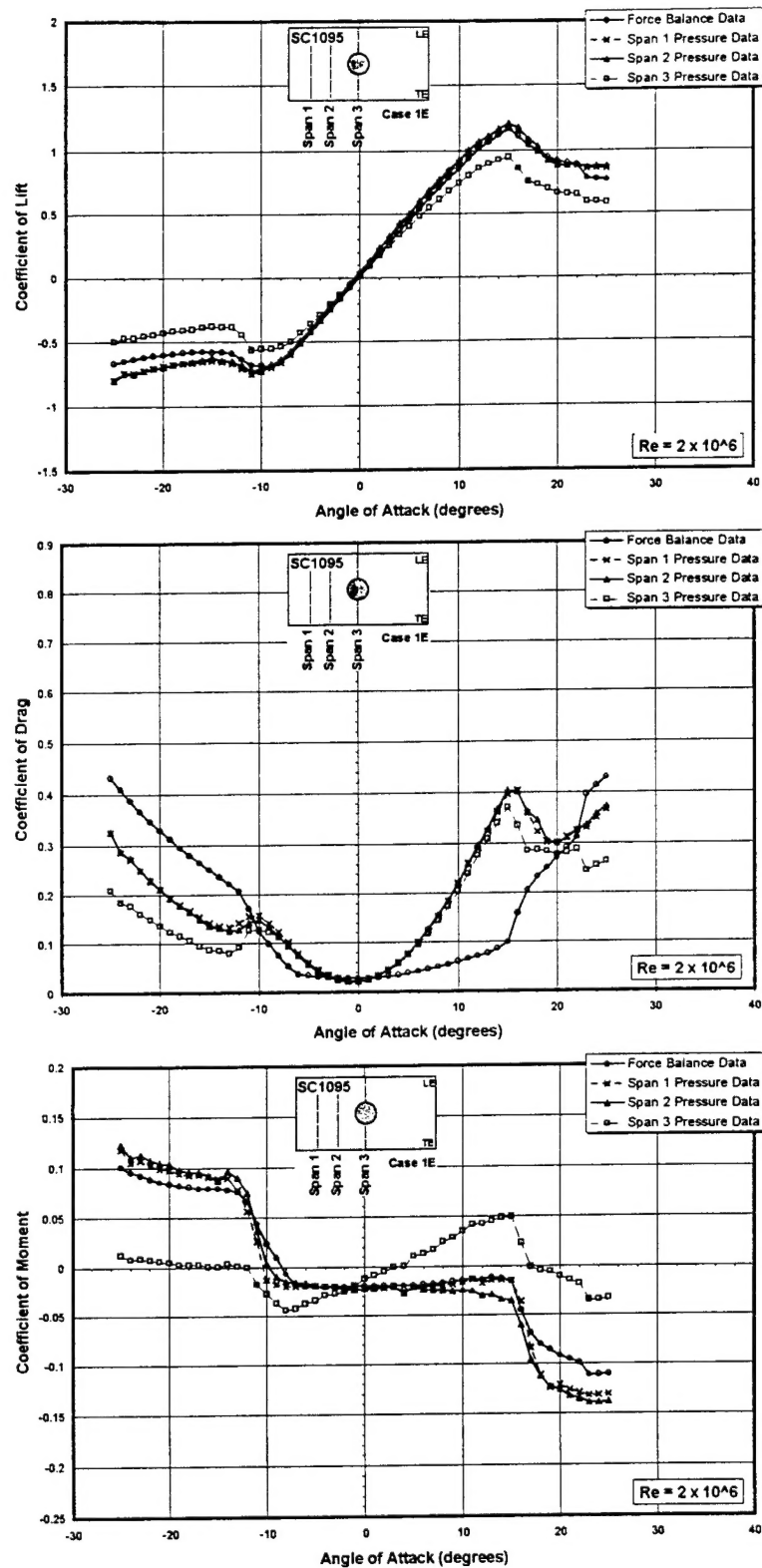Balance and Integrated Pressure Data for Case 1D at Re = 2 x 10^6

Figure 64: A Comparison of the Aerodynamic Characteristics Derived from Force Balance and Integrated Pressure Data for Case 1E at Re = 2 x 10^6
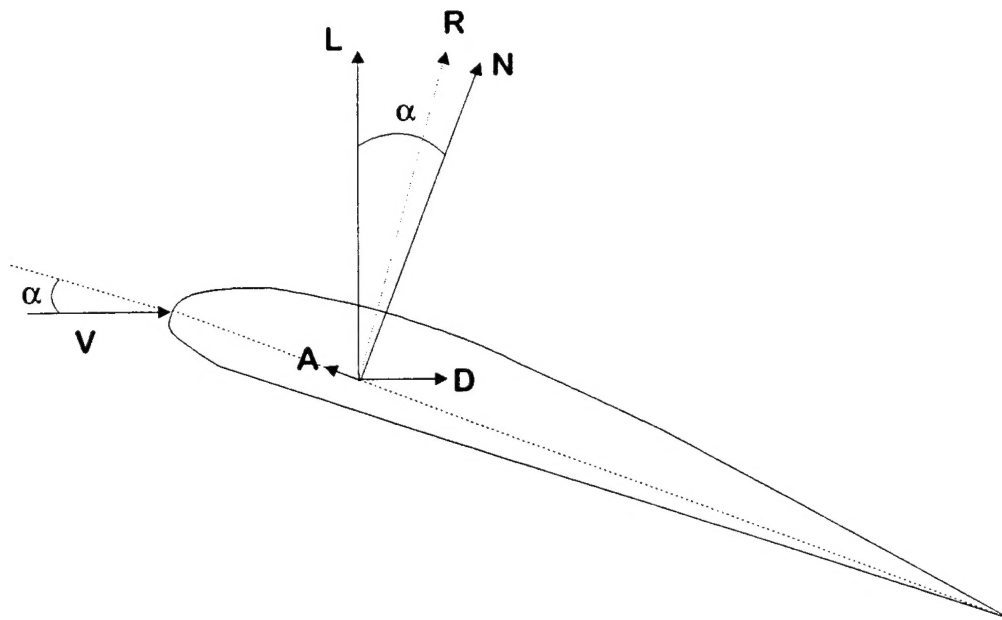
158

Figure 65: Definition of Aerodynamic Force Components